Polymer Nanoparticles

Their Functionalization for Biomedical Applications and Dynamics near an Electrode

Dissertation
zur Erlangung des Grades
"Doktor der Naturwissenschaften"
im Promotionsfach Chemie

am Fachbereich Chemie, Pharmazie und Geowissenschaften
der Johannes Gutenberg-Universität
in Mainz

Veronika Beer
geb. in Augsburg

Mainz, 2015

Dekan: *aus Datenschutzgründen online nicht verfügbar*
Erster Berichterstatter: *aus Datenschutzgründen online nicht verfügbar*
Zweiter Berichterstatter: *aus Datenschutzgründen online nicht verfügbar*
Tag der Promotion: 1.9.2015

Zusammenfassung

In der vorliegenden Arbeit wird eine Methode vorgestellt, mit der biokompatible Nanopartikel aus Polymilchsäure (poly(L-lactic acid), PLLA) mit Ladungs- oder Fluoreszenzfunktionalisierung versehen werden können. Hierfür wurde eine Miniemulsions-Lösungsmittelverdampfungstechnik angewandt, bei der neben vorpolymerisiertem PLLA auch ein zuvor synthetisiertes Copolymer aus Methacrylsäure bzw. einem polymerisierbaren Farbstoff und einem Oligomilchsäure-Makromonomer eingesetzt wurde. Alternativ wurden die Copolymerisation gleichzeitig mit der Miniemulsion und Lösungsmittelverdampfung durchgeführt.

Die erhöhte Stabilität in Salzlösungen der carboxylfunktionaliserten Nanopartikel im Vergleich zu reinen PLLA-Nanopartikeln wurde in einer Lichtstreustudie gezeigt. Hierbei waren die Eigenschaften der Partikel, die aus dem separat synthetisierten Copolymer hergestellt wurden und jenen, die aus der simultanen Durchführung des Polymerisations- und Miniemulsions-Verdampfungsschritts hervorgingen, nahezu identisch.

Das Hauptaugenmerk bei der Charakterisierung der fluoreszenzmarkierten Nanopartikel lag auf einer stabilen Bindung des Fluoreszensfarbstoffs, sodass dieser auch bei Lagerung oder in längeren Experimenten nicht freigesetzt wird. Im Fluoreszenzkorrelationsspektroskopie-Experiment wurde gezeigt, dass auch nach zwei Wochen keine Freisetzung des Farbstoffs in das Lösungsmittel erfolgte.

Neben der biomedizinischen Forschung, für die die oben beschriebenen Nanopartikel optimiert wurden, spielen diese auch in der Beschichtungstechnologie eine Rolle. Eine Möglichkeit zur Herstellung von Beschichtungen ist die elektrophoretische Abscheidung (EPD, electrophoretic deposition) von Partikeln. Hierbei ist die Beweglichkeit von Nanopartikeln an Elektrodenoberflächen relevant.

In der vorliegenden Arbeit wurde dieses mittels resonanzverstärkter dynamischer Lichtstreuung (REDLS, resonance enhanced dynamic light scattering) untersucht. Hierfür wurde ein Versuchsaufbau entwickelt, bei dem das evaneszente elektromagnetische Feld eines Oberflächenplasmons das entlang einer Gold-Proben-Grenzfläche propagiert, als einfallender Strahl für die dynamische Lichtstreuung genutzt wird. Die Goldschicht dient gleichzeitig als Elektrode. Aufgrund der limitierten Eindringtiefe des evaneszenten Feldes in die Probenschicht von ca. 200 nm konnten Erkenntnisse über die spannungs- und frequenzabhängige Beweglichkeit der Nanopartikel dicht an der Elektrode erhalten werden. Zudem ermöglicht der Aufbau die gleichzeitige Messung bei vier verschiedenen Streuwinkeln was die Untersuchung von Proben, die zeitlichen Veränderungen unterliegen, erlaubt. Die Ergebnisse wurden in Zusammenhang mit den vorgeschlagenen Mechanismen zur EPD diskutiert.

Abstract

In this work, a method for the functionalization of biocompatible, poly(lactic acid)-based nanoparticles with charged moieties or fluorescent labels is presented. Therefore, a miniemulsion solvent evaporation procedure is used in which prepolymerized poly(L-lactic acid) is used together with a previously synthesized copolymer of methacrylic acid or a polymerizable dye, respectively, and an oligo(lactic acid) macromonomer. Alternatively, the copolymerization has been carried out in one step with the miniemulsion solvent evaporation. The increased stability in salty solutions of the carboxyl-modified nanoparticles compared to nanoparticles consisting of poly(lactic acid) only has been shown in light scattering experiments. The properties of the nanoparticles that were prepared with the separately synthesized copolymer were almost identical to those in which the copolymerization and particle fabrication were carried out simultaneously.

During the characterization of the fluorescently labeled nanoparticles, the focus was on the stable bonding between the fluorescent dye and the rest of the polymer chain to ensure that none of it is released from the particles, even after longer storage time or during lengthy experiments. In a fluorescence correlation spectroscopy experiment, it could be shown that even after two weeks, no dye has been released into the solvent.

Besides biomedical research for which the above described, functionalized nanoparticles were optimized, nanoparticles also play a role in coating technology. One possibility to fabricate coatings is the electrophoretic deposition of particles. In this process, the mobility of nanoparticles near electrode interfaces plays a crucial role.

In this thesis, the nanoparticle mobility has been investigated with resonance enhanced dynamic light scattering (REDLS). A new setup has been developed in which the evanescent electromagnetic field of a surface plasmon that propagates along the gold-sample interface has been used as incident beam for the dynamic light scattering experiment. The gold layer that is necessary for the excitation of the plasmon doubles as an electrode. Due to the penetration depth of the surface plasmon into the sample layer that is limited to ca. 200 nm, insights on the voltage- and frequency dependent mobility of the nanoparticles near the electrode could be gained. Additionally, simultaneous measurements at four different scattering angles can be carried out with this setup, therefore the investigation of samples undergoing changes is feasible. The results were discussed in context with the mechanisms of electrophoretic deposition.

Contents

1. Introduction

Biocompatibility is a key characteristic of poly(lactic acid)-based (PLA-based) nanoparticles. They are studied by chemists and biologists because of their possible biomedical applications. One of them, for example, is the encapsulation oof of superparamagnetic nanoparticles which in turn are used as contrast agents in magnetic resonance imaging or for the generation of heat in hyperthermia. [1] PLA nanoparticles are also potential carriers in targeted delivery due to the possibility of encapsulating drugs into the polymer matrix. [2–4] In this context, the behavior of nanoparticles near interfaces is of high interest. The movement or dynamics of charged nanoparticles in dispersion near solid interfaces under the application of external electric or magnetic fields is of particular importance for future applications, e.g drug delivery.

The miniemulsion solvent evaporation technique is a popular method for the preparation of such nanoparticles because it also enables the convenient encapsulation of further reagents. [5–7] This method requires the use of surfactants, sodium dodecylsulfonate (SDS) being a prominent example. The drawback of SDS and other ionic surfactants with similar good emulsification properties is their cytotoxicity and therefore inferior biocompatibility. [8] Thus, the surfactant must be removed prior to research studies involving living specimen. The extent of this purification is limited by the stabilization effect of the surfactants: Agglomeration of the nanoparticles will be more likely the more of the surfactant is removed. This problem can be solved by using a biocompatible surfactant [9] or by modification of the nanoparticles themselves in order to achieve a higher stability. One option for modification is to aim for a higher surface charge which stabilizes the nanoparticles even when only low amounts of surfactant are present in the dispersion. An increased surface charge of nanoparticles also has been shown to have a positive effect on their uptake by cells. [10–13] In this work, I will demonstrate a preparation strategy for PLA-based nanoparticles which are stabilized by additional carboxyl groups that are negatively charged in aqueous environments

and introduced to the nanoparticles by using a copolymer of an oligo(lactic acid) (OLA) derivate and methacrylic acid in a miniemulsion solvent evaporation procedure. The improved stability of those nanoparticles is verified by investigating their agglomeration behavior in salt solutions of different concentrations.

Another characteristic of nanoparticles used in biomedical research is their fluorescent labeling. Fluorescence imaging techniques are popular to examine the cellular uptake of nanoparticles or their distribution in tissue. The most convenient way to prepare fluorescently labeled nanoparticles is the encapsulation of a hydrophobic dye in the particles. The drawback of this method is that the dye molecules are only physically bound and therefore might be released during imaging experiments for which observation times of several days are common. This might result in a misinterpretation of data as the naked dye molecules might interact differently with the cells than the nanoparticles. A covalent binding of the dye is therefore preferred. The radical addition of a polymerizable dye from the boron-dipyrromethene (BODIPY) family to an OLA with a vinyl group will be presented in this thesis as an alternative to the esterification of a BODIPY dye. [14] The alkyl bond resulting from the radical addition of the dye has superior stability to the ester bond, especially under conditions that enable hydrolysis.

The application of nanoparticles is not limited to the examples described above, they can also be used for the coating of materials. A popular method for the coating of electrically conductive substrates is electrophoretic deposition. The substrate serves as an electrode at which the charged nanoparticles are deposited. This way, phononic crystals, [15] gas sensors, [16] and composite coatings for possible biomedical applications like implants [17] have been fabricated from polymer nanoparticle dispersions.

The dynamics of particles near the electrode play a crucial role for the success of the deposition. A variety of experimental and computational works examines the motion of microparticles near electrodes. The particle dynamics near an electrode interface are determined by various parameters like the electrolyte concentration [18] and type, [19] as well as the frequency, [20–23] and amplitude [24] of the applied voltage. The phase angle between the frequency of the applied alternating voltage and the particle oscillation has also been studied in the past. [21] Computational works predict the hydrodynamic flow near a colloid at an electrode at which an alternating voltage is applied, [25] the electrophoretic forces acting on such a particle [26] and their varying distance during the application of

an alternating voltage. [27]

There is a lack of studies about the dynamics of nanoparticles near electrodes, probably due to being inaccessible to optical microscopy on which the studies on microparticles rely. Dynamic light scattering (DLS) is a convenient technique to study dynamics of nanosized objects, e.g the diffusional or electrophoretic behavior of nanoparticles. Resonance enhanced dynamic light scattering (REDLS) is a technique that enables the surface-sensitive measurement of the dynamic properties of nanoparticles near a noble metal interface. [28] In this thesis, a multi-angle REDLS setup in which the metal interface along which the surface plasmon propagates doubles as an electrode interface has been build. In contrast to the microscopic studies on the near-electrode behavior of particles, the characteristics of a whole particle ensemble instead of single particles can be observed thereby. The dynamics of nanoparticles under the application of alternating voltages of different strengths and frequencies have been studied in this thesis.

The thesis is structured as follows: In the second chapter, relevant concepts for the nanoparticle stabilization and dynamics near interfaces as well as in electric fields of nanoparticles are introduced. The third and forth chapter explain the methods used in this thesis. The former one reviews the fundamentals of nanoparticle synthesis and characterization while the latter focuses on the methods used for the investigation of their dynamics: The physical background, experimental realization and data analysis of DLS, REDLS, and surface plasmon resonance (SPR) experiments are explained, including detailed information on the setup used for REDLS measurements under the application of electric fields. The results of the nanoparticle synthesis and interpretation of the data obtained from the measurements of their dynamics near electrode interfaces are presented in chapter five. Finally, the improved properties of the functionalized, PLA-based nanoparticles and the insights on their motion near electrode interfaces in context with electrophoretic deposition are summarized in the last chapter.

2. Concepts

2.1. Charged surfaces in electrolytes

Near charged surfaces in electrolytes, the counterions of the electrolyte will form layers near this surface. They are described by the Grahame model which is based on the works of Helmholtz, [29] Gouy, [30] Chapman, [31] and Stern. [32] The distribution of the electrolyte ions near the charged surface is depicted in figure 2.1. The innermost layer which consists of adsorbed, non-hydrated ions is the so called inner Helmholtz layer. In the case of a metal electrode, ions which are already oxidized but not yet hydrated form the inner Helmholtz layer. In surfactant-stabilized colloidal systems, the inner Helmholtz layer consists of the hydrophilic section (or the "head") of the surfactant molecules.

Next to the inner Helmholtz layer, but farther away from the surface, the outer Helmholtz layer is located. It has the opposite charge as the inner Helmholtz layer and consists of hydrated electrolyte ions which are hold in place by Coulomb forces. Due to those strong attractive forces, the ions of the outer Helmholtz layer are immobile.

The outer Helmholtz layer does not fully compensate the charge of the inner Helmholtz layer, therefore the concentration of electrolyte counterions is increased near the charged surface. The area in which an increased concentration of counterions is found is called diffuse layer or outer Stern layer.

For diffusion processes near charged surfaces and for the stabilization of colloids, the potential curves near charged surfaces play a crucial role. These curves can be deduced from the Poisson equation:

$$\nabla^2 \Psi(x,y,z) = \left(\frac{\partial^2}{\partial x^2} + \frac{\partial^2}{\partial y^2} + \frac{\partial^2}{\partial z^2} \right) \Psi(x,y,z) = -\frac{\rho_c(x,y,z)}{\epsilon_0 \epsilon_r}. \qquad (2.1)$$

The Poisson equation relates the potential distribution in space $\Psi(x,y,z)$ to the charge density ρ_c. If we consider the one dimensional case of an endlessly ex-

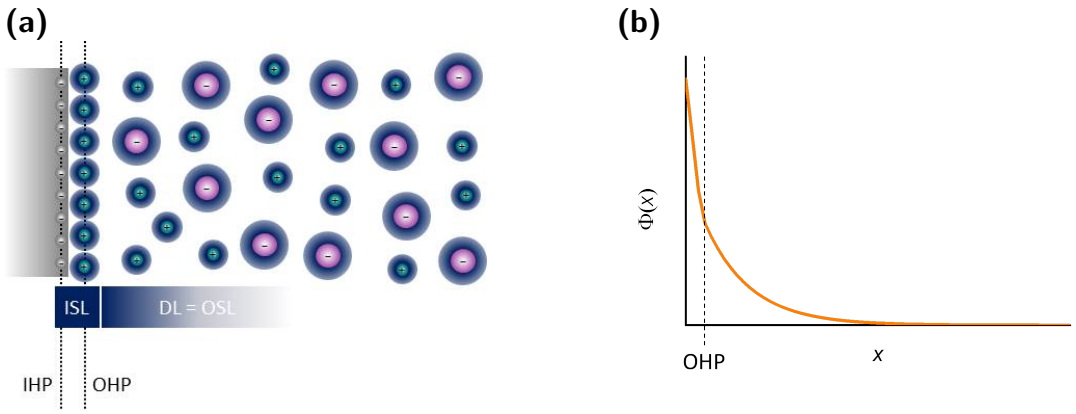

Figure 2.1.: **(a)** Schematic drawing of the electric double layer at a charged surface in an electrolyte and potential-distance curve. IHP and OHP denote the inner and outer Helmholtz plane. ISL is the inner Stern layer and DL the diffuse layer. **(b)** Curve of the absolute potential near the charged surface.

tended, flat, charged surface the Poisson equation simplifies to

$$\frac{d^2\Psi}{dx^2} = -\frac{\rho_c(x)}{\epsilon_0 \epsilon_r}. \tag{2.2}$$

As there is no charge located between the inner and outer Helmholtz plane, the potential is decreasing linearly between those two points as can be proven by two-fold integration of equation 2.2 for $\rho_c = 0$,

$$\Psi(x) = C_1 x + C_2 \tag{2.3}$$

where C_1 and C_2 are constants.

The charge density is no longer zero in the diffuse layer, and the charges are moving. The local ion concentration[1] c_i is related to the work W_i which is needed to bring an ion from a point which is infinitely far away from the charged surface to a distinct position close to it. Therefore, the local ion concentration can be expressed with the Boltzmann equation

$$c_i = c_0 \exp\left(-\frac{W_i}{k_B T}\right) \tag{2.4}$$

[1]For the considered one-dimensional case, $\rho_c = z \cdot e \cdot c$ is valid.

with the thermal energy $k_B T$. The work W_i can be written as

$$W_i = \begin{cases} ze\Psi(x) & \text{for cations} \\ -ze\Psi(x) & \text{for anions.} \end{cases} \tag{2.5}$$

$\Psi(x)$ describes the potential curve near the surface. From now on, we consider the case of a monovalent electrolyte with $z = 1$ to keep the equations simple.

By combining the Boltzmann equation 2.4 and the Poisson equation 2.1, we obtain the following expression for the potential near the surface:

$$\frac{d^2\Psi(x)}{dx^2} = \frac{c_0 e}{\epsilon_0 \epsilon_r} \left(\exp\left(\frac{e\Psi(x)}{k_B T} \right) - \exp\left(-\frac{e\Psi(x)}{k_B T} \right) \right). \tag{2.6}$$

In order to find an expression which connects the potential $\Psi(x)$ directly to the distance from the surface x, we have to integrate equation 2.6. First, we introduce the dimensionless potential Φ for simplicity:

$$\Psi(x) = \frac{k_B T}{e} \Phi(x). \tag{2.7}$$

Rewriting 2.6 leads to [2]

$$\frac{kT}{e} \frac{d^2\Phi(x)}{dx^2} = \frac{c_0 e}{\epsilon_0 \epsilon_r} \left(\exp\left(\Phi(x)\right) - \exp\left(-\Phi(x)\right) \right) = \underbrace{\frac{c_0 e}{\epsilon_0 \epsilon_r}}_{\lambda_D^{-2}} \sinh\left(\Phi(x)\right). \tag{2.8}$$

The newly introduced variable λ_D is the Debye length. As we will see later, it is the distance from the surface at which the potential has decreased to $1/e$ of the surface potential.

After application of the operator $2\frac{d\Phi(x)}{dx}$ on both sides we obtain

$$\underbrace{2 \cdot \frac{d\Phi(x)}{dx} \cdot \frac{d^2\Phi(x)}{dx^2}}_{= \frac{d}{dx}\left(\frac{d\Phi(x)}{dx}\right)^2} = 2 \cdot \frac{d\Phi(x)}{dx} \lambda_D^{-2} \sinh\left(\Phi(x)\right). \tag{2.9}$$

Both sides of 2.9 can be integrated to dx which yields

$$\left(\frac{d\Phi}{dx} \right)^2 = 2\lambda_D^{-2} \cosh\left(\Phi(x)\right) + C_1. \tag{2.10}$$

[2] Remember the trigonometric function $\sinh(x) = \frac{1}{2}\left(e^x - e^{-x}\right)$.

The integration constant C_1 can be determined by inserting the boundary condition

$$\Phi(\infty) = 0 \text{ and } \frac{d}{dx}\Phi(\infty) = 0 \tag{2.11}$$

which accounts for the potential at an infinite distance from the surface being zero and constant, into 2.10:

$$2\lambda_D^{-2}\underbrace{\cosh(0)}_{=1} = C_1 \Leftrightarrow C_1 = -2\lambda_D^{-2}. \tag{2.12}$$

Now we have a full expression for the term

$$\frac{d\Phi}{dx} = \pm\frac{1}{\lambda_D}\sqrt{2\cosh(\Phi(x)) - 2} \tag{2.13}$$

in which only the negative solution has a physical meaning due to the boundary condition that the potential must decrease with increasing distance to the surface.

After separation of the variables x and Φ, we can integrate again to end up with

$$2\ln\left(\tanh\left(\frac{\Phi(x)}{4}\right)\right) = -2\lambda_D^{-1}x + 2C_2. \tag{2.14}$$

Again, the integration constant C_2 can be determined from the boundary condition 2.11 to be

$$C_2 = \ln\left(\frac{\exp\left(\frac{\Phi(0)}{2}\right) - 1}{\exp\left(\frac{\Phi(0)}{2}\right) + 1}\right). \tag{2.15}$$

By inserting 2.1 into 2.14 and solving the equation for $\exp\left(\frac{\Phi}{2}\right)$, we obtain the final expression to calculate the potential $\Phi(x)$

$$\exp\left(-\frac{x}{\lambda}\right) = \frac{\left(\exp\left(\frac{\Phi(x)}{2}\right) - 1\right)\cdot\left(\exp\left(\frac{\Phi(0)}{2}\right) + 1\right)}{\left(\exp\left(\frac{\Phi(x)}{2}\right) + 1\right)\cdot\left(\exp\left(\frac{\Phi(0)}{2}\right) - 1\right)}. \tag{2.16}$$

For low potentials $\Phi \ll {}^{kT}/_{e}$, we can use the the series expansion for $e^x = 1 + x + {}^{x^2}/_2 + ...$ and obtain

$$\exp\left(-\frac{x}{\lambda_D}\right) = \frac{\Phi(x)}{\Phi_0} \Leftrightarrow \Phi(x) = \Phi_0\exp\left(-\frac{x}{\lambda_D}\right) \tag{2.17}$$

which is the linearized Poisson-Boltzmann equation.

2.2. Stabilization of colloids

Apart from everyday applications like in pigment dispersions which are used as paints and coatings, in cosmetic products like lotions, and in foams like industrially produced ice-cream, the stability of colloids is of great importance. In order to achieve long shelf-times and ensure a high product quality, the dispersions, emulsions and foams must be stable, the phases should not separate. Nanoparticles which are designed for biomedical applications are a more sophisticated example for a colloid that should be stable even under extreme conditions like high electrolyte concentrations as found in living cells. Already during nanoparticle preparation, stabilization effects determine the particle size and polydispersity.

The repulsive and attractive forces between two single particles, droplets or bubbles of a colloid which govern its stability are described by DLVO theory. The name of this theory is a tribute to Derjaguin, Landau, Verwey, and Overbeek. [33–35] In the frame of DLVO theory, the interaction forces between two particles in aqueous dispersion are described by a superposition of the attractive van der Waals and the repulsive electrostatic interactions.

The interaction between two dipoles which are either both permanent (Keesom force), permanent in one and induced in the other dipole (Debye force), or both induced (London force) is described by the Van der Waals potential. It decays by the power of six with increasing distance x of the dipoles

$$U_{VdW} = -\frac{C_{orient}}{x^6} - \frac{C_{ind}}{x^6} - \frac{C_{disp}}{x^6}. \tag{2.18}$$

The interaction parameters C_x depend on dipole parameters like the geometry, size, or chemical composition of the respective molecule.

Colloids like nanoparticles are considerably larger than single molecules. Two approaches exist to describe the Van der Waals potential between such bodies. In the Hamaker approach, the interaction energy of two bodies at a center-to-center distance d is described by pairwise summation over the interaction energies of all interacting dipole pairs of the system. For the interaction energy of two spheres

with radii R_1 and R_2, Hamaker obtained [36]

$$U(d,R_1,R_2) = -\frac{A_H}{6}\left(\frac{2R_1R_2}{d^2-(R_1+R_2)^2} + \frac{2R_1R_2}{d^2-(R_1-R_2)^2} + \ln\left[\frac{d^2-(R_1+R_2)^2}{d^2-(R_1-R_2)^2}\right]\right) \tag{2.19}$$

with the Hamaker constant

$$A_H = \pi^2 \cdot C \cdot \rho_1 \cdot \rho_2. \tag{2.20}$$

In equation 2.20, ρ_i is the the atom density in the respective sphere and C the interaction parameter.

For surface-to-surface distances z smaller than the particle radius R_1 or R_2, equation 2.19 simplifies to

$$U(R_1,R_2,z) \approx -\frac{A_H R_1 R_2}{(R_1+R_2)6z} \tag{2.21}$$

$$\overset{\text{for } R_1=R_2}{\approx} -\frac{A_H R}{12z}. \tag{2.22}$$

The according Van der Waals force is the first derivative of the interaction energy 2.22:

$$F_{VdW} = -\frac{A_H R_1 R_2}{(R_1+R_2)6z^2} \tag{2.23}$$

The Hamaker approach includes two major simplifications: First, the approach of pairwise summation of interaction energies which neglects the mutual influence of the dipoles on each other's orientation. Second, it is technically only valid for two interacting bodies in vacuum. If they are separated with a dielectric, quantum effects have to be considered. Lifshitz accounts in his derivation of the interaction energy for those two effects. [37] Laven and Vissers compare the Hamaker constant obtained by the Hamaker and the Lifshitz approach as well as from experimental data. The Hamaker constant according to the first approach is - depending on the volume fraction of the respective phases - up to three times higher than for the two latter approaches. [38]

The second force which acts in colloid stabilization is the force due to the electrostatic potential near a charged surface like the one of a nanoparticle. It is described by the Poisson-Boltzmann potential (equation 2.17).

The third kind of potential existing between to colloidal particles is the Born potential U_{Born} which accounts for the boundary condition that distances smaller than zero are forbidden, or, in other words, that two particles must not overlap. It can be written as

$$U_{rep} = \frac{C_{rep}}{z^{12}}. \tag{2.24}$$

which is a good approximation for the physically more complex term which exactly describes the Pauli exclusion principle.

Adding up the Van der Waals, the Poisson-Boltzmann, and the Born potential, the DLVO potential is obtained:

$$\begin{aligned} U_{DLVO}(z) &= U_{VdW}(z) + \Phi(z) + U_n(z) && (2.25) \\ &= -\frac{-A_H R}{12z} + \Phi_0 \exp(-\frac{z}{\lambda_D}) + \frac{1}{z^{12}}. && (2.26) \end{aligned}$$

The DLVO potential curve for two spheres is depicted in figure 2.2a. At large distances, the potential is close to zero but positive, the dispersion is stable. If the particles approach, they will be trapped at a certain distance due to a local potential minimum: The particles flocculate. Flocculation is a reversible process, the particles can be redispersed by adding e.g. mechanical energy to the system by shaking.

A closer approach of the particles is hindered by the maximum in the particle-particle potential due to Coulomb repulsion. However, in the case of weakly charged particles or high electrolyte concentrations, this maximum can be lowered enough for particles to overcome it as depicted in figure 2.2b. This leads to coagulation, the particles aggregate irreversibly. In the DLVO curve, this state is located at the deeper minimum.

The steep increase of the potential towards $d = 0$ is due to the strongly repulsive Born potential.

2.3. Motion at the solid-liquid interface

The velocity of a particle which is freely diffusing in a dispersant is determined by its thermal energy $k_B T$ and the drag forces F_{drag} exerted by the molecules of the

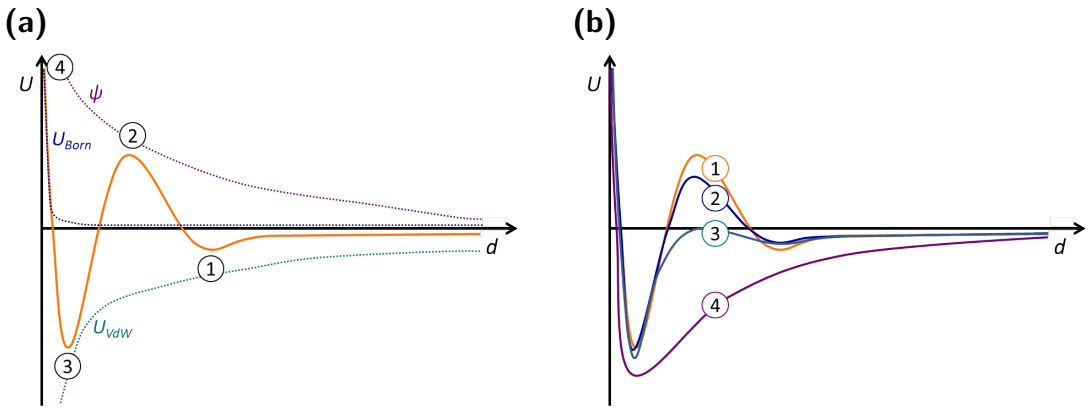

Figure 2.2.: **(a)** The DLVO potential (orange line, –) and the various contributing potentials (dotted lines, ···). The numbered points mark the distances at which flocculation (1), maximum repulsion (2), coagulation (3), and infinite repulsion due to the forbidden overlap boundary condition (4) occur. **(b)** DLVO potential at various electrolyte concentrations. The orange line (–, (1)) corresponds to the lowest electrolyte concentration. With an increasing number of dissolved ions, e.g. in the blue curve (–, (2)) and green curve (–, (3)), the maximum which needs to be overcome for coagulation is lowered. In the vase of the purple line (–, (4)) which refers to the highest electrolyte concentration, there is no Coulomb barrier anymore, particles coagulate immediately.

dispersant. Both contributions are connected by the Stokes-Einstein equation

$$D = \frac{v k_B T}{F_{drag}} = \frac{k_B T}{6\pi\eta R_H} \tag{2.27}$$

with the diffusion coefficient D, the velocity of the particle v, the viscosity of the dispersant η, and the hydrodynamic radius of the particle R_H. The hydrodynamic radius equals the radius of the particle plus its hydrate shell. [39,40] The mean squared displacement of a particle during the time interval τ is

$$\langle x^2 \rangle = 2D\tau\langle v_{\Delta x} \rangle = \frac{2D}{\Delta x}. \tag{2.28}$$

The result is independent of the direction of x, the motion is isotropic. This changes when a solid, impenetrable surface is located near the particle. In this case, its motion is no longer isotropic but can be separated into a vertical component towards or from the surface and a lateral component describing the motion parallel to the surface as depicted in figure 2.3. [41]

Assuming only hydrodynamic interactions between the surface and the particle,

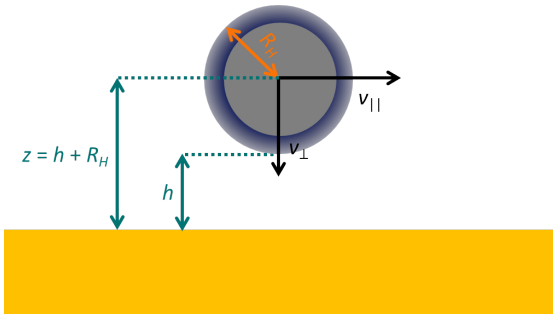

Figure 2.3.: Anisotropic diffusion of a particle near a solid surface. R_H is the hydrodynamic radius of the particle, h marks the distance between the outer border of the hydrate shell of the particle and the solid surface. $v_\perp$ and $v_{||}$ are the normal respective lateral components of the speed vector of the particle.

the vertical and lateral diffusion coefficients $D_\perp$ and $D_{||}$ can be calculated from the overall diffusion coefficient D by the introduction of the correction factors $\Upsilon_\perp$ and $\Upsilon_{||}$ for the respective direction:

$$D_\perp = \Upsilon_\perp D \text{ and } D_{||} = \Upsilon_{||} D \tag{2.29}$$

For the vertical motion, the correction coefficient is expressed by [42]

$$\Upsilon_\perp = \frac{4}{3}\sinh(A)\sum_{n=1}^{\infty}\frac{n(n+1)}{(2n-1)(2n+3)}\left[\frac{2\sinh(A\cdot B)+B\sinh(2\cdot A)}{\left(2\sinh\left(\left(n+\frac{1}{2}\right)A\right)\right)^2 - B^2\sinh^2(A)}\right] \tag{2.30}$$

with $A = \operatorname{arccosh}\left(\frac{z}{R_H}\right)$ and $B = 2n-1$.

For large distances z between the particle and the surface, eqn. 2.30 simplifies to [43]

$$\Upsilon_\perp \approx \left(1 - \frac{9R_H}{8z}\right)^{-1}. \tag{2.31}$$

The lateral correction coefficient $\Upsilon_{||}$ accounts for the anisotropy of the drag forces acting on the particle: They are significantly higher at the side of the particle which is oriented towards the surface compared to the side facing the free space. Therefore, the surrounding fluid also applies a torque M on the sphere. The drag force and torque are expressed by

$$F_{drag} = 6\pi\eta R_H\left(v_{||}F_{drag,t} + \omega R_H F_{drag,r}\right) \tag{2.32}$$

and

$$M = 8\pi\eta R_H^2 \left(v_{||} M_t + \omega \cdot R_H M_r\right). \tag{2.33}$$

If the particle can rotate freely, equation 2.33 is zero and we can plug it into equation 2.32 to express the correction coefficient by

$$\Upsilon_{||} = \frac{D}{D_{||}} = F_{drag,t} - \frac{M_t}{M_r} \cdot F_{drag,r} \tag{2.34}$$

For equation 2.34, only a numerical solution exists which has been found by O'Neill. [44] However, if we assume a distance between the particle and the surface which is larger than $z > 1.4R_H$, equation2.34 simplifies to

$$\Upsilon_{||} \approx \left(1 - \frac{9}{16}\frac{R_H}{z} + \frac{1}{8}\left(\frac{R_H}{z}\right)^3 - \frac{45}{256}\left(\frac{R_H}{z}\right)^4 \frac{1}{16}\left(\frac{R_H}{z}\right)^5\right)^{-1} \tag{2.35}$$

Equation 2.35 can be solved analytically. [45] The results of equations 2.30 and 2.35 for two different particle sizes are depicted in figure 2.4. The graph shows that the correction coefficients Υ are always below one. This means, the surface slows down particle diffusion. With increasing distance between the particle and the surface, both correction coefficients approach one: the particle diffusion is no longer affected by the surface. The distance at which the effect of the surface can be neglected is higher for larger particles than for smaller particles.

2.4. Particle motion in electric fields

A charged particle which is diffusing in an electrolyte to which an electric field $\vec{E}$ is applied experiences an additional electric force

$$\vec{F}_{el} = q_{app}\vec{E} \tag{2.36}$$

which is proportional to the apparent particle charge q_{app}. This charge is the net charge of the particle itself plus the charge of the ions in its hydrate shell (figure 2.5).

This charge can be calculated from the ζ-potential of the particle which is the potential at the shear plane (figure 2.5). In the case of particles which are large compared to the Debye length of the system, $R_H \gg \lambda_D$, the Grahame equation

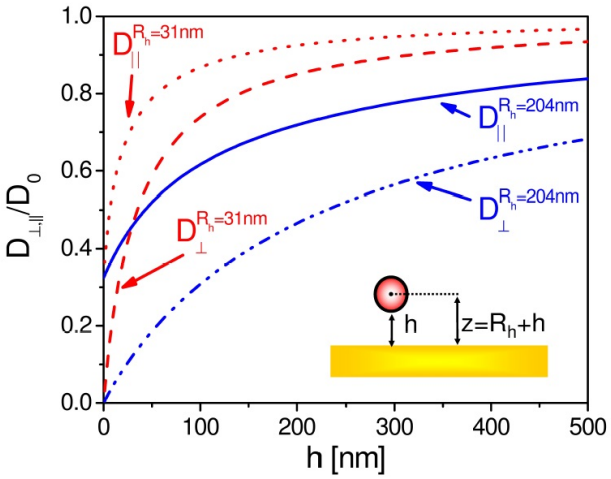

Figure 2.4.: Corrected diffusion coefficients for the motion parallel and normal to the solid surface for two different particle radii. The curves are based on the first one hundred terms of equation 2.30 and on equation 2.35. Reprinted with permission from PhD thesis of M. A. Plum. [46]

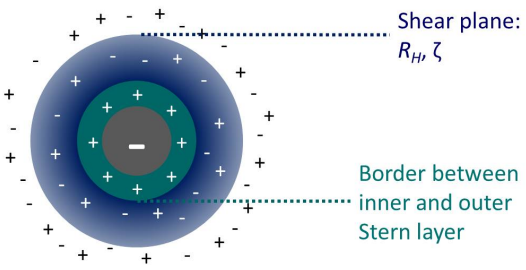

Figure 2.5.: A negatively charged particle (gray) in an electrolyte. The inner Stern layer consists of the surface charge of the particle and the immobile cations bound at the particle surface (green). The outer Stern layer or diffuse layer is depicted in blue. The cation concentration is higher than the anion concentration in this layer. The ions within this layer are mobile. The inner and outer Stern plane are diffusing with the particle, therefore the shear plane marks the border between the outer Stern layer and the continuum.

can be employed: [47]

$$\sigma_c = \sqrt{8c_0\epsilon_0\epsilon_r k_B T}\sinh\left(\frac{e\zeta}{2kT}\right). \tag{2.37}$$

It simplifies for the case of low potentials where the series expansion

$$\sinh(x) = x + {}^{x^3}/_{3!} + ... \tag{2.38}$$

is applicable to

$$\sigma_c = \frac{\epsilon\epsilon_0\zeta}{\lambda_D}. \tag{2.39}$$

The particle charge can be calculated from the surface charge density σ_c by multiplication with the surface area A of the particle,

$$q_{app} = \sigma_c A = \frac{\epsilon_0\epsilon_r\zeta}{\lambda_D} 4\pi R_H^2. \tag{2.40}$$

Just as in the case of undisturbed diffusion, particles moving at a certain speed v in a viscous medium are decelerated by drag forces. The thermal velocity of particles is determined by the balance of thermal motion energy and drag forces in Brownian motion as described by the Stokes-Einstein equation (equation 2.27), the electrophoretic velocity v_{el} of a particle in an electric field is determined by the balance of the electric force and the drag force. The drag force is described by the Stokes equation

$$\vec{F}_{drag} = 6\pi\eta R_H \vec{v}. \tag{2.41}$$

Assuming the above mentioned condition $F_{drag} = F_{el}$, we end up with

$$v_{el} = \frac{q_{app}\vec{E}}{6\pi\eta R_H} \tag{2.42}$$

$$= \begin{cases} \frac{\epsilon\epsilon_0\vec{E}\zeta}{\eta} & \text{for } \lambda_D \ll R_H \\ \frac{2}{3}\frac{\epsilon\epsilon_0\zeta\vec{E}}{\eta} & \text{for } \lambda_D \gg R_H \end{cases} \tag{2.43}$$

The first case is the Smoluchowski [48], the second the Hückel [49] approximation. Particles with radii in between those two extremes are covered by Dukhin's theory in which a function $f(\frac{R}{\lambda_D})$ is multiplied to equation 2.43. [50,51]

2.5. Electrophoretic deposition

Electrophoretic deposition (EPD) is a coating process in which dispersed particles are driven towards an electrode by electrophoresis and aggregate there in a mono- or multilayer. The effect was first observed by Reuß in 1809 when he studied the behavior of clay particles in an electric field. [52] More than one century later, several patents existed, e.g. for the electrodeposition of resins to fabricate electric insulations or for the electrophoretic deposition of thorium dioxide particles to produce electron tubes. Around this time, Hamaker and Verwey started to think about and experiment on the mechanism behind EPD. They published a first possible mechanism of EPD in 1940. [53,54] More than half a century later, in the 1990s, three more mechanism of EPD have been suggested. I will introduce all of them below. More details about EPD and can be learned from the review of Besra [55] or the up-to-date textbook edited by Dickerson and Bocaccini [56]. Specifically EPD in alternating voltages in particular is reviewed by Neirinck. [57]

According to the Hamaker's and Verwey's model, particles migrating to the oppositely charged electrode exert a repulsive force on particles already located nearby the electrode when they are approaching closer than the distance of the Coulomb barrier (point 2 in figure 2.2). This forces the particles even closer to the electrode where they aggregate.

Grillon and his coworkers suggested that an electrochemical reaction is the reason which causes the particles to aggregate at the electrode surface. [58] They suggest that the particle discharges at the electrode. Now that it has ζ-potential close to zero, other particles can closely approach the particle and also discharge at the electrode. This mechanism can only explain the first layer of electrophoretic deposits. Particles in higher layers are not in direct contact with the electrode and therefore cannot discharge.

Koelmans calculated that due to the increased ion concentration in the diffuse layer near an electrode, the particle distances are in the flocculation regime. [59] A proof for the flocculation is that Koelmans showed in experiments that the deposit redispersed again if the field has been switched off.

Sarkar and Nicholson suggested that the thinning of the electrochemical double layer around the particles is the reason for their deposition at the electrode. [60] As the particle is moving towards the electrode, its counterions in the diffuse layer

are driven in the opposite direction, to the counterelectrode.[3] The diffuse layer is thinning as the charge of the counterion within is neutralized by ions of the same charge as the particle which are also migrating towards the same electrode as the particle. Eventually, the particles have fully lost their hydrate shell and adsorb at the electrode or on top of the already deposited particle layer.

Which of the four mechanisms explains the results of a specific system best depends on several parameters like e.g. the dispersant, the particle type (polymer or inorganic) and size (nano- oder microparticles), or the electrode type.

[3] In the case of ceramic particles, the counterions are from the liquid, e.g. H^+ and OH^- in water.

3. Chemical Methods

3.1. Polymerization reactions

The manifoldness of polymerization types is divided into step growth and chain growth polymerizations. Polycondensations and -additions belong to the former class; radical, ionic and coordinative polymerizations to the latter one. In the following sections, the radical and coordinative polymerization will be discussed. For references on the other types of polymerization, the textbooks by Tieke [61] or Koltzenburg, Maskos and Nuyken [62] are recommended.

3.1.1. Radical polymerization

Radical polymerizations are suitable for the polymerization of monomers with vinyl groups. They can be conducted in aqueous or organic solutions as well as in bulk. To start a radical chain growth reaction, a radical initiator is needed. Initiator molecules readily form radicals when heated. The initiator has to be chosen according to the reaction environment, e.g. potassium persulfate $K_2S_2O_8$ is soluble in water and azo initiators like V70 (figure 3.1) are soluble in organic solvents.

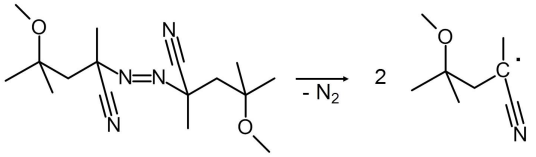

Figure 3.1.: Structure and radical formation of the azo initiator V70.

The radicals resulting from the decay of the initiator molecules

$$\mathrm{I{-}I} \longrightarrow 2\ \mathrm{I}\cdot \tag{3.1}$$

add to the vinyl group of the monomers

$$\mathrm{I}\cdot + \mathrm{M} \longrightarrow \mathrm{I{-}M}\cdot \tag{3.2}$$

and thereby start the chain growth reaction

$$\mathrm{I{-}M}\cdot + \mathrm{M} \longrightarrow \mathrm{I{-}M{-}M}\cdot . \tag{3.3}$$

The reaction is terminated either by the combination of two radical molecules

$$\sim\!\sim\!\sim\mathrm{M}\cdot + \sim\!\sim\!\sim\mathrm{M}\cdot \longrightarrow \sim\!\sim\!\sim\mathrm{M{-}M}\sim\!\sim\!\sim \tag{3.4}$$

or by disproportionation which leads to one saturated (sat) and one unsaturated (vin) polymer

$$\sim\!\sim\!\sim\mathrm{M}\cdot + \sim\!\sim\!\sim\mathrm{M}\cdot \longrightarrow \sim\!\sim\!\sim\mathrm{M}^{\mathrm{sat}} + \sim\!\sim\!\sim\mathrm{M}^{\mathrm{vin}}. \tag{3.5}$$

The degree of polymerization is determined by the reaction rate of the termination reactions, the temperature and the transfer constants of the monomer, polymer, and solvent. Some solvents such as halogenated hydrocarbons have high transfer constants. Those solvents readily accept the radical property of a growing polymer chain. For example,

$$\sim\!\sim\!\sim\mathrm{CH_2}\cdot + \mathrm{CHCl_3} \longrightarrow \sim\!\sim\!\sim\mathrm{CH_3} + \mathrm{CCl_3}\cdot \tag{3.6}$$

In order to obtain polymers of high molecular weight, solvents with low transfer constants such as benzene or toluene should be used preferably.

3.1.2. Coordinative polymerization

The most prominent example of a coordinative polymerization which is catalyzed by an organometallic compound is the Ziegler-Natta polymerization of olefins. [63,64] As part of this thesis, poly(lactic acid) (PLA) has been synthesized by coordinative ring-opening polymerization which is catalyzed by aluminum- or tin-based metal-alkoxides. The most common catalyst is tin(II) bis(2-ethylhexanoate) $\mathrm{Sn(Oct)_2}$. [65–67] Alcohols act as cocatalysts in this reaction. They substitute the ethylhexanoate ligands at the tin ion and thereby initiate the re-

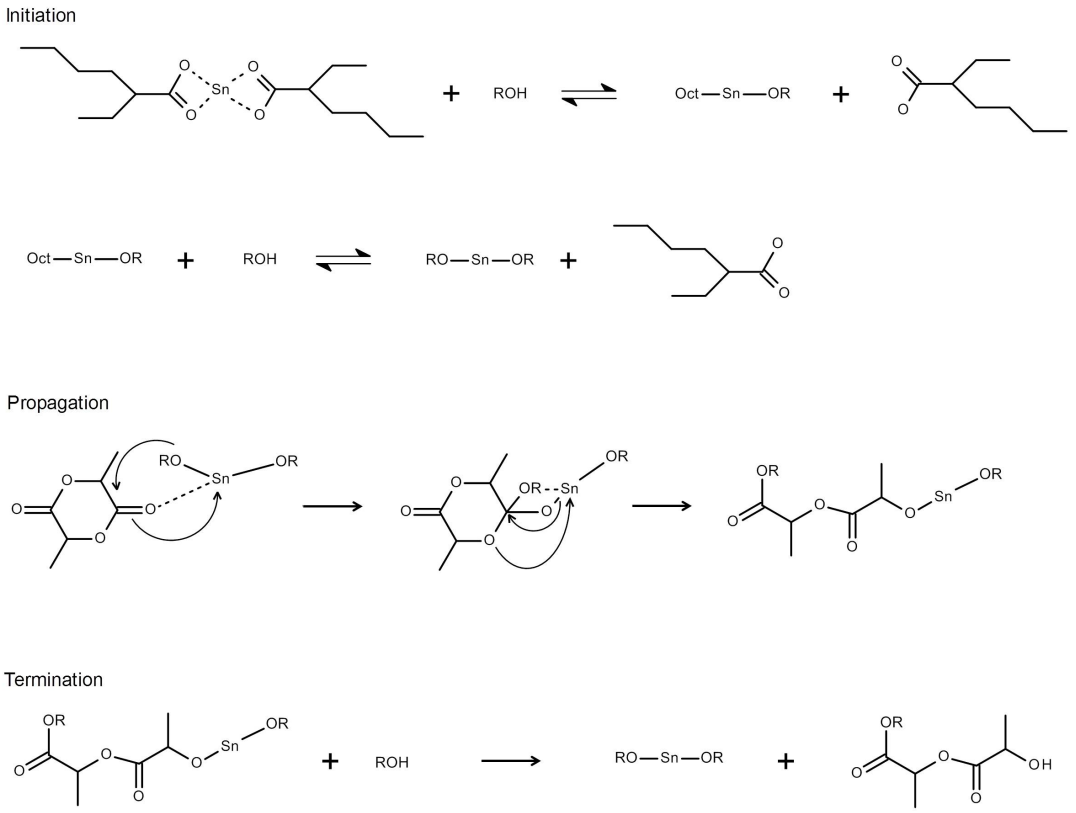

Figure 3.2.: Mechanism of the coordinative ring-opening polymerization of lactide.

action (figure 3.2). A lactide molecule becomes oriented at the metal ion by coordination of the oxygen atom of the carbonyl group and the simultaneous formation of a bond between the oxygen of the alcohol and the carbon atom of the carbonyl group. In the following insertion step, the coordination by the carbonyl oxygens loosens and a bond between the oxygen atom in the lactide ring and the tin ion forms instead which leads to an opening of the ring. By coordination of another lactide molecule and its insertion into the chain which has just started, the polymerization progresses. It is terminated by the reaction of alcohol or water with the polymer-metal complex. The reaction can be carried out in bulk or in solution, e.g. in xylene.

3.1.3. Copolymerization

A polymerization reaction with two different monomers in the reaction mixture may result in a copolymer. In a so-called ideal or statistical copolymer, the

monomer composition of the polymer chain equals the concentration ratio of the reaction mixture. However, the reaction rates k_{ij} of the four chain growth reactions occurring in a copolymerization of comonomers A and B might be different:

$$\sim\sim\sim\mathrm{A}\cdot + \mathrm{A} \xrightarrow{k_{11}} \sim\sim\sim\mathrm{AA}\cdot \tag{3.7}$$

$$\sim\sim\sim\mathrm{A}\cdot + \mathrm{B} \xrightarrow{k_{12}} \sim\sim\sim\mathrm{AB}\cdot \tag{3.8}$$

$$\sim\sim\sim\mathrm{B}\cdot + \mathrm{A} \xrightarrow{k_{21}} \sim\sim\sim\mathrm{BA}\cdot \tag{3.9}$$

$$\sim\sim\sim\mathrm{B}\cdot + \mathrm{B} \xrightarrow{k_{22}} \sim\sim\sim\mathrm{BB}\cdot \tag{3.10}$$

Based on the assumption that the reaction rates k depend only on the chain end and not on other parameters of the polymer, e.g. the chain length, the composition of the copolymer is given by the copolymerization or Mayo-Lewis equation [68]

$$\frac{d[A]}{d[B]} = \frac{[A]\,(r_1[A] + [B])}{[B]\,(r_2[B] + [A])}. \tag{3.11}$$

As the comonomer concentrations $[A]$ and $[B]$ change during the progress of the reaction, the polymer composition also varies. The reactivity ratios $r_1 = {}^{k_{11}}/_{k_{12}}$ and $r_2 = {}^{k_{22}}/_{k_{21}}$ can be determined from the Fineman-Ross plot of the respective copolymer (figure 3.3). The Fineman-Ross plot of a copolymerization is experimentally determined by carrying out the copolymerization with various initial concentration ratios, stopping it at low conversions and analyzing the polymer as well as the monomer composition.

The reactivity ratios can also be determined semiempirically by the Q-e scheme which has been developed by Alfrey and Price. [69] Within this concept, a reactivity value Q and polarity value e are assigned to each monomer. Those values are set in comparison to those of styrene which are $Q = 1$ and $e = -0.8$ by deliberate assignment. The reactivity ratios are

$$r_1 = \frac{Q_1}{Q_2} \exp\left(-e_1\,(e_1 - e_2)\right) \tag{3.12}$$

$$r_2 = \frac{Q_2}{Q_1} \exp\left(-e_2\,(e_2 - e_1)\right). \tag{3.13}$$

The reactivity ratios depend on the polarity of the comonomer as well as on steric and resonance effects stabilizing the respective reactive species. Therefore, the reactivity ratios are only given for one type of reactive species, e.g. the anion. Its

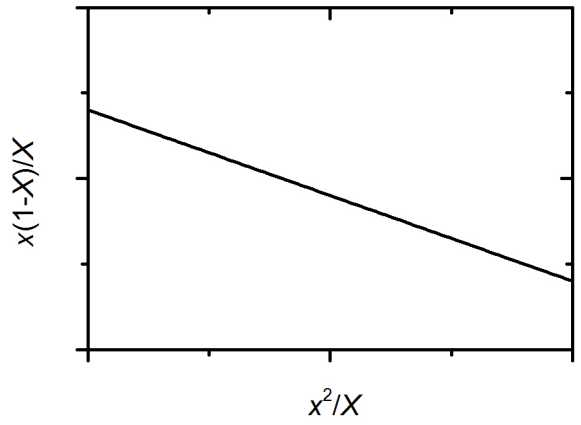

Figure 3.3.: Fineman-Ross plot of a copolymerization with the initial comonomer concentration ratio $x = {}^{[A]}/_{[B]}$ and the change of the comonomer ratio $X = {}^{d[A]}/_{d[B]}$.

value might be different from the reactivity ratio for the radical species. If the reactivity ratios of both monomers are similar, an ideal copolymer is formed. If the monomers differ considerably in polarity and reactivity, alternating copolymers may result from the reaction.

3.2. Polymer nanoparticle formulation

Nanoparticles from preformed polymer can be prepared by a variety of processes, e.g. emulsion solvent evaporation [70] or emulsion solvent diffusion, [5] double emulsion, [71] nanoprecipitation, [72] or the salting out method. [73] The emulsion solvent evaporation process is especially used if drugs or contrast agents are encapsulated in the polymer matrix. [74–77] Since its development in the 1970ies, [70,78] the method has been improved and refined in order to fabricate nanoparticles which meet the specific demands of biomedical applications like biocompatibility or colloidal stability under physiological conditions. [79–81]

The principle of the miniemulsion solvent evaporation process is depicted in figure 3.4. The polymer of choice is dissolved in a hydrophobic solvent of low boiling point, e.g. chloroform or tetrahydrofuran. An aqueous solution of a surfactant, e.g. sodium dodecylsulfate (SDS), is added to the reaction vessel. High shear forces, e.g. due to ultrasonication, lead to the emulsification of the mixture consisting of two immiscible solvents. The solvent droplets of the disperse

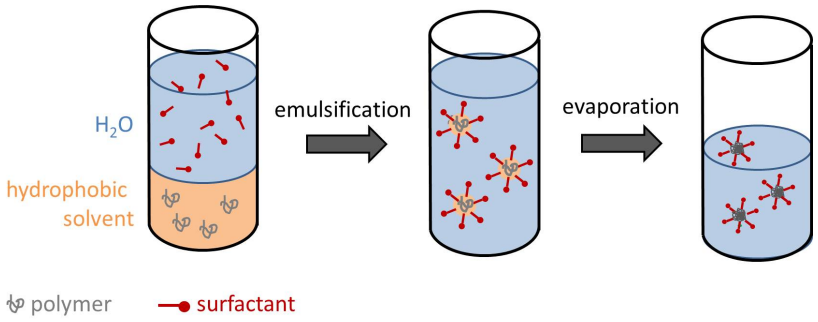

Figure 3.4.: Principle of the miniemulsion solvent evaporation method for the fabrication of nanoparticles from preformed polymer.

phase which contain the polymer are stabilized by surfactant molecules. In a second step, the volatile organic solvent is evaporated from the miniemulsion by heating, leaving behind one nanoparticle from each droplet.

The particle radii are determined by the interplay of several parameters like the temperature during solvent evaporation, [82] the concentration of the surfactant [83], the properties of the organic solvent, [84] and the duration of ultrasonication. [85]

As several experimental studies have shown, the width of the size distribution of the nanoparticles is already determined in the emulsification step. In later stages of the reaction, no further broadening of the size distribution due to coalescence or Ostwald ripening has been found for polystyrene or poly(lactic acid) [86–88]. Especially Ostwald ripening might be an issue if the polymer is slightly soluble in water which increases the probability of its diffusive migration from smaller to larger droplets. [89]

Polymer nanoparticles can also be prepared directly from the corresponding monomer in a miniemulsion polymerization. [90] In this case, a radical initiator is dissolved in the monomer. The solution is dispersed in an aqueous surfactant solution and the polymerization is started by heating or UV-light. Each droplet can be imagined as a nanoreactor in which a bulk polymerization takes place. No evaporation of solvent is needed, making this approach attractive for continuous synthesis in flow reactors.

The advantage of the miniemulsion solvent evaporation process above the miniemulsion process is that preformed polymer can be used. The resulting particles are therefore free from impurities like monomer remains or side products. Ad-

ditionally, it can be applied to polymers which demand a more sophisticated synthetic approach, e.g. block-copolymers, or polymers which require another polymerization as the radical one. It also allows the encapsulation of other materials like drugs or magnetite nanoparticles which might be affected by or inhibit the polymerization.

3.3. Characterization methods

The polymers and nanoparticles synthesized within this thesis have been characterized in terms of structure, charge, and size. In this chapter, the working principles of the methods used are described.

3.3.1. Potentiometric titration

The determination of the number of acidic or basic groups in a polymer chain often cannot be done by regular titration because the equivalence point might not be known or no common solvent for indicator and polymer exists. Potentiometric titration circumvents those challenges. A pair of electrodes is used to measure the potential between the analyte solution and a reference electrode. This potential changes with the addition of titrant. The equivalence point is the point at which the titration curve has a point of inflection, i.e. its slope has a maximum or minimum.

3.3.2. Electron microscopy

The resolution of a microscope is determined by the diffraction limit

$$d = \frac{\lambda}{2n\sin(\alpha)}. \tag{3.14}$$

The minimum distance d required for two points to be resolved depends on the wavelength λ, the refractive index of the medium between the object and the objective n, and the opening angle of the lens, 2α. From equation 3.14, it follows that only structures larger than approximately 200 nm can be resolved by light microscopy. However, with shorter wavelengths, the resolution can be increased. This can be achieved by using accelerated electrons instead of visible light for imaging. The first electron microscope has been built by Knoll and Rustka. [91] It

was a transmission microscope which is very similar to the transmission electron microscopes (TEM) used nowadays. Electrons are accelerated by a voltage between 50 and 200 kV and focused on the sample by electromagnetic lenses. The electrons and nuclei of the sample interact with the electron beam. They are either scattered elastically or inelastically, or they are absorbed or transmitted. The lower the proton number of the atoms in the sample, the more electrons are transmitted and arrive at the detector. Areas where atoms with high proton numbers are located in the sample appear as dark spots on a TEM image. Sub-Ångström resolution has been achieved with TEM. [92]

An extension of TEM is cryo-TEM. [93] The sample holder and the electron-emitting tip are cooled by liquid nitrogen, therefore allowing the imaging of sensitive materials like biological or polymer samples which would suffer from severe beam damage in regular TEM. [94]

In scanning electron microscopy (SEM), lower accelerating voltages (0.5 to 30 kV) can be used because the detector is located at the same side of the sample as the electron source. In this case, mainly the so-called secondary electrons which are leaving the sample surface due to inelastic scattering of the electron beam are detected. More electrons are leaving the sample positions where it has peaks, at less elevated areas they are easily absorbed by surrounding atoms. Therefore, elevated areas appear brighter in SEM images, leading to a 3D appearance. The resolution of a regular SEM is in the range of 1 to 20 nm. [95]

3.3.3. Surface charge measurements

The surface charge of a colloidal particle can be determined by titration with a polyelectrolyte. [96] The amount of titrant used until the streaming potential of the particle dispersion becomes zero is measured. The streaming potential is the potential difference between two points of a measurement cell in which the particle and counterion charges have been separated by shear. In practice, this is done by vertically moving a cylinder in a very narrow measurement cell (figure 3.5). The potential between an electrode at the bottom and another electrode at the top of the cell is measured. For the titration of the negatively charged particles prepared in this thesis, the polycation poly(diallyldimethylammonium chloride) PDADMAC (figure 3.6) has been used. The polyelectrolyte molecules strongly adhere to the particle surface and are not sheared by the moving cylinder, therefore they neutralize the particle charge.

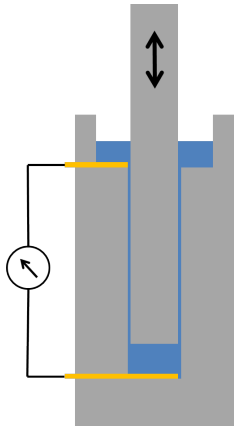

Figure 3.5.: Charge titration setup. The gray cylinder marked with the arrow is moving up and down, thereby creating a shearing potential in the particle dispersion (blue) which is measured between the gold electrodes.

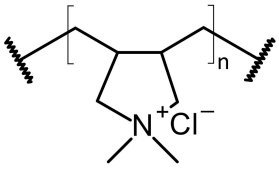

Figure 3.6.: Structure of PDADMAC.

The ζ-potential of a particle is directly related to the surface charge of a particle by the Grahame equation (equation 2.40). ζ-potential analyzers are based on electrophoretic light scattering. [97,98] In brief, moving particles Doppler shift the frequency of a laser beam when they scatter it. Therefore, the frequency spectrum of a particle undergoing only thermal motion shows one single, broad peak. Its center is located at the frequency of the incident beam and its width relates to the diffusion coefficient of the particle. If an electric field is applied on the sample, the particles additionally undergo electrophoresis. This directed motion leads to a shift of the peak caused by the nanoparticle motion in the frequency spectrum. However, its width remains unchanged as it is only determined by the isotropic Brownian motion which is still present. From the frequency shift, the electrophoretic velocity v_{el} and therefore the mobility $\mu_{el} = {}^{v_{el}}/_{E}$ are directly related to the Doppler shift of the particles. If other properties like salt concentration and particle radius are known, the ζ-potential can be calculated from this value according to a previous chapter (equation 2.43).

3.3.4. Fluorescence correlation spectroscopy

The diffusion coefficient and therefore hydrodynamic radii of fluorescent species, e.g. dye-labeled nanoparticles, can be determined by fluorescence correlation spectroscopy (FCS). [99,100] A confocal setup is used to detect the photons emitted by the sample due to fluorescence. Only fluorescent species inside the confocal volume which is determined by the lenses and pinholes used in the detection beampath contribute to the measured intensity. The sample concentrations used in FCS are very low, in time-average, typically only one fluorescent species is located inside of the confocal volume. The detected fluorescence intensity is fluctuating with time as the molecules are entering and leaving the confocal volume due to the diffusion of the molecules. If the time-dependent intensity fluctuations $I(t)$ are autocorrelated,

$$G(t') = \frac{\langle I(t)I(t+t')\rangle}{\langle I(t)\rangle^2} - 1, \tag{3.15}$$

a function which depends on the number of fluorescent species in the confocal volume N, the characteristic diffusion time τ and the structure parameter k is obtained:

$$G(t') = 1 + \frac{1}{N} \cdot \frac{1}{1 + \frac{\tau}{t'}} \cdot \frac{1}{\sqrt{1 + \frac{t'}{k^2 \tau}}}. \tag{3.16}$$

The structure parameter accounts for the geometry of the confocal volume which is defined by the focus and the pinholes. The diffusion coefficient is extracted from equation 3.16 using the equation

$$D = \frac{\omega_0^2}{4\tau} \tag{3.17}$$

in which ω_o is the half-width length of the Gaussian profile in the xy-plane of the confocal volume. The hydrodynamic radius can be evaluated with the Stokes-Einstein relation (equation 2.27).

Dynamic light scattering (DLS) is another method to determine the radius of a nanoparticle spectroscopically. The explanation and description of this method is found in the next chapter.

3.4. Experimental details

3.4.1. Materials

2-Hydroxyethyl methacrylate (HEMA, $\geqslant$ 99%), tin(II)ethylhexanoate ($SnOct_2$, 92.5-100%), L-lactide ((3S)-cis-3,6-dimethyl-1,4-dioxane-2,5-dione, 98%), sodium dodecylsulfate (SDS, $\geqslant$ 99%), anhydrous toluene (99.8%), and chloroform ($\geqslant$ 99.9%) were purchased from Sigma-Aldrich and used as received. 2,2'-Azobis(4-methoxy-2,4-dimethyl valeronitrile) (V70, 10 h decomposition half-time at 30 °C) was purchased from Wako Chemicals GmbH and used as received. Biomer L9000 (PLLA, $M_N \approx 66\,500$ g/mol and $M_W \approx 145\,000$ g/mol, determined by GPC in chloroform) was supplied by Biomer, Germany. Acrylic acid (AA, 99%) and methacrylic acid (MAA, 99%) were purchased from Sigma-Aldrich and purified by column chromatography. The synthesis of hydrophobic dye from the BODIPY family, B612-MA, was done by A. Turschatov (MPI-P) according to a previously published procedure. [101]

3.4.2. Synthesis of HEMA-OLA

Two different HEMA-OLAs have been synthesized in a bulk polymerization according to the procedure published by Ishimoto et al. [102] Briefly, in an 18 mL pressure tube, 7.24 g (50 mmol) L-lactide were melted in an oil bath at 130 °C. The melt was purged with N_2 for 5 min. A mixture of 0.87 g (6.7 mmol) HEMA and 8 mg $Sn(Oct)_2$ was injected by syringe. The mixture was magnetically stirred at 130 °C for 3 h. A clear and colorless, highly viscous liquid was obtained. It was dissolved in 15 mL chloroform and washed once with ca. 10 mL 1 N HCl and four times with ca. 10 mL MilliQ-H_2O. The organic phase was recovered and the chloroform removed in vacuum. Another batch was synthesized the same way using 2.49 g (17.3 mmol) of L-lactide, 0.50 g (3.9 mmol) of HEMA, and 5 mg $Sn(Oct)_2$. Alternatively, in a three neck round-bottom flask equipped with a magnetic stir bar and a reflux condenser, lactide (7.24 g, 50 mmol) was dissolved in 30 mL p-xylene at 100 °C. Nitrogen was bubbled through the solution for 15 min and during the following injection of a mixture of HEMA and $Sn(Oct)_2$. The temperature was raised to 130 °C while stirring. After 1 h, the colorless product precipitated from the solution. Stirring and heating were ued for 4 h in total. Afterwards, the mixture was cooled down to 1 °C to complete the precipitation. The supernatant was removed and the precipitate dried in vacuum (80 °C, 2 h). To purify the product, the same routine as described above has been followed.

3.4.3. Synthesis of carboxyl-functionalized copolymers

180 mg of the heavier HEMA-OLA synthesized in bulk (B2) and various amounts of methacrylic and acrylic acid were each dissolved in 1 mL of anhydrous toluene (3 mg and 11 mg of AA, 4 mg and 13 mg of MAA for a molar ratio of 1:1 and 1:3, respectively). The solutions were mixed in an 18 mL pressure tube using a magnetic stirrer while bubbling argon for 20 min. A solution of 10 mg V70 (32.5 mmol) in 500 µL anhydrous toluene was injected under argon atmosphere and the pressure tube sealed afterwards. The mixture was heated to 60 °C and magnetically stirred overnight. After cooling to room temperature, toluene was removed using a rotary evaporator. Non-grafted AA or MAA, respectively, were removed by dissolving the product in chloroform and washing with 1 N HCl and with water. The product was recovered by drying in vacuum at 40 °C for 14 h. The viscous, colorless product was stored under argon at −20 °C.

3.4.4. Synthesis of the fluorescent copolymer

In an 18 mL pressure tube, 200 mg of HEMA-OLA and 2 mg of B612-MA have been dissolved in 1.3 mL anhydrous toluene. Argon was bubbled for 30 min to degas the solution. 18 mg of V70 were added and the solution was magnetically stirred at 60 °C for 24 h. The crude product was recovered by evaporation of the solvent in vacuum. It was washed with ethanol and dried for 24 h in vacuum.

3.4.5. Preparation of nanoparticles

Nanoparticles were prepared using the miniemulsion solvent evaporation procedure. The organic phases of the miniemulsions were prepared as follows:

One step route PLLA (210 mg), HEMA-OLA (90 mg), V70 (5 mg), and MAA (7 mg) were separately dissolved in 10 g of chloroform in total. All solution were combined to obtain the organic phase for the miniemulsion solvent evaporation step.

Two step route For the functionalized particles, PLLA (210 mg), and MAA-HEMA-OLA (90 mg) or (B612-MA)-HEMA-OLA (90 mg) were separately dissolved in 10 g of chloroform in total and then combined to obtain the organic phase for the miniemulsion solvent evaporation step. For the control sample, PLLA (210 mg) and HEMA-OLA (90 mg) were separately dissolved in 10 g of chloroform in total and then combined to yield the organic phase for the miniemulsion solvent evaporation step. All organic solutions were homogenized using a shaker at 400 rpm. In 50 mL beakers, they have each been overlaid with a solution of 144 mg SDS in 24 g MilliQ-H_2O. The emulsification was carried out by ultrasonication of the mixtures while cooling in an ice bath (Branson Sonifier W450 Digital, 0.5 inch tip, 70% amplitude, 3 min pulsed sonication (30 s on, 10 s off). The miniemulsion was transferred to a 50 mL wide-neck round-bottom flask. In the open flask which was eqipped with a magnetic stirbar, the miniemulsion was stirred vigorously for two hours at 60 °C to evaporate the chloroform. Then, about 5 mL of water were added afterwards to compensate evaporated water and the flask was sealed with a glass stopper. Stirring and heating were continued overnight. After cooling to room temperature, excess SDS has been removed by dialysis (Cellulose membrane, MWCO = 14 kDa, Carl Roth GmbH + Co. KG).

The dispersions were stored at 4 °C until further use.

3.4.6. Characterization

^{1}H NMR spectra were taken on a Bruker Avance 250 or Bruker Avance 500 spectrometer, using deuterated solvents from Carl Roth GmbH & Co. KG. Molecular weights and distributions were determined by GPC (Polymer Standards Services columns; 106, 104, and 500 Å), with THF as eluent at 30 °C, flow rate 1.00 mL/min, and differential refractive index and fluorescence detectors (Shodex RI 101, PSS SECurity VWD).

The apparent molecular weights and polydispersities (M_W/M_N) were determined with a calibration based on linear polystyrene standards using WinGPC software from PSS. Nanoparticle diameters were determined by dynamic light scattering (DLS) measurements using the setup described in section 4.1. The scattering angles were varied between 30° and 120° for each sample. By performing linear fits of the plots of the first order decay rates from the cumulant fit versus the square of the scattering angle q^2, the hydrodynamic radii were obtained. The PDIs are averages of the cumulant fit results obtained for the individual scattering angles. The fitting results were cross-checked by CONTIN fits.

Absorption spectra have been measured using a Perkin Elmer Lambda 900 spectrometer and analytically grade solvents.

ζ-potential measurements were carried out with a Delsa Nanospectrometer (Beckman Coulter). The results represent the average of three consecutive measurements.

The amount of charged groups at the particle surface was determined by polyelectrolyte titration using a combination of Mütek PCD-04 (BTG Instruments GmbH) and a 702 SM Titrino unit (Metrohm Switzerland). 1 mM aqueous poly(diallyldimethylammonium chloride) (Sigma-Aldrich) was used as a titrant. The particle dispersions were titrated at pH 2.5 and pH 9 three times each. The charge arising from the carboxyl groups was determined by subtraction of the averaged titrant consumption at pH 2 from the average consumption at pH 9. For the potentiometric titration, the copolymer was dissolved in a THF/water mixture and NaOH (0.1 M) was used for titration. The particles have been imaged with a Libra 120 cryo-TEM from Carl Zeiss NTS GmbH equipped with a LaB6 source. The acceleration voltage was 120 kV and no additional contrast was applied.

Fluorescence correlation spectroscopy (FCS) experiments were performed using a commercial FCS setup (Zeiss, Germany) consisting of a ConfoCor 2 module and an inverted microscope (Axiovert 200) with a Zeiss C-Apochromat® 40×/1.2 W Corr water immersion objective. The fluorophores were excited by an Argon laser ($\lambda = 488\,\mathrm{nm}$) and the emission was collected after filtering with a LP505 long pass filter. For detection, an avalanche photodiode was used. An eight-well polystyrene cover glass (Laboratory-Tek, Nalge Nunc International) was used as a sample cell for the aqueous dispersions of the studied nanoparticles. For each particle sample, a series of ten measurements with a total duration of 5 min was performed. The size of the FCS probing volume was calibrated using a chromophore with known diffusion coefficient, i.e. Alexa Fluor 488 in water.

4. Physical Methods

4.1. Dynamic light scattering

In this section, the basic physical principles of dynamic light scattering (DLS) are explained. The experimental setup used for data acquisition in this thesis and the data evaluation are described.

4.1.1. Principle

The elastic scattering of electromagnetic waves by nanoparticles is described by the Mie theory. [103] Mie exactly solved the Maxwell equations for the scattering of a linearly polarized electromagnetic wave by a spherical object. Each nanoparticle consists of several independent dipoles which act as antennae when hit by an electromagnetic wave, i.e. they isotropically emit electromagnetic waves of the same wavelength as the incident beam. Electromagnetic waves scattered at different dipoles of a nanoparticle interfere in the far field, therefore the scattering intensity depends on the observation angle as depicted in figure 4.1. At a distance which is long compared to the distance of the dipoles, a speckle pattern is observed. In scattering experiments, this angular dependency is described by the scattering vector $\vec{q}$ which is defined as the difference between the wave vectors of the scattered beam $\vec{k}_{sc}$ and the incident beam $\vec{k}_0$,

$$\vec{q} = \vec{k_{sc}} - \vec{k_0}. \tag{4.1}$$

We consider only the quasi-elastic scattering regime, in which the wavelength λ does not change during the scattering process. In this case, the magnitude of the scattering vector is

$$|\vec{q}| = q = \frac{4\pi n \sin\left(\frac{\theta}{2}\right)}{\lambda}. \tag{4.2}$$

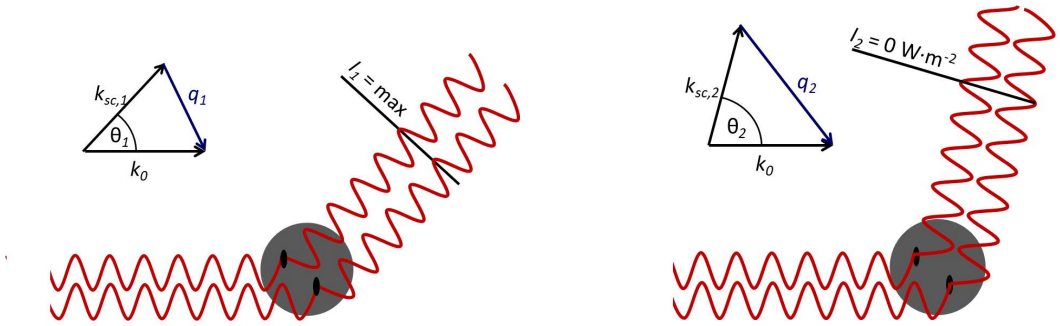

Figure 4.1.: Interference of the light scattered by two different dipoles of a nanoparticle at two different scattering angles. On the left, an example of a scattering angle that allows the observation of constructive interference is shown and on the right example, destructive interference results in a scattering intensity of zero.

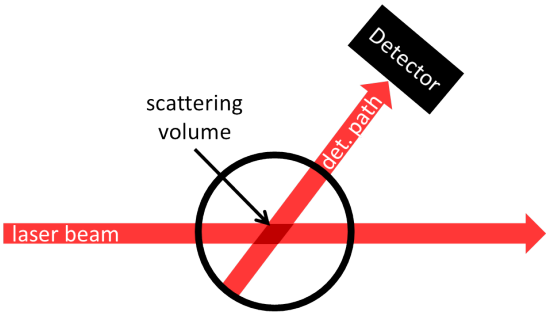

Figure 4.2.: Definition of the scattering volume.

The refractive index n of the dispersant accounts for the correction of the wavelength. q is a measure for the observation length scale, e.g. for a wavelength of $\lambda = 532\,\mathrm{nm}$ and scattering angles θ between 30° and 130°, it is in the range of $1 \times 10^7\,\mathrm{m}^{-1}$.

Nanoparticles in dispersion are not fixed at one point in space, but are undergoing thermally activated Brownian motion. Therefore, the scattering intensities originating from distinct coordinates within the scattering volume are fluctuating with time. The scattering volume is defined by the overlap of the incident laser beam and the detection path which is determined by the optical components between the sample and the detector (figure 4.2). Consequently, the single speckles of the pattern caused by the sample are changing their intensity with time.

While measuring light intensities at different scattering angles is easy to achieve,

the detection of their fluctuations on the micro- to submicrosecond range is more challenging. Single photon counting devices like photomultipliers or avalanche photo diodes have to be used. The signal-to-noise ratio is enhanced by binning of the detected photons in discreet time-intervals. The time-dependent signal is autocorrelated in order to obtain the relaxation time of the fluctuations. Therefore, the intensity $I(q,t)$ measured at a certain angle θ at a certain point on the time scale is multiplied by the intensity detected at a time interval t' later, $I(q,t+t')$. This is done for all possible combinations of t and $t+t'$ and the average is normalized to the averaged intensity detected during the time range which is analyzed. The result is the intensity autocorrelation function (ACF)

$$g_2(t') = \frac{\langle I(q,t)I(q,t+t')\rangle}{\langle I(q,t)\rangle^2}. \tag{4.3}$$

The intensity ACF is obtained in homodyne DLS experiments, in which only quasi-elastically scattered photons are correlated. It is related to the field ACF $g_1(t')$ by the Siegert relation

$$g_1(t') = \sqrt{g_2(t') - 1}. \tag{4.4}$$

The field – also called amplitude – ACF results from DLS experiments when the heterodyne detection mode is used, light which is scattered by the sample is mixed with a fraction of $> 99.9\%$ of uncorrelated, elastic light from the same source. [104]

In the case of a monodisperse, dilute, undisturbed particle sample in which neither particle-particle interactions nor other forces are acting on the particles, only Brownian motion is present. In this case, the amplitude and the intensity ACFs are single exponentially decaying functions in with decay rates Γ which are directly related to the diffusion coefficient D and the magnitude of the scattering vector q:

$$g_1(q,t') = \exp(-\Gamma t') = \exp(-Dq^2t') \tag{4.5a}$$

$$g_2(q,t') = \exp(-2\Gamma t') + 1 = \exp(-2Dq^2t'). \tag{4.5b}$$

Equations 4.5a and 4.5b can be deduced from the Fourier transform of the amplitude ACF, the so called van Hove selfcorrelation function

$$g_{vH}(\vec{r'},t') = \langle n(\vec{r},t)n(\vec{r}+\vec{r'},t+t')\rangle \tag{4.6}$$

in which $n(\vec{r},t)$ is the local number density of particles. g_{vH} equals the probability that a particle is found at $\vec{r}$ at $t=0$ and moves in the time t' to $\vec{r}+\vec{r'}$. Averaged over the whole measurement time, $g_{vH}(\vec{r},t')$ depends only on the mean square displacement of the particle $\langle r'(t')^2\rangle$ which is just the three dimensional expression for the mean square displacement Δx defined for one dimension in equation 2.28,

$$g_{vH}(\vec{r'},t') = \left(\frac{2\pi}{3}\langle\Delta\vec{r'}(t')^2\rangle\right)^{\frac{3}{2}} \exp\left(-\frac{3\vec{r'}(t')^2}{2\langle\Delta\vec{r'}(t')^2\rangle}\right). \tag{4.7}$$

The Fourier transform of equation 4.7 is

$$g_1(q,t') = \exp\left(-q^2\langle\Delta\vec{r'}^2(t')\rangle\frac{t'}{6}\right). \tag{4.8}$$

The relation between the mean square displacement and the self-diffusion coefficient

$$\langle\Delta\vec{r'}(t')^2\rangle = 6Dt' \tag{4.9}$$

connects the van Hove selfcorrelation function (equation 4.7) to the field autocorrelation function (equation 4.5).

4.1.2. Setup

The setup used for the DLS measurements in this thesis is depicted in figure 4.3. The vertically polarized light of a Nd:YAG laser ($\lambda = 532\,\text{nm}$, Verdi 2 W, Coherent Inc.) is focused on the sample in a cylindrical cuvette (# 540-110-80, Hellma GmbH & Co. KG). The detection optics, consisting of polarizer to chose the detection polarization, and a collimator, are mounted on a one-circle goniometer (ALV/SP-125, ALV) with the sample cuvette in the center in order to enable measurements at various scattering angles. The detected light is coupled into a fiber and distributed on two detectors (SPCM-CD2696, Perkin Elmer) by a beam splitter before it is cross-correlated (ALV-6010/160E, ALV GmbH) in order to eliminate afterpulsing signals in the ACF.[1] The autocorrelation functions have been stored and evaluated according to the methods described in the next section.

[1] Afterpulsing signals are observed in measurements with single photon counting devices, e.g. with photomultipliers or avalanche photo diodes. Afterpulsing signals follow directly on a real signal. More details are explained in literature. [105]

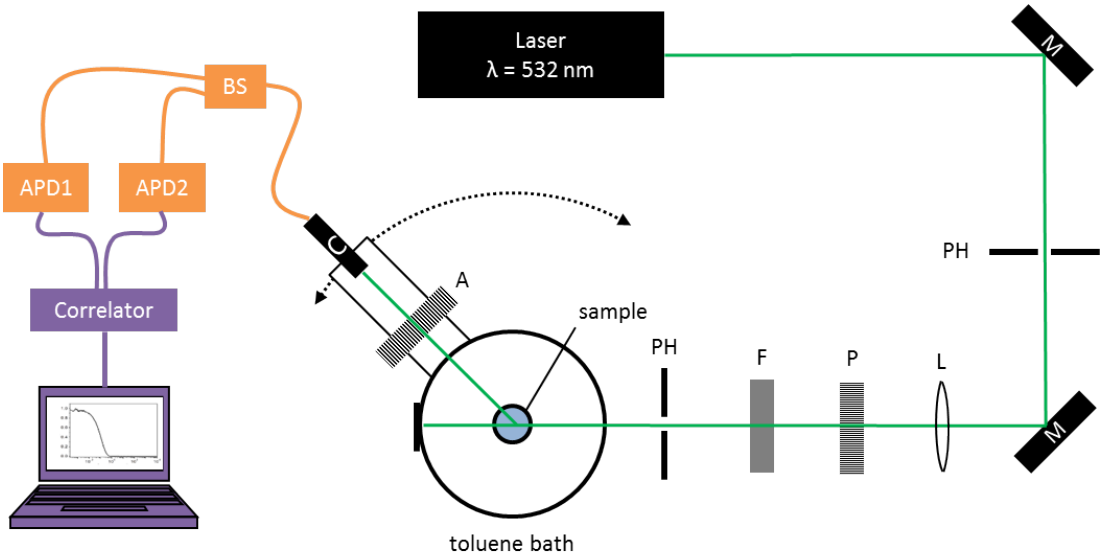

Figure 4.3.: Schematic drawing of the DLS setup. The beampath is represented in black, the fiber optics part in orange, and the computation part in purple. In the beampath, the two mirrors (M) and the two pinholes (PH) serve alignment purposes. The neutral filter (F) is used for adjusting the laser intensity. Only the fraction of light which is vertically polarized in respect to the scattering plane is used for the illumination of the sample. Therefore, a polarizer (P) is placed in the beampath. The sample cuvette is immersed into a toluene bath in order to match its refractive index with the environment for the prevention of reflection. The vertically or horizontally polarized (A) portion of the scattered light is collimated (C) and coupled into an optical fiber. The beam is split and the two fractions of incoming photons are counted independently by two avalanche photo diodes (APD). The signals are cross-correlated by a hardware correlator which is connected to a PC.

4.1.3. Data analysis

There exist several established methods to fit the ACF. In the next paragraphs, the fit with a single exponential, the method of cumulant analysis, [106] the concept of fitting with a Kohlrausch-Williams-Watts (KWW) function, [107,108] and Provencher's CONTIN algorithm [109,110] which have all been used in this thesis will be introduced.

From the derivation shown in the previous section, the fit of the ACF (equation 4.5) with an exponentially decaying function is the most intuitive. The scattering angle θ and the scattering vector q are known, therefore the diffusion coefficient D can be calculated from the relaxation rate Γ. Single exponential fitting does not account for the size and therefore diffusion coefficient distributions in a sample and should only be used for rather monodisperse samples.

If a sample with narrow size distribution ($\frac{\Delta R_H}{\langle R_H \rangle} \ll 0.5\%$) is considered, cumulant analysis conveniently fits the ACF. [106,111] A sum of exponentials is used to fit the ACF

$$g_1(q,t') = \exp\left(-\Gamma_{cum}t'\right)\left(1 + \frac{\kappa_2}{2!}t'^2 + \frac{\kappa_3}{3!}t'^3 + ...\right). \tag{4.10}$$

Γ_{cum} is the average decay rate. The quotient of the second cumulant κ_2 and the square of the average decay rate is the second order polydispersity index

$$\sigma_\Gamma = \sqrt{\frac{\kappa_2}{\Gamma_{cum}^2}}. \tag{4.11}$$

If the broadening arises from a size distribution of the particles in our sample, the size polydispersity can be calculated accordingly by inserting the Stokes-Einstein equation into eq. 4.11. Note that cumulant analysis can only be used if the ACF shows no or only little broadening and has a reasonable signal to noise ratio at short times as only the first part of the ACF is fitted.

In the case of samples with a broader size distribution or distribution of diffusion coefficients, the ACF can be fitted with a stretched exponential or so called Kohlrausch-Williams-Watts function. [107,108,112] The ACF is treated as a distribution of a multitude of single exponential functions with distinct relaxation rates Γ. The function is described by

$$g_1(q,t') = \exp(-\Gamma_{KWW}t')^\beta \tag{4.12}$$

with the decay rate Γ_{KWW} and the stretching factor β ($0 < \beta \leq 1$) accounting for the various diffusion rates. The mean relaxation time $\langle\tau_{KWW}\rangle$ which is the inverse of the mean relaxation rate $\langle\Gamma_{KWW}\rangle$ can be calculated with the mathematical Gamma function $gamma(x)$: [113]

$$\langle\tau_{KWW}\rangle = \frac{1}{\langle\Gamma_{KWW}\rangle} = \int_0^\infty dt' \exp\left(-\left(\Gamma t'\right)^\beta\right) = \frac{1}{\Gamma\beta} gamma\left(\frac{1}{\beta}\right). \tag{4.13}$$

The error of the mean relaxation rate is calculated by

$$\Delta\Gamma_{mean} = \sqrt{\left(\Delta\Gamma \frac{\beta}{gamma\left(\frac{1}{\beta}\right)}\right)^2 + \left(\Delta\beta \frac{\Gamma}{gamma\left(\frac{1}{\beta}\right)}\left[1 - \frac{1}{\beta}\frac{d}{d\beta} gamma\left(\frac{1}{\beta}\right)\right]\right)^2} \tag{4.14}$$

Stretched exponential fits can be used for nearly any type of monomodal ACF - for monodisperse samples, the stretching factor β equals one. However, this stretching factor does not have any physical meaning, i.e. the polydispersity index cannot be calculated from it.

Provencher's CONTIN algorithm is another method to fit an ACF. [109,110] The distribution of single exponentials which sum up to the heterodyne ACF $g_1(t')$ is obtained by a regularized inverse Laplace transform of the ACF. It has the advantage that it directly delivers information about the polydispersity.

Usually, ACFs are measured at several scattering angles θ and fitted separately. The slope of the linear fit of decay rates Γ which are plotted against G^2 equals the diffusion coefficient D of the sample.

In the case of multimodal samples, i.e. if two kinds of particles with fairly different radii are present, the ACF can be fitted with either two single exponentials or two KWW functions.

4.2. Surface plasmon resonance spectroscopy

4.2.1. Priniciple

Plasmons are the eigenmodes of electron density oscillations in the conduction band of metals. They are induced by electromagnetic radiation, e.g. light. Surface plasmons transversally propagate along the interface of a metal and a dielectric, in contrast to bulk and particle plasmons which are the electron density

oscillations within a bulk metal or within the volume of a nanoparticle. Zenneck and Sommerfeld were the first who studied surface plasmons. [114,115] In order to calculate the conditions for the exitation of a surface plasmon with light, the conservation of momentum and energy must be obeyed. The momentum p of an electromagnetic wave is connected to the wave number k by the de Broglie equation,

$$p = \frac{h}{\lambda} = \hbar k. \tag{4.15}$$

h and $\hbar$ are the Planck constant and the reduced Planck constant, respectively. The energy of an electromagnetic wave is

$$E = \hbar\omega \tag{4.16}$$

with the angular frequency ω. In order to express the relation between the energy and the momentum of an electromagnetic wave, the wavelength λ in equation 4.15 is substituted by

$$\lambda = \underbrace{c}_{=\frac{c_0}{\sqrt{\epsilon_i}}} \frac{2\pi}{\omega}. \tag{4.17}$$

The speed of light in the respective medium c can be calculated from the speed of light in vacuum c_0 and the complex refractive index n or the dielectric function of the material, ϵ_i

$$n = \sqrt{\epsilon_i \mu_i} \tag{4.18}$$

$$= \sqrt{\epsilon_i' + i\epsilon_i''} \quad \text{with } \mu \approx 1 \text{ for non-magnetic materials.} \tag{4.19}$$

Note that the dielectric function and therefore the refractive index depends on the frequency ω: $\epsilon_i = f(\omega)$. Using equation 4.17 we can rewrite the de Broglie equation 4.15 as

$$k = \omega \frac{\sqrt{\epsilon_i}}{c_0}. \tag{4.20}$$

Equation 4.20 is called dispersion relation. It is valid for bulk media.

The dispersion relation of surface plasmons can be derived by considering the boundary conditions [116]

$$\frac{k_{z1}}{\epsilon_1} = \frac{k_{z2}}{\epsilon_2}. \tag{4.21}$$

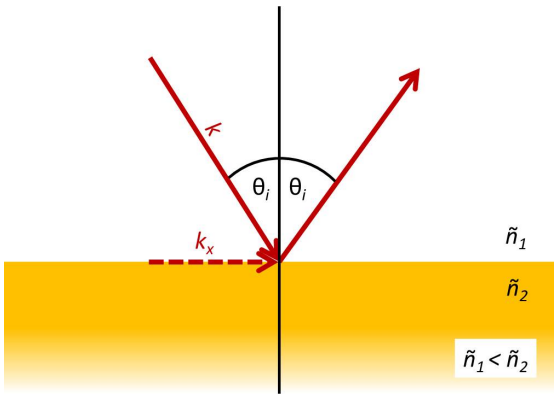

Figure 4.4.: Schematic drawing of the total internal reflection of a photon coming from a medium with the refractive index $\tilde{n}_1$ hitting a medium with the higher refractive index $\tilde{n}_2$. k_x is the x-component of the wave vector.

and

$$k_x^2 + k_{zi}^2 = \epsilon_i \left(\frac{\omega}{c_0}\right) \text{ with } i = 1, 2. \tag{4.22}$$

They describe the special requirements for electromagnetic waves which are propagating along the surface of a metal near a dielectric. By solving both equations 4.21 and 4.22, we obtain the dispersion relation of a surface plasmon

$$k_x = \frac{\omega}{c} \left(\frac{\epsilon_1 \epsilon_2}{\epsilon_1 + \epsilon_2}\right)^{\frac{1}{2}}. \tag{4.23}$$

The surface plasmon can be excited by a laser beam which traverses a dielectric of appropriate refractive index, e.g. a glass prism, and hits the surface of the metal at a certain angle θ_i (figure 4.4). Only the part of the wave parallel to the surface plays a role in surface plasmon excitation (figure 4.4). The dispersion relation for only this part is given by

$$k_x = \omega \frac{\epsilon_i}{c_0} \sin(\theta_i). \tag{4.24}$$

In figure 4.5, dispersion curves of air and gold are shown. As mentioned above, momentum and energy must be conserved during the exitation of a surface plasmon, the dispersion curves must intersect. This is never the case for air and the surface plasmon at the gold-air interface, therefore the surface plasmon needs to be excited by light coming from a dielectric of higher refractive index. In figure

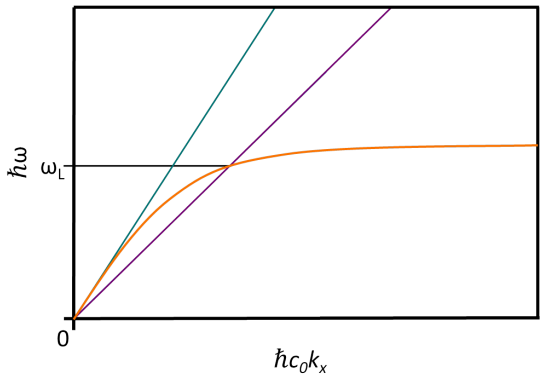

Figure 4.5.: The dispersion curve of the plasmon at the gold-air interface (—) never intersects with the one of air (—), but with the one of N-LAK8 glass (—). By turning the prism, k_x is chosen in a way that the intersection matches the laser frequency ω_L.

4.5, the purple line depicts the dispersion relation for the optical glass N-LAK8[2] which intersects with the one of the surface plasmon. Only one angle θ_i exists at which the dispersion relation of the surface plasmon and N-LAK8 intersect at the frequency of the commonly used HeNe laser. This angle is called angle of surface plasmon resonance, θ_{SPR}.

In practice, the excitation of a surface plasmon can be achieved following two different approaches: The Otto or the Kretschmann setup. In the Otto setup (figure 4.6a), the excitation beam is guided through a prism of highly refractive glass. Between the prism and the gold layer is a narrow air gap, the surface plasmon will be excited at the gold-air-interface facing the prism. The evanescent fraction of the totally reflected excitation beam excites the surface plasmon, limiting the air gap to less than 4000 nm. [117] The Kretschmann configuration (figure 4.6b) is the more convenient approach because it does not require the meticulous alignment of the prism in respect to the gold layer: A thin metal film is deposited directly on the prism. The evanescent wave caused by total internal reflection of the laser beam excites the surface plasmon which is again located at the air-metal interface. This implies that the metal film needs to be sufficiently thin to be penetrated by the evanescent part of the reflected beam. [118] For a N-LAK8 prism, the gold layer thickness is typically 48 nm.

It is important to adjust the incident angle θ_i in order that its moment matches

[2]N-LAK8 is a highly refracting optical glass by Schott AG ($n = 1.71$ at visible wavelenghts).

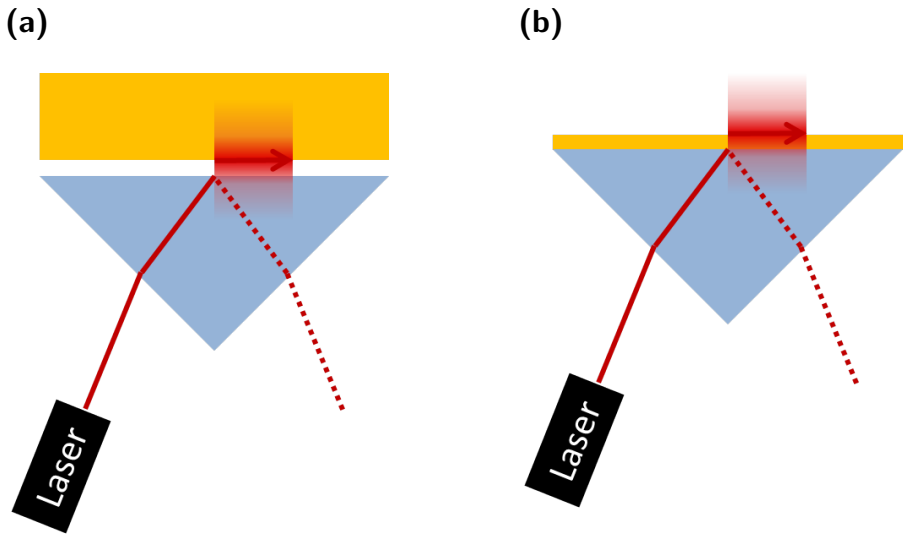

Figure 4.6.: Schematic drawing of the **(a)** Otto and **(b)** Kretschmann configurations for the excitation of surface plasmons. Note that in both cases the surface plasmon is excited by the evanescent wave along the glass-air or glass-metal interface resulting from total internal reflection.

the plasmon dispersion curve at the laser frequency ω_L which usually cannot be as easily changed. The details of the technical realization are described in the next section.

4.2.2. Setup

Surface plasmon resonance (SPR) spectroscopy is a valuable tool in nano- and biotechnology, e.g. for the sensing of nanoscale deposition of polymers or for the measurement of antibody-antigen bindings. [119,120] The sensing application is based on a change of the refractive index of the dielectric near the metal. This leads to a change of the dispersion curve of the plasmon and therefore to another angle of surface plasmon resonance at the given laser frequency (equation 4.20).

The measured parameter in SPR spectroscopy is the reflectivity in relation to the angle. The prism (N-LAK8, Hellma GmbH & Co. KG) with the metal layer (Kretschmann configuration) and with an attached sample cell (figure 4.8, # 136.045-QS version 2, Hellma GmbH & Co. KG) is mounted on one and a photodiode on the other circle of a two-circle goniometer (figure 4.7, 414a-10097, Huber Diffraktionstechnik GmbH & Co. KG). The incident angle θ_i is varied by turning the prism in the laser beam, the photodiode (220D, OSI Optoelec-

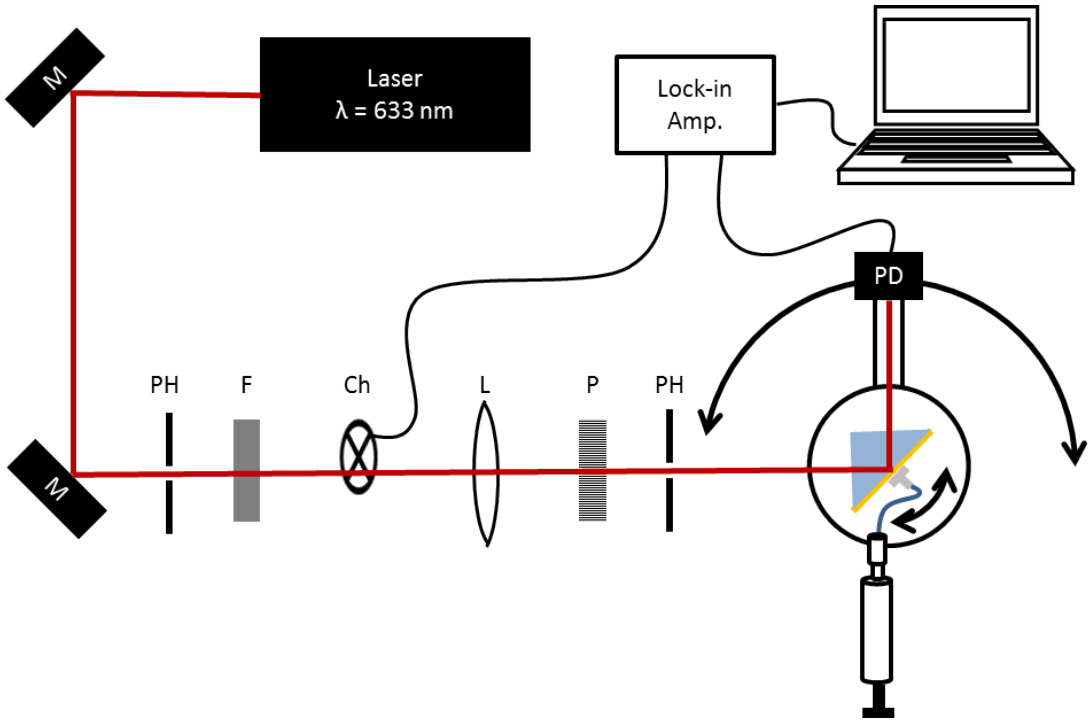

Figure 4.7.: Schematic drawing of the SPR spectroscopy setup. The beam of a HeNe laser ($\lambda = 633$ nm, 1125p, Uniphase Corp.) passes a filter (F) and a chopper (Ch) and is polarized horizontally (P) before it hits the prism. The mirrors (M) and pinholes (PH) are for alignment purposes. The intensity of the reflected beam is measured by a photodiode (PD) in combination with a chopper and a lock-in amplifier and is saved with the according incident angle on a computer.

tronics) is always located at $2\theta_i$. The photodiode is combined with a chopper (197, EG&G) and a lock-in amplifier (5210, EG&G) to increase the signal-to-noise ratio. The surface plasmon can only be excited by 90° polarized light, therefore a polarizer is placed in the beampath. Reflectivity curves which plot the intensity of the reflected light against the angle of incidence on the prism-gold interface are recorded with Wasplas (Version 2.92, Andreas Scheller, MPI for Polymer Research). For the thickness evaluation of deposited layers from a measured reflectivity curve, the program Winspall (Version 3.0, Jürgen Worm, MPI for Polymer Research) has been used.

4.3. Resonance enhanced dynamic light scattering

4.3.1. Principle

The electric field of a surface plasmon propagating along a metal-dielectric interface penetrates to a certain depth into both of those media where its strength decays exponentially. The distance from the metal-dielectric interface at which the intensity – the square of the evanescent part of the electric field of the surface plasmon – has decreased to $E^2 = \frac{E_0^2}{e}$ is the penetration depth $L_\perp$ which can be calculated for a dielectric according to literature by [121]

$$L_{\perp,d} = \frac{c_0}{\omega} \frac{\sqrt{-\epsilon'_m + \epsilon'_d}}{\epsilon'_d}. \tag{4.25}$$

For a surface plasmon propagating along a gold-water interface, the penetration depth into the water phase is $L_{\perp,\mathrm{H_2O}} \approx 200\,\mathrm{nm}$.

The surface plasmon also has a limited propagation length $L_{||}$

$$L_{||} = \left(2\frac{\epsilon''_m}{2(\epsilon'_m)^2} \frac{\omega}{c} \left(\frac{\epsilon'_m \epsilon_d}{\epsilon'_m + \epsilon_d} \right)^{\frac{3}{2}} \right)^{-1} \tag{4.26}$$

which is in the range between 0.6 to 50 µm for gold. [122]

The evanescent part of the surface plasmon which penetrates into the dielectric can be used as incident beam in a DLS experiment. In this configuration, the scattering volume is determined by the penetration depth and not by the lenses and pinholes used in the beam path of regular DLS. In the case of aqueous dispersions, only the colloids in the evanescent field near the gold-water interface

scatter the light, i.e. within a range of 200 nm away from the interface. Consequently, we obtain information about the diffusion properties of the particles closer than this distance to the interface. This enables the investigation of the effect of the surface on diffusion behavior.

In this thesis, nanoparticle diffusion near electrode interfaces is investigated. The details of the experimental setup are described below.

4.3.2. Setup

The setup used for REDLS requires only minor changes of the one used for SPR spectroscopy (figure 4.9). The main difference are the additional units for single photon counting and correlation. The detection angle is changed from 50° to 130° in respect to the gold-sample interface. The time-dependent intensity of the scattered part of the evanescent electromagnetic field near the gold interface caused by the surface plasmon is measured. A special quartz-glass cell with a sample volume thickness of 100 µm is used to pass the light through and minimize multiple scattering from spurious beams from reflections in the cell or prism (figure 4.8). Single photon-counting devices are used as detectors. In this thesis, four hybrid photodetectors (HPM-100-40, Becker & Hickl GmbH) have been used. [123] To our knowledge, this is the first time this detector type is used in a DLS setup. Hybrid photodetectors resemble to photomultiplier tubes: They are vacuum tubes and they enhance the signal of incoming photons. However, in hybrid photodetectors, the primary photoelectron is multiplied by hitting an avalanche diode instead of the dynodes which are found in a photomultiplier. Even if the gain of hybrid photodetectors is lower than the gain of photomultiplier tubes, [124] they have some advantages which play a role in DLS: First, they do not show afterpulsing. [125] Usually this effect is avoided by the costly manner of by splitting and cross-correlation of the signal which requires two detectors. Second, they have a high quantum efficiency.

In this work, four of those detectors have been used in parallel, each connected by an optical fiber (single mode fiber, $\lambda = 630$ nm, PMC-630-4-455, Schäfter + Kirchhoff GmbH) to a collimator (focusable, 60FC-K-4-M12-33, Schäfter+Kirchhoff GmbH). The collimators are mounted with a holder which enables three dimensional alignment (KineMATIX-P2, Qioptiq Photonics Ltd.) onto the goniometer plate. Glan-Thompson polarization prisms (10^{-5} extinction ratio, Bernhard Halle Nachfl. GmbH) in front of the collimators ensure that only horizontally

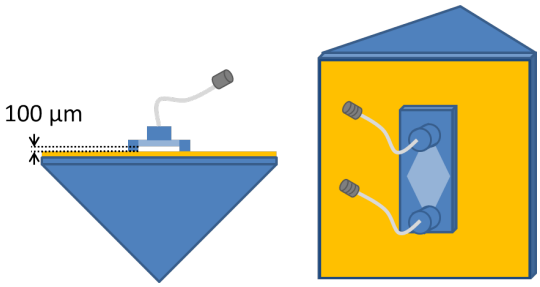

Figure 4.8.: The cell is fixed directly at the gold layer which creates a metal-glass sealing as shown in the schematic drawing.

polarized light, i.e. with the same polarization as the surface plasmon, is coupled into the fibers. The detectors are located at a defined angle of 20° to each other. This multi-angle REDLS setup enables the measurement at four different angles at the same time. This is especially interesting for samples that age or deposit during time because all angles have been measured at the same state of the system. In addition, it speeds up the measurement time by four. The detectors are connected to a hardware correlator with four input channels (DPC-230, Becker & Hickl GmbH) which assigns time-tags to the incoming signals and correlates them using a multi-τ algorithm.

To perform REDLS measurements near an electrode, a sample cell which enables the application of electric fields has been developed. In this sample cell, one electrode is the gold film which is also used for the generation of the surface plasmon. This is the electrode at which be observe the nanoparticle behavior. A 300 nm indium tin oxide (ITO) layer which has been sputtered (Auto 500, Edwards) on the inner side of a standard flow through cell (# 136.045-QS version 2, Hellma GmbH & Co. KG) serves as the counter electrode. An insulating tape (tesa® 51408 Kapton®, 65 µm thickness, Tesa SE) is used for insulation of the ITO electrode against the gold electrode at the sealing part of the sample cell (figures 4.10a and 4.10b). By connecting the gold electrode and the ITO electrode to the output of a function generator (Function generator 8021, Tabor Electronics), electrical potentials can be applied to the sample with the field perpendicular to the gold electrode (figure 4.10c). The large electrode area in combination with the small distance between the electrodes guaranties a homogeneous field and allows the application of comparatively high field strengths even at low voltages.

Before any REDLS measurement, the angle of surface plasmon resonance of

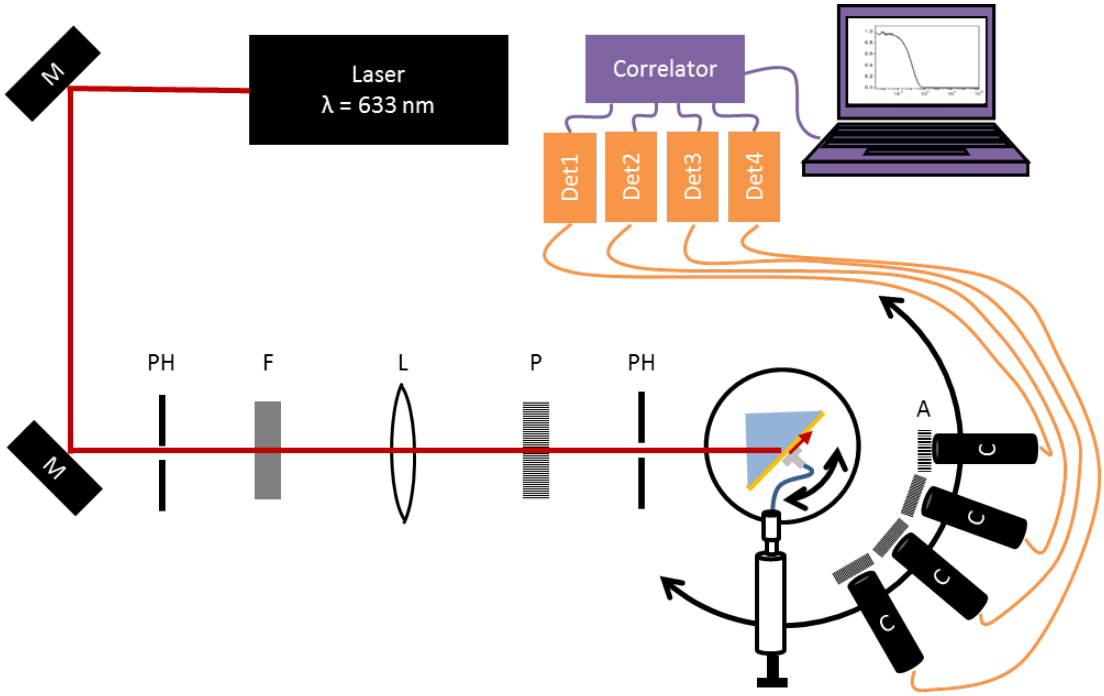

Figure 4.9.: Schematic drawing of the REDLS setup. It is in most parts equivalent to the SPR setup (figure 4.7). Either the – in respect to the scattering plane – horizontally or vertically polarized fraction of the scattered light are detected by adjusting the polarizers (A) accordingly. The light is coupled into fibers by collimators (C), and guided to single-photon counting detectors (Det) which are connected to a correlator. Note that the detectors used do not show correlated afterpulsing. Therefore all four detectors are located at different angles.

.

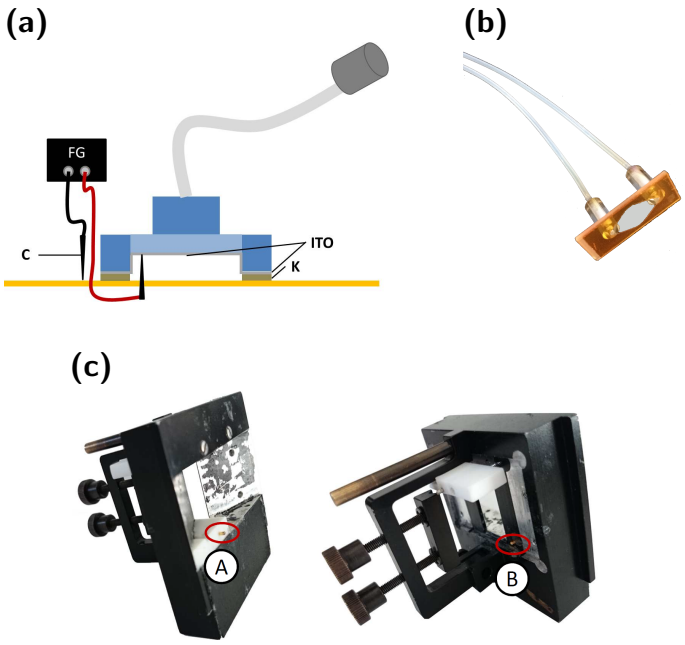

Figure 4.10.: **(a)** Schematic drawing of the cross-section of the sample cell for measurements in the electric field. (ITO) is the sputtered conductive indium tin oxide electrode, (K) is the Kapton tape for insulation against the gold electrode and (C) are the electrical contacts which are connected to a function generator (FG). **(b)** Photograph of the sample cell with a sputtered layer of ITO and Kapton® for insulation. **(c)** Photographs of the holder for the sample cell and prism including the extension for measurements in the electric field: (A) and (B) are the electric spring contacts.

the respective sample was detected. The ACFs shown in this thesis are averages over several consecutive runs during which individual ACFs have been obtained. By this procedure it is possible to exclude experimental runs hampered by strong signals from dust particles or gas bubbles.

4.3.3. Data analysis

The functions used for fitting REDLS ACFs are equivalent to those for the evaluation of DLS (section 4.1.3). However, some care should be taken when calculating the scattering vector because the use of a triangular prism does not allow a "perfect" alignment in which the the gold surface is located in the turning center of the goniometers and at the center of the surface plane at the same time. REDLS measurements are only possible in the latter case, therefore the scattering angle

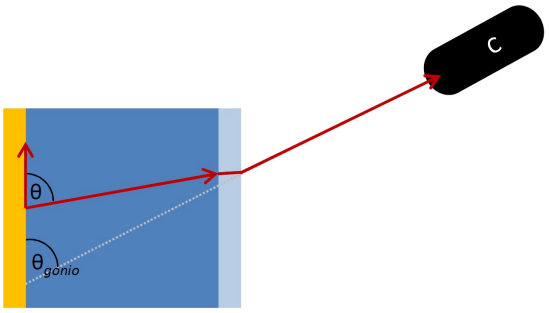

Figure 4.11.: Shift of angle due to the difference of the refractive indices of the sample and air.

has a systematic error. However, due to long distance between the collimator and the gold layer in comparison to the shift of the layer out of the turning center, this limits to ±1°. However, there is another systematic error by the shift of the beam due to refraction when it is passing from the sample through the quartz glass of the sample cell into air (see figure 4.11) which needs to be corrected by calculating the actual scattering angle using the equation

$$\theta = \theta_{gonio} \arcsin\left(\frac{n_{sample}}{n_{air}}\right) \tag{4.27}$$

with the goniometer position θ_{gonio} and the refractive indices n of the respective sample and air.

In addition, all errors in regular DLS have also been considered, e.g. temperature fluctuations when diffusions coefficients are derived from the relaxation rate Γ. The temperature-induced fluctuation of viscosity is the most crucial parameter here. Assuming a temperature during the measurement of $T = (294 \pm 1)K$, the dynamic viscosity of water fluctuates around $\eta = (0.981 \pm 0.029)\,\mathrm{mPa\,s}$. As the diffusion coefficient D depends linearly on the viscosity, its relative error equals the relative error of viscosity,

$$\Delta_{rel}\Gamma = \Delta_{rel}\eta = 3.0\%. \tag{4.28}$$

4.4. Cyclic voltammetry

Cyclic voltammetry is a method to detect and characterize electrochemical reactions of a given sample at electrodes. Two electrodes and a reference electrode are immersed into the sample. A triangular voltage is applied between the working and the counter electrode (FG). The current is measured and automatically plotted against the voltage at the working electrode by a potentiostat (PGSTAT302, Autolab). Electrochemical reactions appear as peaks in this cyclic voltammogram trace. One reaction, i.e. oxidation or reduction, can result in more than one peak when it involves several steps like adsorption at the electrode before reduction.

In this thesis, cyclic voltammetry has only been used to verify that not electrochemical reactions are occurring in the investigated voltage range. However, the method can also be used to determine the standard potentials of electrochemical reactions.

4.5. Experimental details

For the deposition of gold layers necessary for the excitation of the surface plasmons on 25 mm × 25 mm N-LAK8 glass substrates (Hellma Analytics). They have been immersed in a 2% solution of Hellmanex (Hellma Analytics) in MilliQ-H_2O and irradiated with ultrasound for 15 min. Afterwards they were thoroughly rinsed with running MilliQ-H_2O and washed with ethanol before they have been dried in a nitrogen stream. 1 nm of chromium has been vapor deposited on the slides to ensure adhesion of the gold layer which has been evaporated directly afterwards (Edwards Auto 306, evaporation rate 0.2 nm/s, final thickness 48 nm). The substrates have then been glued to a N-LAK8 prism with an index matching oil (Cargille-Sacher Laboratories Inc.). A new gold layer has been used for every series of REDLS experiments.

If a negatively charged gold surface was desired to prevent adsorption of the nanoparticles, the gold layer was immersed in a 1 mM solution of 11-mercaptoundecanoic acid (95%, Sigma-Aldrich GmbH) in ethanol for at least 24 h. The gold layer was washed with ethanol afterwards and dried in a nitrogen stream.

The particle samples have been injected with a syringe through a filter (pore size 0.45 µm, Millex HA, Merck Millipore) into the sample cell.

5. Results and discussion

5.1. Functionalized nanoparticles for biomedical applications

Poly(lactic acid) (PLA)-based nanoparticles with enhanced stability in environments of high ionic strengths as well as with fluorescent labeling were prepared. The goal was to obtain nanoparticles with covalently and therefore stably bound carboxyl- and fluorescent functionalization.

Two different routes were established to prepare polymer nanoparticles with the desired properties (figure 5.1). First, an oligo(lactic acid)-based (OLA-based) macromolecule with polymerizable double bond was synthesized from lactide and hydroxyethyl methacrylate (HEMA) in bulk and solution polymerizations. Three macromolecules with different molecular weights have been obtained and the most suitable one, i.e. the one with the highest molecular weight, was used for the copolymerization step with acrylic and methacrylic acid (AA and MAA) in different ratios. Additionally, the HEMA-OLA macromolecule was copolymerized with a fluorescent dye.

The (HEMA-OLA)-MAA copolymer with the most promising properties in terms of molecular weight as well as number of acid units in the chain and the fluorescently labeled macromonomer were chosen for the preparation of nanoparticles in a miniemulsion solvent evaporation process. Following another route, HEMA-OLA and methacrylic acid were used as comonomers in the miniemulsion solvent evaporation process. In order to evaluate the nanoparticle properties, control particles without any functionalization were prepared from HEMA-OLA without the addition of a comonomer.

The details of the single preparation steps and comparison of the different products obtained from each stage are discussed in the following sections.

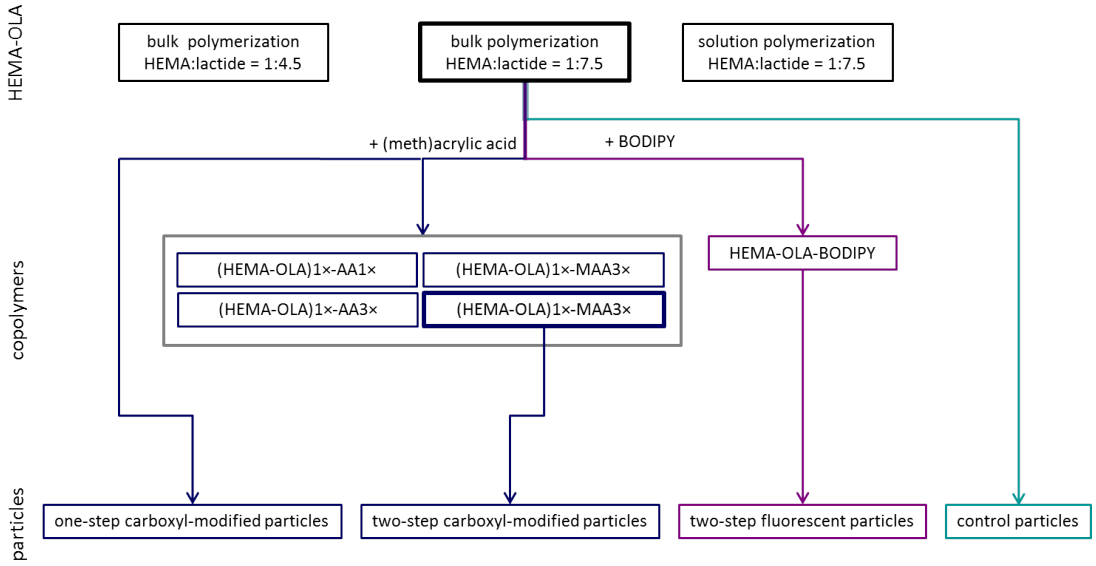

Figure 5.1.: Routes to the functionalized particles described in this chapter. The most suitable intermediate products used in the following step are marked by the bold frames. The ratios given are molar ratios.

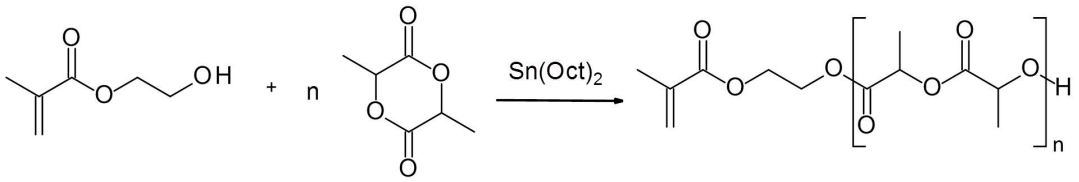

Figure 5.2.: Reaction equation of the ring-opening polymerization of lactide in the presence of HEMA and the catalyst tin(II) 2-ethylhexanoate.

5.1.1. HEMA-OLA with polymerizable double bond

An OLA with polymerizable double bond was synthesized by a tin(II)-catalyzed ring opening polymerization of lactide. As described in section 3.1.2, this reaction is cocatalyzed by alcohols. The alcohol is the unit of the resulting polymer and is linked to it by an ester bond. A copolymerizable vinyl group in the OLA chain can be obtained by using an unsaturated alcohol like hydroxyethyl methacrylate (HEMA) as cocatalyst (figure 5.2). The reaction was carried out in bulk following a previously published procedure [102] and in solution in adaption to a similar synthesis. [126] The obtained HEMA-OLA macromolecules were characterized by ^{1}H NMR and GPC. Depending on the feed ratio of HEMA and lactide, HEMA-

Table 5.1.: GPC and ^{1}H NMR data of the three different HEMA-OLAs synthesized in bulk (B1, B2) and in solution (S1). The repeat unit refers to the one in figure 5.2. Reprinted with permission. [127]

		GPC			^{1}H NMR	
Sample	$n_{Lactide}$:n_{HEMA}	M_n	M_w	D	M_n	**repeat units**
B1	9:1	1731	2779	1.61	1714	11
B2	15:1	2598	3498	1.35	2290	15
S1	15:1	1361	2743	2.02	1858	12

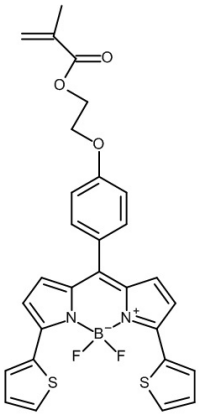

Figure 5.3.: Chemical structure of the BODIPY dye B612-MA.

OLAs with different molecular weights have been obtained because a different number of propagation reactions took place at the same time (table 5.1). The product of the solution polymerization (S1) had a broader size distribution than the rather monodisperse products from the bulk polymerization (B1 and B2). This is not typical because the products of solution polymerizations are usually less polydisperse due the constant viscosity and the better heat transfer in diluted reaction mixtures. The GPC and ^{1}H NMR results for the bulk oligomers were well in accordance with previously published ones (figure 5.6). [102]

For the preparation of nanoparticles, polymers of high molecular weight are favored as their higher entanglement prevents diffusion of the polymer out of the particle during the formulation process. Thus, the heavier of the HEMA-OLAs prepared in bulk polymerization, namely sample B2, was used for the copolymerization step with (meth)acrylic acid and a fluorescent dye.

5.1.2. Synthesis of functionalized HEMA-OLA

For the synthesis of carboxyl-functionalized and fluorescently labeled OLA-based copolymers, the HEMA-OLA sample B2 was copolymerized with acrylic and methacrylic acid as well as with a fluorescent, copolymerizable dye from the BODIPY family, B612-MA (figure 5.3). The HEMA-OLA and acrylic acids or methacrylic acid have each been used in a 1:1 and a 1:3 molar ratio (figure 5.4). The molar mass of the macromolecules increased approximately by a factor of two during the copolymerization (table 5.2). The amount of the acid units in the copolymer was determined by potentiometric titration. As expected, the copolymers prepared with the higher molar ratio of acid monomer to HEMA-OLA contain more acid units. The difference is more significant for the methacrylic acid copolymer than for the acrylic acid one. All copolymers contain more acid units than it would have been expected from the feeding ratio. This might be due to the partial hydrolysis of the ester bonds of the HEMA-OLA fraction of the copolymer chain. The resulting carboxyl groups also contribute to the total number of acid units.

The copolymers were also characterized by ^{1}H NMR. The signals of the acrylic and methacrylic acid units could not be resolved by ^{1}H NMR because they are located at δ = 1.14 to 1.32 ppm and δ = 1.54 to 2.16 ppm and therefore overlap with the peaks caused by the OLA-chains in this range (figure 5.7). [128] The relative number of HEMA-OLA vinyl groups is decreasing as determined by comparison of the integrals of peaks a and b from the vinyl group against the one of peak c from the chain. According to the conversion that is 22% in the case of (HEMA-OLA)1×-MAA3×, not all vinyl groups reacted during the polymerization. This might be due to the low polymerization rate of the HEMA-OLA due to the sterical demands of the oligomer. Low reaction rates of the HEMA-OLA mean that competitive radical-catching reactions, e.g. with the solvent or impurities, are gaining importance. Experiments on the copolymerization kinetics of methyl methacrylate and a HEMA-caprolactame which is structurally very similar to HEMA-OLA have proven that the copolymerization is nearly ideal. [129] The Q-e scheme in figure 5.5 shows that the values of acrylic acid and methacrylic acid are even closer to those of HEMA than those of methyl methacrylate. Thus, homopolymerization can be excluded in our case.

A fluorescently labeled polymer was synthesized by copolymerization of HEMA-OLA B2 and a fluoroescent dye of the BODIPY family. This dye was chosen

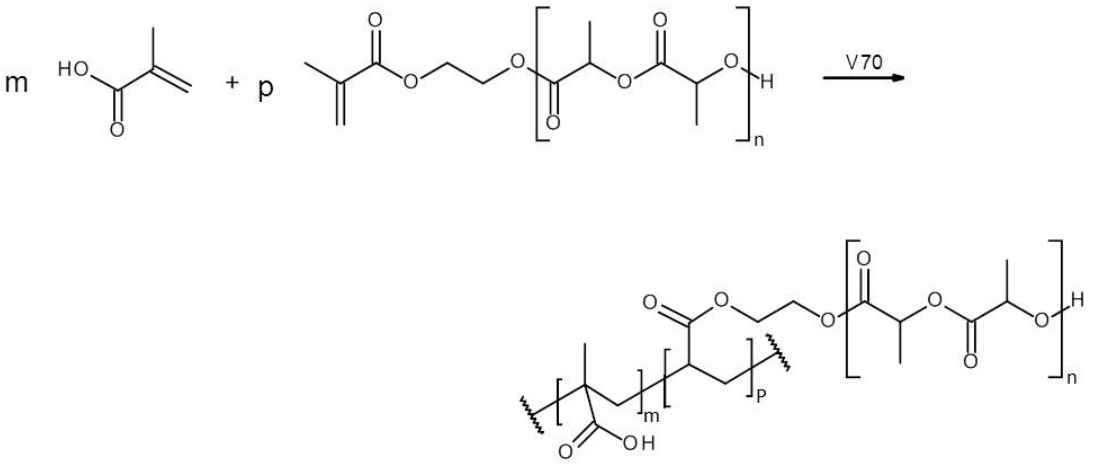

Figure 5.4.: Reaction equation of the copolymerization of HEMA-OLA with methacrylic acid as an example. Adapted with permission. [127]

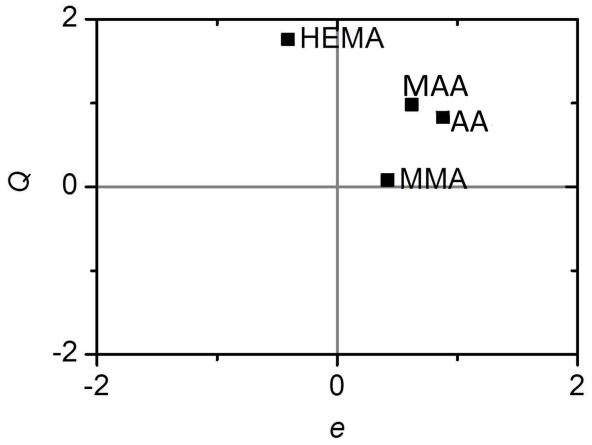

Figure 5.5.: *Q-e* scheme of the relevant monomers. Values are taken from literature. [130,131]

Table 5.2.: Results from GPC and potentiometric titration of the (meth)acrylic acid and dye copolymers. Adapted with permission. [127]

Sample	M_N (g/mol)	M_W (g/mol)	PDI	Acid units (wt%)
(HEMA-OLA)1×-AA1×	3535	5678	1.61	27.3
(HEMA-OLA)1×-AA3×	3709	4197	1.13	29.1
(HEMA-OLA)1×-MAA1×	3290	4229	1.29	14.8
(HEMA-OLA)1×-MAA3×	3209	3920	1.22	22.6
(HEMA-OLA)-(B612-MA)	4154	7053	1.91	-

because of its high quantum yield and excellent solubility in toluene. [132] Like the acidic copolymers, the product was characterized by GPC and ^{1}H NMR. The GPC results reveal the success of the polymerization (table 5.2) as does the decrease of the integrals caused by vinyl protons in the ^{1}H NMR spectrum (figure 5.8). The dye units in the copolymer cannot be resolved by ^{1}H NMR because their concentration is below the resolution of the method.

The conversion of the copolymerization of HEMA-OLA and B612-MA is 34%, but experiments on the reaction kinetics have shown that the conversion of the radical homopolymerization of HEMA-OLA or its copolymerization with the BODIPY dye could be increased by further addition of initiator (figure 5.9).

For the preparation of nanoparticles, only the (HEMA-OLA)1×-MAA3× copolymer was used due to its high number of acid units. The (HEMA-OLA)1×-AA1× and (HEMA-OLA)1×-AA× carry even more acid units but are better soluble in water. Thus, their chance of escaping from the chloroform droplets or from the particles during the miniemulsion solvent evaporation step is higher. This would lead to an unsolicited loss of functional groups in the particle.

5.1.3. Nanoparticle formulation

Two different types of PLA-based nanoparticles were prepared in a miniemulsion solvent evaporation procedure: Nanoparticles with additional carboxyl groups on their surface and nanoparticles with fluorescent labeling. Two different procedures were applied (figure 5.10): In the first procedure, the one-step approach, the copolymerisation step and the particle formation step by miniemulsion solvent evaporation were carried out simultaneously. Methacrylic acid, HEMA-OLA

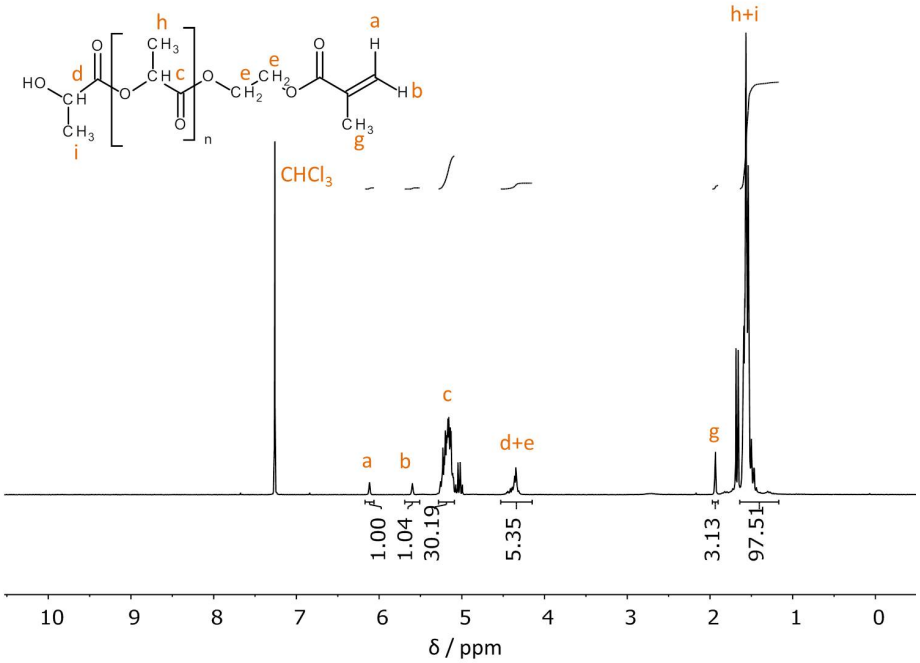

Figure 5.6.: ^{1}H NMR of HEMA-OLA sample B2 in chloroform. Reprinted with permission. [127]

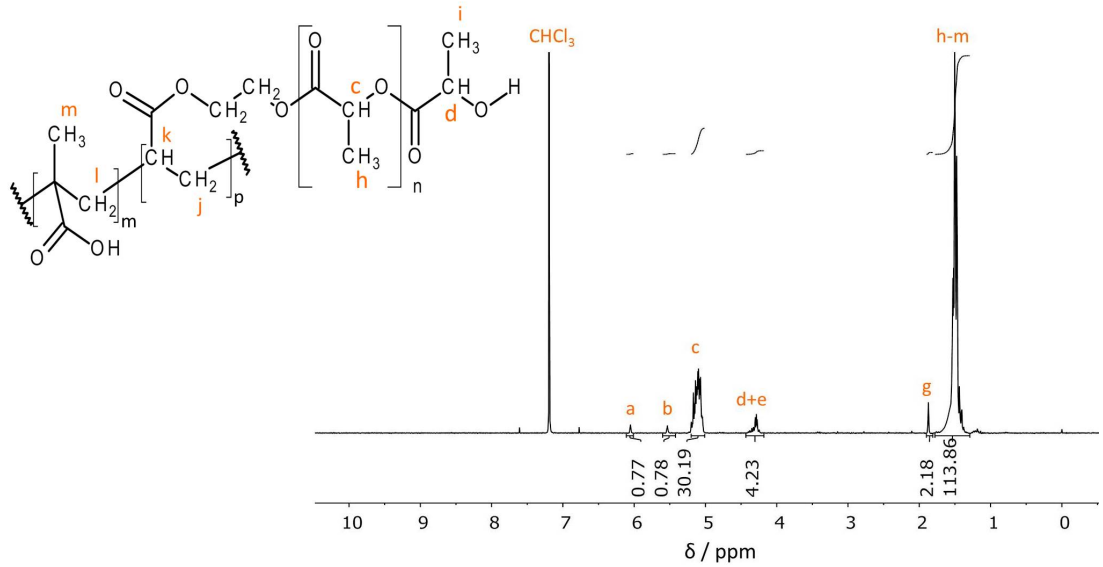

Figure 5.7.: ^{1}H NMR of (HEMA-OLA)1×-(MAA)3× in chloroform.

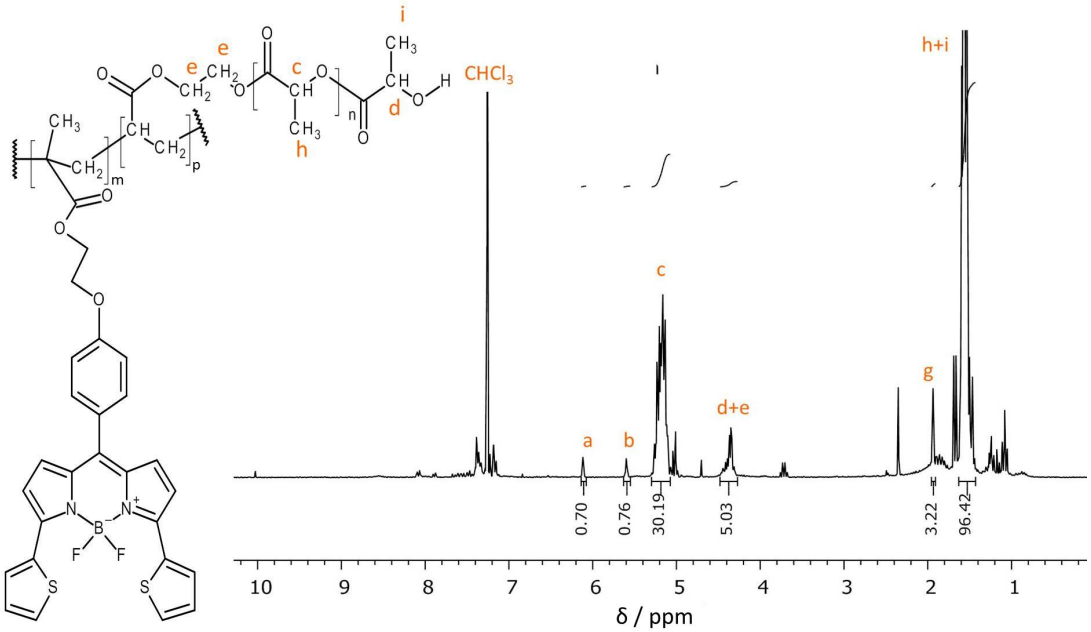

Figure 5.8.: ^{1}H NMR of (HEMA-OLA)-(B612-MA) in chloroform.

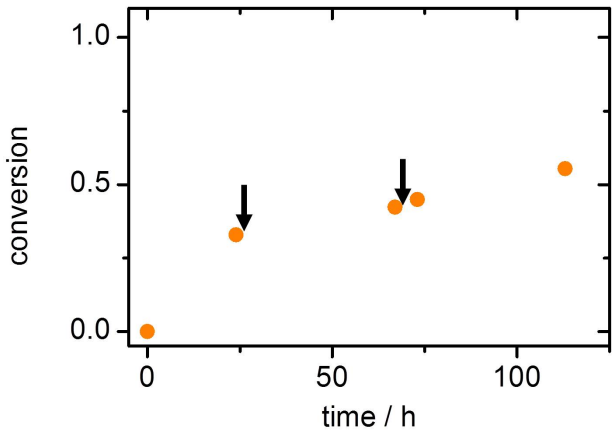

Figure 5.9.: Conversion of the copolymerization of HEMA-OLA and B612-MA. The arrows indicate further addition of initiator.

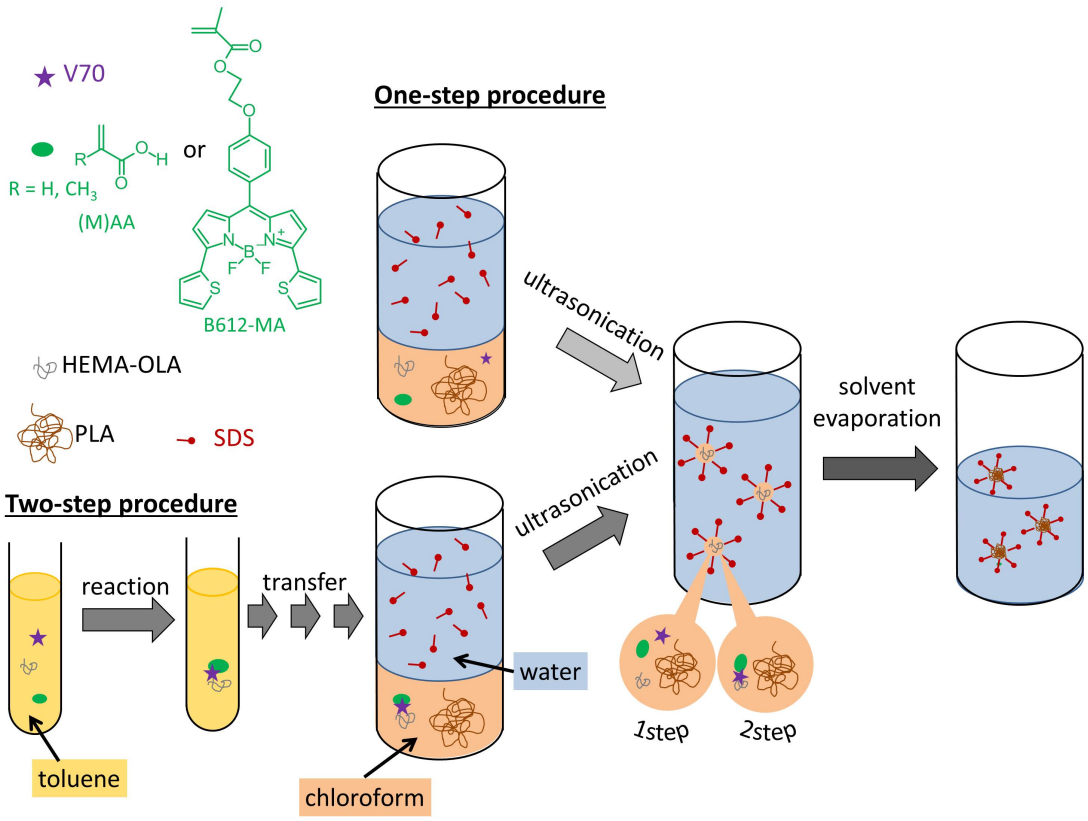

Figure 5.10.: Schematic drawing of the two procedures to prepare the nanoparticles. Adapted with permission. [127]

B2, the oil-soluble azo initiator V70, and preformed PLA are together dissolved in chloroform. The solution was dispersed in an aqueous solution of sodium dodecyl sulfate (SDS). HEMA-OLA and the methacrylic acid are copolymerizing while the chloroform is evaporated. In the second, the two-step procedure, the copolymer was prepared in a separate step as described in section 5.1.2 and used together with PLA in the miniemulsion solvent evaporation procedure.

Both approaches have their advantage and disadvantage: The one-step procedure is less time-consuming because the copolymer does not need to be isolated and purified. Additionally, the concentration of the reaction mixture increases during the copolymerization and thus its speed. The drawback is that the solvents used in the miniemulsion solvent evaporation procedure must have a low boiling point. THF and chloroform, which meet this requirement, are not ideal solvents for radical polymerizations due to their high transfer rate. Another disadvantage is that methacrylic acid dissolves to a certain amount in water, therefore it might

Table 5.3.: Hydrodynamic radius R_H, polydispersity index PDI, ζ-potential, area density of carboxyl groups ρ_{COOH}, and number of carboxyl groups per particle N_{COOH} of the prepared PLA nanoparticles. Adapted with permission. [127]

Sample	R_H (nm)	PDI	ζ-pot. (mV)	ρ_{COOH} (μmol m^{-2})	N_{COOH} (per particle)
PLLA/HEMA-OLA	46	0.10	-38	0.179	3.15×10^3
PLLA/(HEMA-OLA)-MAA-1step	43	0.11	-51	0.488	6.83×10^3
PLLA/(HEMA-OLA)-MAA-2step	43	0.10	-48	0.491	6.88×10^3
PLLA/(HEMA-OLA)-(B612-MA)	46	0.07	-41	0.115	2.09×10^3

migrate from the oil to the water phase during the reaction. Toluene has a by four times lower transfer constant and is used as solvent for the copolymerization in the two-step procedure. The copolymer is isolated and purified before it is used in the miniemulsion and solvent evaporation step, therefore only covalently bound carboxyl units are present in the nanoparticle.

The size of the particles, i.e. their hydrodynamic radius R_H, was measured by DLS. ζ-potential measurements and surface charge titrations (table 5.3) were performed in order to characterize their surface charge properties. The particle radii and PDI are in the range of 45 nm and 0.1 for all particles. This meets the expectations because they depend only on the amount of surfactant as well as the ultrasound amplitude and duration during the emulsification step which have been identical in all particle preparations. A TEM image of the particles prepared in the two-step procedure is shown in figure 5.11[1], the size distribution as determined by CONTIN analysis of DLS data in figure 5.12. The ζ-potentials and carboxyl group densities of the particles are higher for both procedures than for control particles which have been synthesized without methacrylic acid.

The high number of carboxyl groups on the particle surface also increases their stability under salty conditions. This was verified by DLS experiments. Samples of dialysed particle dispersions in NaCl solutions of concentrations between 0 and 100 mM as well as in phosphate buffered saline (PBS, 0.138 mol/L NaCl, 0.0027 mol/L KCl, pH 7.4 at 25 °C) have been prepared and analyzed by DLS. The representative ACFs in figure 5.13 show that the control particles can withstand only the pure water and 1 mM NaCl solutions. They agglomerate in salt

[1] Cryo-TEM imaging courtesy of (*Name aus Datenschutzgründen online nicht verfügbar*).

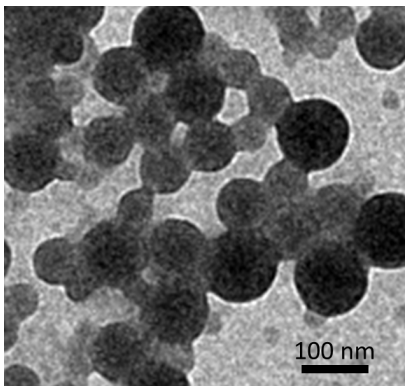

Figure 5.11.: Cryo-TEM image of the PLLA/(HEMA-OLA)-MAA-2step particles.

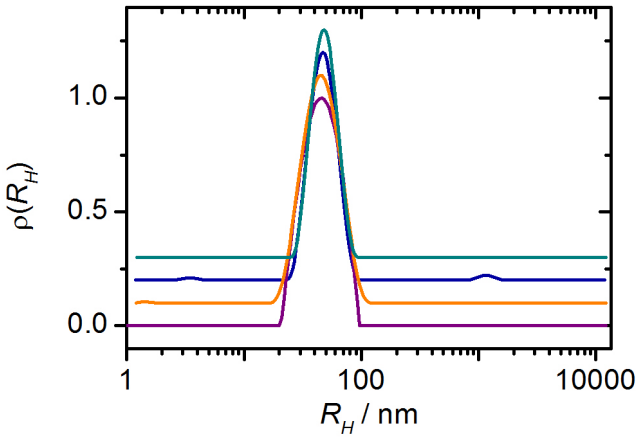

Figure 5.12.: CONTIN fits of DLS. The purple line refers to the control sample, the orange and blue lines to the carboxyl-functionalized particles prepared in the one-step respectively two-step procedure, and the green line to the fluorescently labeled particles.

solutions of 5 mM and higher concentrations. The carboxyl-modified nanoparticles are more stable, the ones prepared in the one-step procedure agglomerate only at 10 mM and higher salt concentrations, the ones prepared in the two-step procedure only at 100 mM and in PBS that is used to check the particle properties under physiological conditions.

Following the two-step procedure, also fluorescently labeled nanoparticles have been prepared. They have the same size and surface charge characteristics as the control particles (table 5.3). The absorption spectrum shows that the most distinct absorption maximum of the fluorescent copolymer and the nanoparticles is at $\lambda = 509$ nm (figure 5.14). Two secondary maxima at 470 nm and 530 nm are found in the spectrum of the copolymer, but are not resolved in the one of the nanoparticles. The absorption of BODIPY dyes is very sensitive to the chemical composition of the surroundings of the molecule, therefore the absorption curve of the labeled nanoparticles in water differs from the one of the (HEMA-OLA)-(B612-MA) in chloroform. [133,134] The successful labeling of the particle was checked by FCS. The hydrodynamic radius determined by sigmoidal fitting of FCS ACFs according to equation 3.16 was the same as the one obtained from cumulant fits of DLS data which proves the successful labeling. No fast process was present in the ACF which would indicate the presence of free, unbound dye molecules.

In order to check the stability of the labeling, the same sample was remeasured by FCS ten days later. This ACF was equivalent with the previously measured one, thus it can be concluded that the dye is stably bound and will not be released even in long-term imaging experiments, e.g. studies of the cellular nanoparticle uptake.

Overall, the experiments show that HEMA-OLAs are a good starting point for the synthesis of functionalized PLA-based nanoparticles. The copolymer can be synthesized in situ during the miniemulsion solvent evaporation procedure. The properties of nanoparticles formulated following this one-step procedure differ only slightly from those of the particles prepared by the two-step procedure in which a separately prepared copolymer is used.

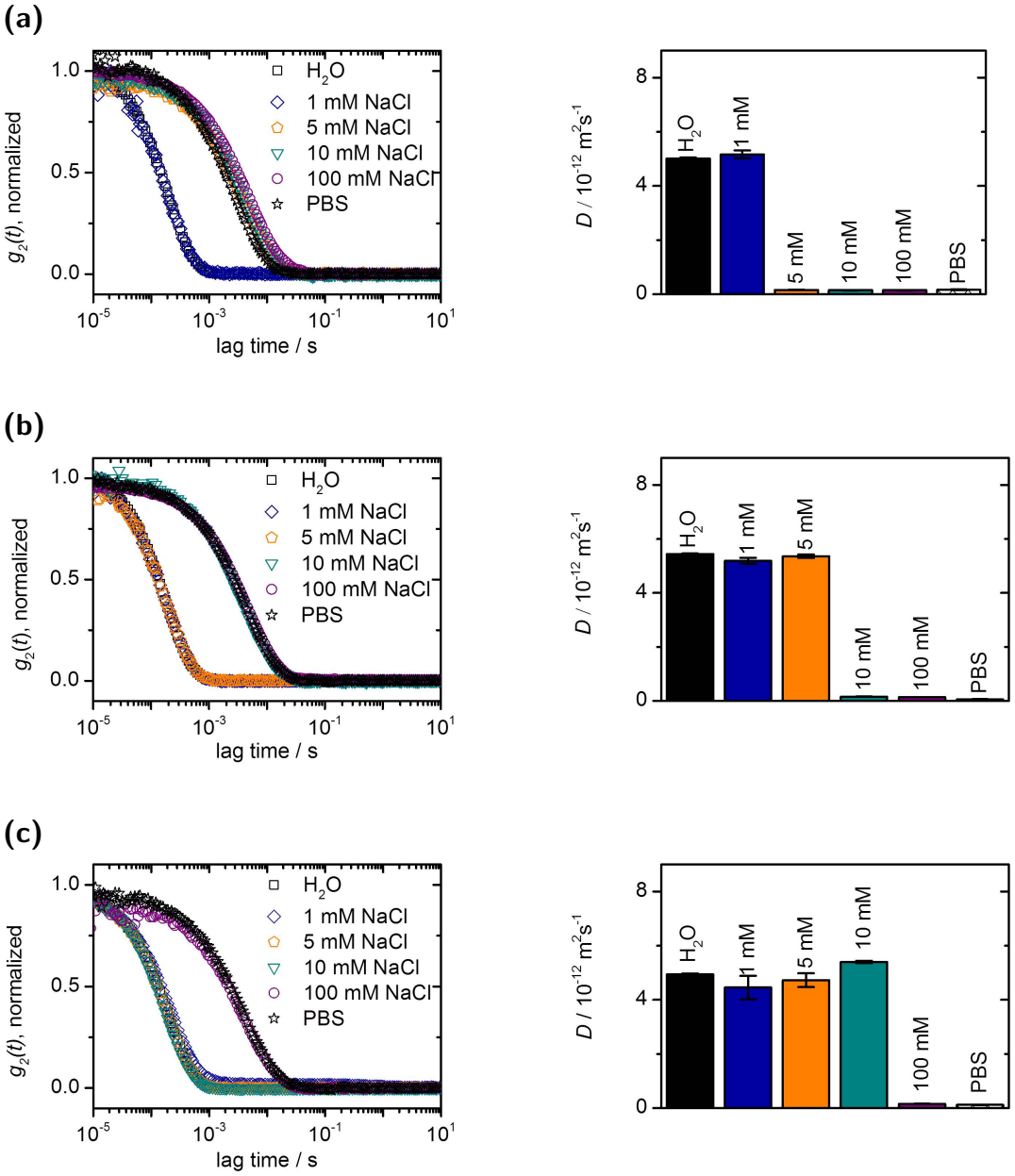

Figure 5.13.: Stability of the carboxyl-functionalized nanoparticles as measured by DLS. Row **(a)** refers to the control nanoparticles, row **(b)** to the nanoparticles prepared by the one-step procedure, and row **(c)** to the ones prepared by the two-step procedure. The left column shows the ACFs at $q = 1.2 \times 10^7\,\mathrm{m}^{-1}$ of the respective samples, the right column contains the diffusion coefficients determined from KWW fits of the ACFs. Reprinted with permission. [127]

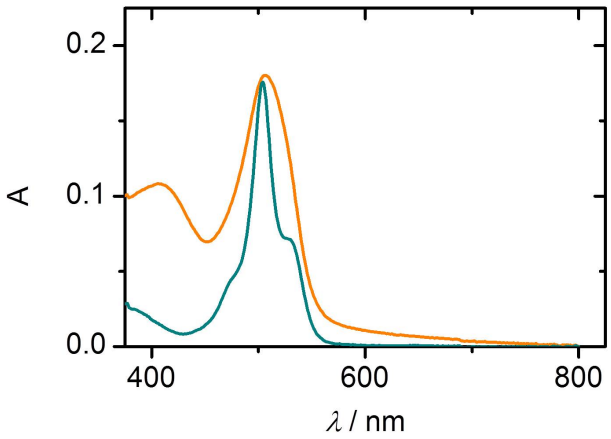

Figure 5.14.: Absorption curves of the (HEMA-OLA)-(B612-MA) copolymer in chloroform (green) and the PLLA/(HEMA-OLA)-(B612-MA) nanoparticles in water (orange).

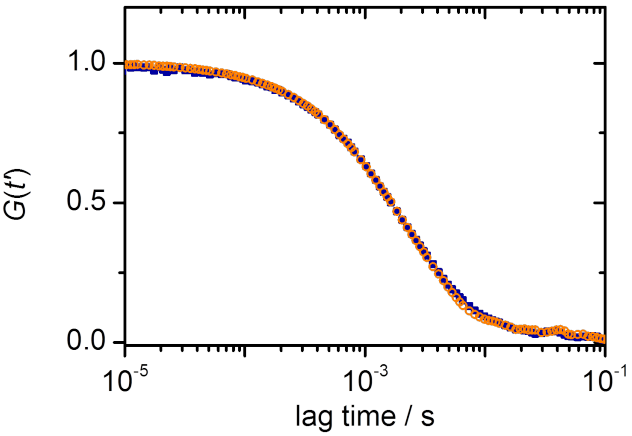

Figure 5.15.: Normalized autocorrelation curves from the FCS measurements of a dilute dispersion of the PLLA/(HEMA-OLA)-(B612-MA) nanoparticles one day (blue squares ■) and eleven days (orange circles ○) after preparation. Adapted with permission. [127]

5.2. Nanoparticle dynamics near an electrode

5.2.1. Studied sample

The dynamics of polystyrene nanoparticles near a gold electrode has been investigated using REDLS with the setup described in section 4.3.2.

Instead of the particles which have been prepared according to the previous section, polystyrene particle size standards have been used in the following experiments due to their near-monodisperse size distribution. This is reasonable because the polymer composition does not directly affect the electrophoretic properties of particles which are determined by their surface charge. Table 5.4 summarizes the properties of the investigated particles, a SEM image is shown in figure 5.16. Of special interest for our experiments are the particle diameter which determines their thermal velocity (equation 2.8), the bulk electrophoretic mobility which characterizes the velocity at which nanoparticles are moving in an external electric field (equation 2.43), and the salt concentration in our sample which determines the Debye lengths of the electrode and the particles (equation 2.8).

Figure 5.17 depicts the scales at which our observations and parameters are taking place. Note that the intensity of the light scattered by a particle depends on its distance from the electrode as the evanescent field of the surface plasmon is exponentially decaying with the distance from the gold electrode.

To verify the absence of electrochemical reactions within the observed voltage range, cyclic voltammetry measurements have been performed. Figure 5.18 shows the cyclic voltammogram of a 1 mM NaCl solution without and with polystyrene nanoparticles. The curves show the same peaks, thus electrode processes in which

Table 5.4.: Parameters of the polystyrene nanoparticle dispersion used in the REDLS experiment.

Property	**Value**	**Source**
particle diameter	$(40 \pm 1)\,\mathrm{nm}$	DLS
electrophoretic mobility	$(-3.37 \pm 0.06) \times 10^{-4}\,\mathrm{cm^2\,V^{-1}\,s^{-1}}$	Zetasizer
particle concentration	0.1 wt%	datasheet
NaCl concentration	$10\,\mathrm{mmol\,L^{-1}}$	calculated
Debye length	3 nm	calculated

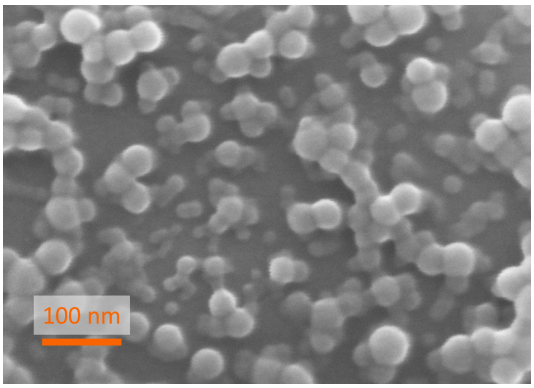

Figure 5.16.: SEM image of the $d = 40\,\text{nm}$ polystyrene nanoparticles used in the REDLS experiment.

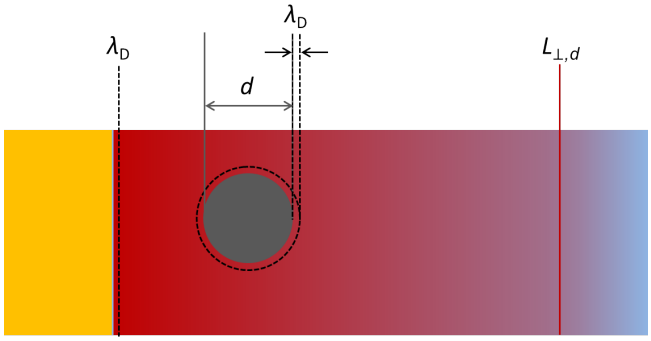

Figure 5.17.: Original scale ratios for the REDLS experiment in an electric field. A part of the gold layer of 48 nm thickness (gold) is shown with the fraction of the surface plasmon (red) that penetrates $L_{\perp,d} = 200\,\text{nm}$ into the sample solution (blue). The particle with the diameter d is depicted in gray. The Debye lengths $\lambda_D = 3\,\text{nm}$ of the gold surface and nanoparticle are also marked.

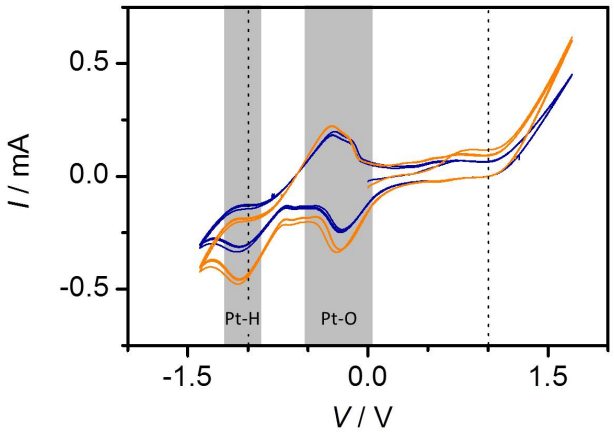

Figure 5.18.: Cyclic voltammogram of an aqueous solution of 1 mM NaCl without (blue) and with (orange) dispersed polystyrene nanoparticles. The traces were measured at 100 mV/s.

the nanoparticles are involved can be excluded. In the voltage range that is considered in the REDLS experiment, only peaks caused by the adsorption and desorption of water are found at ca. $-1\,\mathrm{V}$ (Pt-H) and $-0.25\,\mathrm{V}$ (Pt-OH).

5.2.2. The ACF of REDLS experiments at an electrode interface

Figure 5.19 shows the ACFs of the nanoparticles without the application of any field near a gold surface with a negative surface charge[2] and near a gold electrode while a symmetric square-wave voltage of 1 V and 1 Hz has been applied. The ACF obtained without the application of any field shows one process. It can be fitted by either a single exponential or a KWW function. The relaxation rates are $\Gamma_{Sng} = (1.93 \pm 0.04) \times 10^{-3}\,\mathrm{s}^{-1}$ and $\Gamma_{KWW} = (1.31 \pm 0.01) \times 10^{-3}\,\mathrm{s}^{-1}$ for the single exponential and KWW fit, respectively. They are both significantly lower than the particle diffusion coefficient measured by bulk DLS which is $\Gamma_{bulk} = 3.98 \times 10^{-3}\,\mathrm{s}^{-1}$ at the same scattering vector $q = 18.7 \times 10^{6}\,\mathrm{m}^{-1}$. The low velocity of the particles is attributed to hydrodynamic interactions with the surface (section 2.3). The low KWW stretching factor $\beta = 0.754 \pm 0.006$ compared to the bulk measurement $\beta = 0.974 \pm 0.013$ is due to the high penetration length of the surface plasmon in comparison to the particle radius. The smaller

[2]The gold surface has been functionalized with 1-mercaptoundecanoic acid.

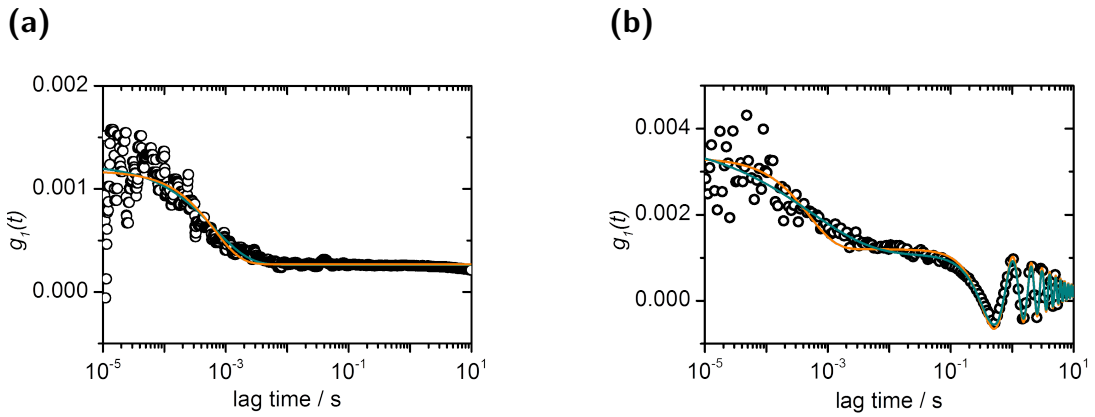

Figure 5.19.: ACFs obtained in REDLS measurements at $q = 18.7 \times 10^{-6}\,\mathrm{m}^{-1}$ **(a)** without the application of a voltage and **(b)** when a square-wave voltage of 1 V and 1 Hz has been applied. Black circles (○) are the experimental data in both plots. In **(a)**, the orange (–) and green (–) lines represent the fit by a single exponential and a KWW function. In **(b)**, the green line represents the fit with equation 5.1 in which the relaxation rate of the fast process has been fixed at the value obtained for the relaxation rate without the application of any field, $\Gamma_{exp} = \Gamma_{E=0,Sng}$. Consequently, the stretching factor $\beta = 1$ also has been fixed. The green line represents a fit with all parameters free to vary.

the particles, the more pronounced is the broadening of the ACF. [135] The effect of the gold surface on the particle dynamics, e.g. due to hydrodynamic interactions, varies depending on their distance from the surface.

Taking a look on the ACF obtained during the application of an AC electric field on the sample, the major difference is that two processes can be distinguished. The first is expressed in the ACF as an exponential decay, the second as a damped periodic oscillation. The ACF can be fitted with a function of the form

$$g_1(t) = \underbrace{A \cdot \exp(-(\Gamma_{exp} t)^{\beta})}_{\text{fast process}} + \underbrace{B \cdot \cos(\omega_{cos} t) \cdot \exp(-\Gamma_{cos} t)}_{\text{slow, periodic process}} \tag{5.1}$$

where A and B are the amplitudes of the purely exponential and periodic part, Γ_{exp}, Γ_{cos} the respective decay rates, β the stretching factor, ω_{cos} the cosine frequency, and t the lag time.

The decay rate of the fast process remains in the same range for all voltage amplitudes and frequencies (figure 5.20). The average values are $\Gamma_{exp} = (1.78 \pm 0.41)\,\mathrm{ms}^{-1}$ and $\Gamma_{exp} = (1.05 \pm 0.30)\,\mathrm{ms}^{-1}$ for the single exponential and

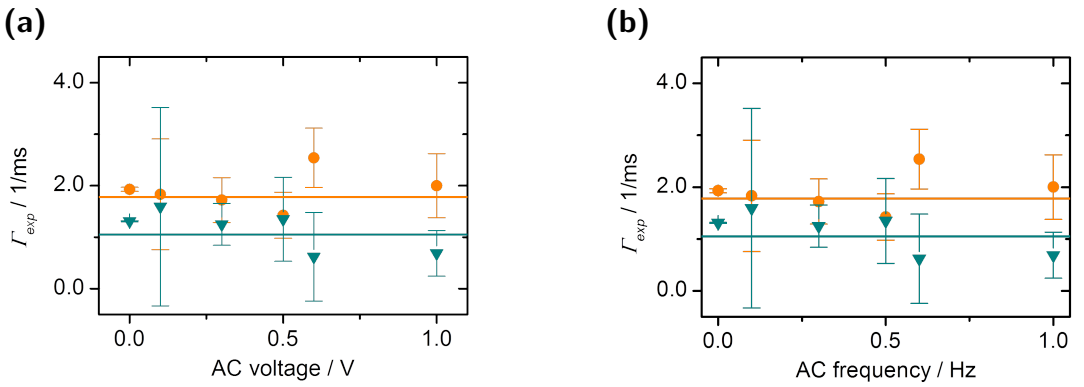

Figure 5.20.: Relaxation rates of the exponential, fast process of the ACFs measured with and without the application of an electric voltage. Orange circles (●) and green triangles (▼) represent the results obtained by fitting with a single exponential and KWW function, respectively. The lines mark the averages.

the KWW fit, respectively. The errors are the respective standard deviation. Due to the fact that this exponential process seems to be identical with the one measured without the application of any field, it can be attributed to the thermal motion of the particles which is still present if they experience an external, directed force. The values from the fit with a single exponential are always higher than the ones obtained with the KWW fit. This is due to the fact that the single exponential underestimates the "tail" of the ACFs which is in our case in the range of 10^{-3} to 10^{-2} s. It is attributed to hydrodynamic interactions of the nanoparticles with the electrode surface as well as to the reversible adsorption and desorption of particles to the solid surface. [43,136,137] The relatively large errors are mainly due to the low signal-to-noise ratio in the sub-millisecond regime. One reason for this is the limited correlation time in the electric field to make sure that the system stays in the same state and the other reason is that only a fraction of the particles causes the second process. This will be explained in the next sections that focus on the periodic process and its relation to the amplitude and frequency of the applied voltage.

5.2.3. Effect of the AC frequency on the nanoparticle dynamics

For the following experiments, REDLS measurements have been performed at various frequencies from $f_{AC} = 0.6$ to 10 Hz at a fixed voltage of $V = 1$ V.

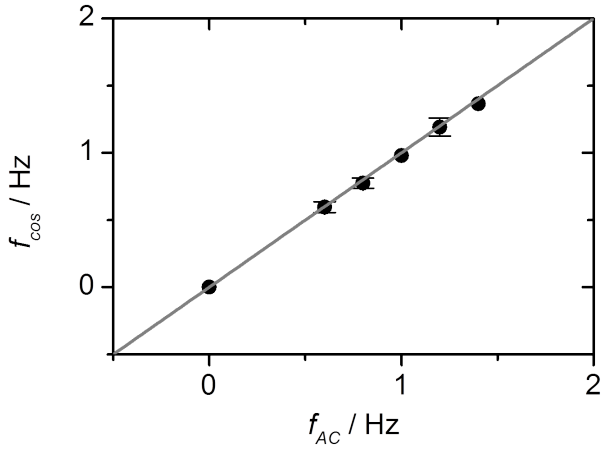

Figure 5.21.: Frequency of the periodic slow process observed in the ACF versus the frequency of the applied voltage. The gray line (–) represents $f_{cos} = f_{AC}$; $\omega_{cos} = 2\pi f_{cos}$.

The major effect of a changing AC frequency is that the frequency of the ACF changes accordingly (figure 5.21). The particles move periodically away and towards the electrode with the alternation of the AC voltage. The closer they are to the electrode, the higher the intensity of the evanescent field and thus the intensity of the scattered light (figure 5.17). Additionally, we expect the particles not to be equally distributed in the sample cell if a voltage is applied. Moreover, the local particle concentration near the oppositely charged electrode should be increased, giving another reason for the periodic fluctuation of the scattering intensity. The ACF of a periodic function is always also periodic and has the same frequency. In our case, the amplitude of the electric part of the scattered field $E(t) = \sqrt{I(t)}$ is periodic

$$E_{sc}(t) = E_{sc}(t + nT), \tag{5.2}$$

therefore

$$g_1(nT) = \int_{-\infty}^{+\infty} E(t) \cdot E(t + nT)dt = \int_{-\infty}^{+\infty} E(t) \cdot E(t) = g_1(0). \tag{5.3}$$

Not only the frequency of the damped cosine depends on the frequency of the

applied voltage, also its relative amplitude

$$A_{cos} = \frac{A_{cos}}{A_{exp} + A_{cos}} \tag{5.4}$$

varies (figure 5.22). To explain those observations, we have to take a closer look at the processes near the electrode interface during one AC period. As soon as the electrode is becoming anodic, the negatively charged nanoparticles start moving towards the electrode, the particle concentration near the interface increases thereby. At higher concentrations, i.e. higher volume fractions, the mean free path and therefore the diffusion coefficent of the particles is lower. Michailidou and coworkers found in evanescent wave DLS that at volume fractions around $\phi = 0.36$, the diffusion coefficient of particles is decreased by a factor of four compared to $\phi = 0.002$. [138] In our scenario, volume fractions near the electrode of $\phi = 0.33$ are feasible (calculation in appendix A.2). Those relatively ordered particles very near to the electrode interface collectively move up and down as the electrode voltage cycles, giving rise to the damped cosine in the ACF. Farther away from the electrode, the particle concentration is lower, the mean free path is not decreased by neighboring particles at close distances. Brownian motion determines the particle diffusion, giving rise to the exponential decay in the ACF.

This model fits the observation that the periodic process is only observed at lower frequencies around 1 Hz. The ordering of the particles which leads to high volume fractions near the electrode takes some time, probably longer than the 50 ms available in half a period of an AC field with a frequency of 10 Hz. However, this model does not explain the increase of A_{cos} with frequency in the range between 0.6 and 1.4 Hz. Our findings for the low frequency range can be explained by electrode polarization: If an AC voltage is applied, electrodes immersed in electrolytes polarize, i.e. an electrochemical double layer forms at their surfaces and partially shields the electrode charge towards the neighboring medium, in our case the nanoparticle dispersion. At low frequencies, the time during which the applied field is pointing towards one direction is long enough that a completely closed electrochemical double layer can build up. At higher frequencies, it only forms partially, leading to a higher potential in the medium next to the electrode and a longer Debye length. Mirtraheri and coworkers [139] who investigated the frequency-dependent polarization of a gold electrode in NaCl solutions of different

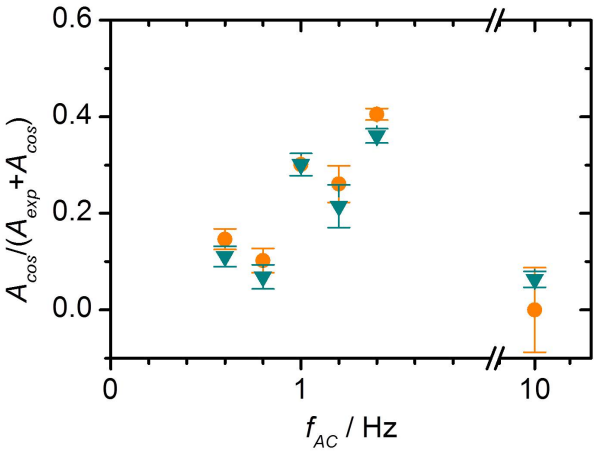

Figure 5.22.: Amplitude fraction of the damped cosine of the ACF versus the applied AC frequency. The orange circles (●) and green triangles (▼) represent the values obtained by fitting with a single exponential and a KWW function for the exponential part.

concentrations showed that the polarization is decreasing with increasing AC frequency. This means, the electrostatic interaction between the electrode and the particles is getting stronger with increased AC frequency. Consequently, the particles are stronger influenced by the electrode at higher AC frequencies. Only at sufficiently high frequencies, in our case at 10 Hz, the time needed to achieve a high volume fraction near the electrode plays a role. In this case, only Brownian motion is observed in the REDLS experiment.

This does not mean that the particles are not affected by the electrode – it might be that only a small fraction of them is affected by the changing potential of the electrode. In this case, the signal caused by them just might be not resolved against the much stronger signal caused by the particles which are undergoing free Brownian motion. However, the signal can be resolved in a fluorescence correlation experiment. Thus, the sample of fluorescently labeled polystyrene nanoparticles with carboxyl groups on their surface, the same diameter of 40 nm, and about the same ζ-potential is used instead of sulfonated polystyrene nanoparticles (table 5.5). An edge filter with a cut-off wavelength of $\lambda = 650$ nm has been added to the detection beam path to ensure detection of light emitted by the fluorescence of the particles only. As in the REDLS experiment, the fluorescent light was detected using single photon-counting detectors and correlated for analysis of the ACFs.

Table 5.5.: Parameters of the fluorescent particle sample.

Property	Value	Source
particle diameter	40 nm	datasheet
electrophoretic mobility	$-2.67\,\mathrm{cm^2\,V^{-1}\,s^{-1}}$	Zetasizer
particle concentration	0.1 wt%	datasheet
NaCl concentration	1 mM	calculated
Debye length	10 nm	calculated

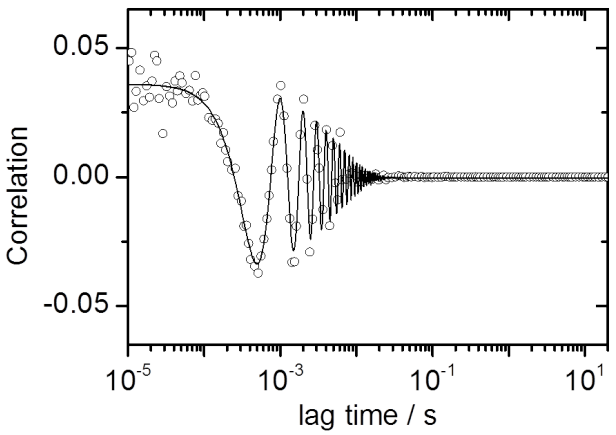

Figure 5.23.: Example of an ACF obtained in a fluorescence experiment under the application of an AC voltage (V =1 V, f = 1 kHz).

The exponential decay cannot be detected by this experiment because the random fluctuation of the fluorescence intensity compared to the overall fluorescence intensity emitted by the sample is negligible at our high concentration compared to regular FCS experiments. Only the particles which are closest to the electrode and periodically approach and retract from it are causing a signal which can be fitted with a damped cosine function (figure 5.23 and appendix B.2)

$$g_1(t) = A \exp\left(-\Gamma_{cos} t\right) \cos\left(\omega_{cos} t\right) \tag{5.5}$$

where A is the amplitude, Γ_{cos} the decay rate, ω_{cos} the frequency, and t the lag time.

Figure 5.24 shows that just as in the case for the lower frequencies in the scattering experiment, the cosine frequency of the ACF equals the frequency of the applied AC voltage. With this dataset of a wide range of frequencies, the

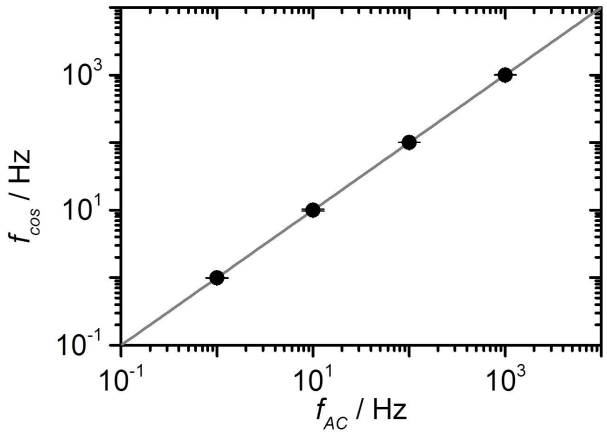

Figure 5.24.: Cosine frequency versus AC frequency measured in the fluorescence experiment. The gray line (–) represents $f_{cos} = f_{AC}$; $\omega_{cos} = 2\pi f_{cos}$.

frequency-dependence of the damping constant also can be analyzed. It increases linearly with the applied frequency (figure 5.25). This confirms our idea that the volume fraction of the particles is increasing near the electrode with the time elapsed since it is negatively charged. The lower the frequency, the more time the particles have to accumulate at the electrode and get into a higher ordered state which results in hindered diffusion and therefore lower diffusion constants.

5.2.4. Effect of the AC voltage on the particle dynamics

In the following series of experiments, the frequency of the applied AC field was kept constant at 1 Hz while the voltage has been varied between 100 and 1000 mV. For all voltages, the ACF consists of a rapidly decaying exponential function and a damped cosine. The relative amplitude of the latter increases with the applied voltage (figure 5.26). This supports the findings obtained in the frequency-dependent experiments. The higher the applied voltages, the higher is the potential near the electrode. When a certain voltage V_1 is applied at the electrode, a potential Ψ is found at a distance z_1 from the electrode. The same potential Ψ is measured farther away from the electrode if a higher voltage $V_2 > V_1$ is applied. Consequently, more particles are affected by the field when the voltage is increased, therefore the amplitude of the cosine is stronger.

The increase of the amplitude due to a higher particle concentration near the electrode due to higher voltages can be excluded as the damping constant is at

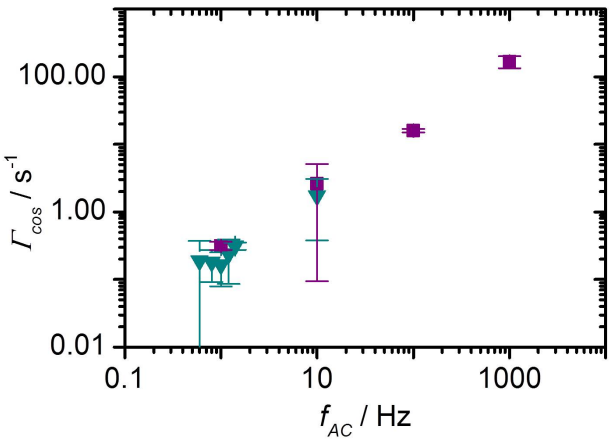

Figure 5.25.: Decay rates of Γ_{cos} measured by REDLS (▼) and the fluorescence correlation experiment (■) at various frequencies and a voltage of 1 V.

the same level for all measurements (figure 5.27).

5.2.5. Layer formation

In the previous section it has been shown that the volume fraction of particles near the electrode is higher than in the remaining sample volume and that particles near the electrode are diffusing orders of magnitude slower than near a gold surface at which no potential is applied. This raises the question if the particles are interacting strongly enough with the electrode to form a layer there. To answer this question, reflectivity measurements have been conducted after the application of a voltage of 1 V and various frequencies. Figure 5.28 shows that the angle of SPR does not shift as it would be the case if a layer is formed. In this case, a shift of the angle of the surface plasmon resonance to higher angles would be observed, i.e. a shift of the angle of SPR by $\Delta\theta_{SPR} = 6.1°$ is expected if a closed monolayer is deposited (calculation see A.3).

However, larger particles ($d = 100$ nm) in a 0.01 mM NaOH solution formed a layer on the electrode surface under the influence of an AC voltage of 1 V and 1 Hz as revealed by a reflectivity measurement (figure 5.29). The observed shift of the angle of surface plasmon resonance $\Delta\theta_{SPR} = 1.2°$ corresponds to a gold surface coverage of 22% with particles (calculation see appendix A.3). The ACF in this case looked quite different to the ACFs obtained for the smaller nanopar-

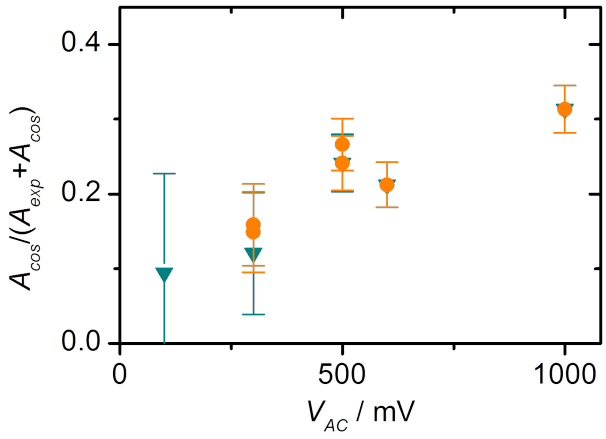

Figure 5.26.: Amplitude fraction of the damped cosine of the ACF versus the AC voltage. The orange circles (●) and green triangles (▼) represent the values obtained by fitting with a single exponential and a KWW function for the exponential part.

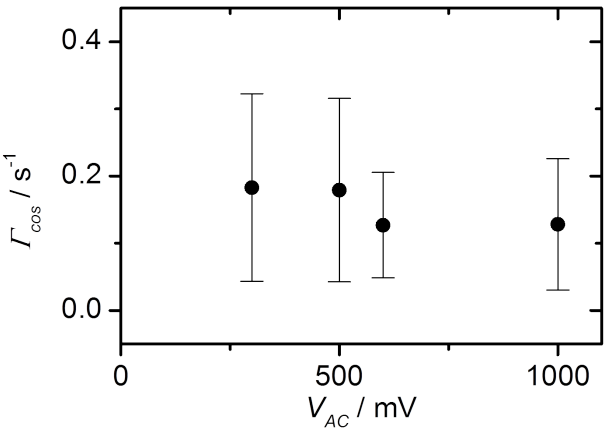

Figure 5.27.: Damping constant of the cosine part of the ACF versus the magnitude of the applied voltage. For the fit procedure of the damping constant see appendix B.1.

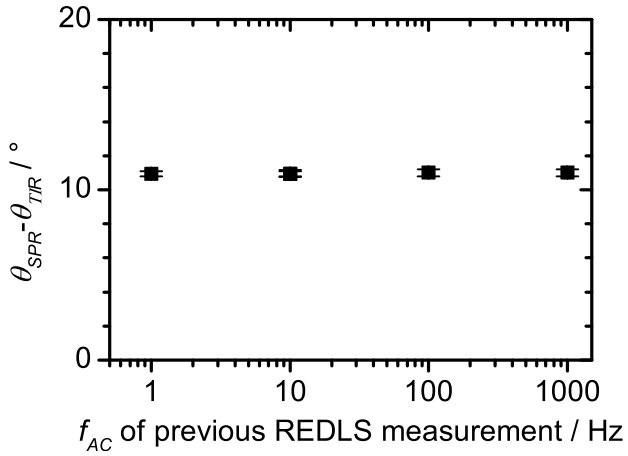

Figure 5.28.: Shift of the angle of surface plasmon resonance, measured after each application of the AC field.

Table 5.6.: Relaxation rates of the exponentially decaying ACFs of a sample of PS particles with a diameter of 100 nm in a 0.01 mM NaOH solution in bulk, at a functionalized gold surface and near a gold electrode, each measured at a scattering vector of $q = 18.7 \times 10^6\,\mathrm{m}^{-1}$.

conditions	Γ_{KWW} **in** $\mathbf{ms^{-1}}$
DLS	2.54 ± 0.07
regular REDLS	$(9.83 \pm 0.29) \cdot 10^{-1}$
REDLS at $V = 1\,\mathrm{V}$; $f = 1\,\mathrm{Hz}$	$(4.33 \pm 0.18) \cdot 10^{-4}$

The gold surface was negatively charged by functionalization with 1-mercaptoundecanoic acid.

ticles under the application of a voltage, only one slowly decaying exponential is observed. Its relaxation rate is three orders of magnitude lower than the relaxation rates at a gold surface without the application of a voltage or of bulk diffusion (table 5.6).

The differences of the observations for the smaller and the larger nanoparticles can only be explained by the high thermal velocity of the smaller particles which allows them to escape the potential near the electrode.

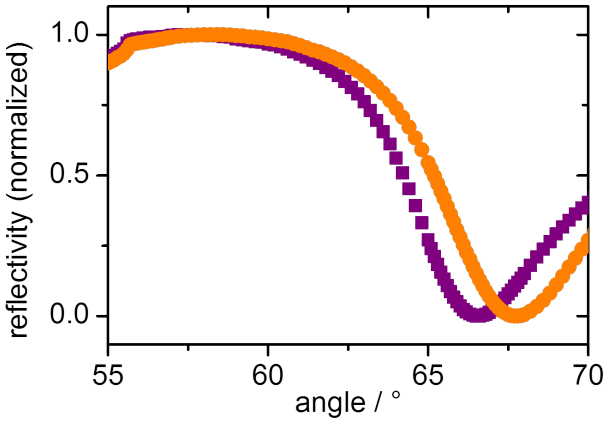

Figure 5.29.: Reflectivity curves of the dispersion of the large particles ($d = 97$ nm) before (purple squares ■) and after (orange circles ●) the application of an AC voltage to the electrode.

Table 5.7.: Sample parameters of the large particles.

Property	**Value**	**Source**
particle diameter	(97 ± 3) nm	data sheet
electrophoretic mobility	$(-1.71 \pm 0.12) \times 10^{-4}\,\mathrm{cm^2\,V^{-1}\,s^{-1}}$	Zeta sizer
particle concentration	0.01 wt%	data sheet
NaCl concentration	10 mM	calculated
Debye length	3 nm	calculated

5.2.6. Considerations to the mechanism of electrophoretic deposition

In this section, the previously shown results are discussed in the framework of electrophoretic deposition and other experimental findings on the behavior of particles near electrode interfaces.

The deposition yield in EPD experiments strongly depends on the AC frequency. The higher it is, the lower the deposition yield. [140,141] This is in accordance with our findings that the thermal velocity of the particles increases with the frequency. Faster particles are less likely to settle at the electrode as slower ones. We have attributed the higher velocity to a larger interparticle distance which has been directly observed by Nadal and coworkers in microscope imaging experiments on microparticles. [23]

Several groups have observed that the deposition yield in EPD experiments increases with the applied voltage. [24,55,60,142] This corresponds to our explanation that more particles are affected by the electrode potential at higher voltages. However, an elevated deposition yield should lead to a decreased particle velocity. In the REDLS experiments, a voltage change did not influence the thermal velocity of the particles.

The fact that the larger particles partially settle on the electrode while the smaller particles do not adsorb can be attributed to their lower thermal velocity. [55]

Even if deposition occurred only in the experiment with larger particles, the findings from the REDLS experiments on the dynamics of nanoparticles near electrodes can be compared with the different mechanisms which are suggested for EPD.

- The mechanism suggested by Grillon which involves electrochemical reactions at the electrode can be excluded for our system as cyclovoltammetric measurements proved their absence. [58]

- The model of interparticle repulsion-induced deposition as proposed by Hamaker and Verwey matches our observation that the thermal velocity of particles near the electrode surface is decreased by the order of magnitudes. [54]

- Flocculation due to an increased ion concentration originating from electro-

chemical reactions at the electrode was proposed by Koelmans but can be excluded for our system. [59] Cyclovoltammetric measurements have shown that in the investigated volatge range, no electrochemical processes are taking place.

- The thinning of the electrochemical double layer of the particles due to the influence of the electric field as proposed by Sarkar and Nicholson can be neither excluded nor proven as a possible mechanism. [60]

In conclusion, the mechanisms suggested by Hamaker and Verwey as well as by Sarkar and Nicholson are in good accordance with our results. Koelmans' and Grillon's suggestions do not match our obersvations as cyclovoltammetric measurements did not show any electrochemical reactions.

5.2.7. Differences to regular electrophoretic light scattering

A reader familiar with electrophoretic light scattering might ask why the fast process associated with the exponential decay at short lag times of the ACF does not have a cosine shape as it should be the case for nanoparticles undergoing electrophoresis, [97]

$$g_1(t) = A \cdot g_{1,E=0}(t) \cdot \cos\left(\omega_{ELS} t\right) \tag{5.6}$$

in which the cosine frequency is only determined by the electric field strength E, the electrophoretic mobility μ, and the scattering vector $\vec{k}$,

$$\omega_{ELS} = \mu \vec{E} \vec{k} \cos\left(\frac{\theta}{2}\right). \tag{5.7}$$

The first reason is the competition between thermal and electrophoretic velocity of the particles: In order to achieve a sufficient effect on the ACF, the latter must be high compared to the former. To express the minimum ratio of the two terms influencing the particle motion, Ware and Flygare set up the following equation for the resolution R which must be greater than One to achieve a clear effect in the ACF: [97]

$$R = \frac{\omega(q)}{\Gamma(q)} = \frac{\mu E \cos(\theta/2)}{qD} \tag{5.8}$$

Figure 5.30 illustrates the meaning of the resolution. It shows the calculated ACFs for our sample and conditions in the case of the application of electric fields of various strengths. A field strength of $E = 50\,\mathrm{V/cm}$ is not sufficient

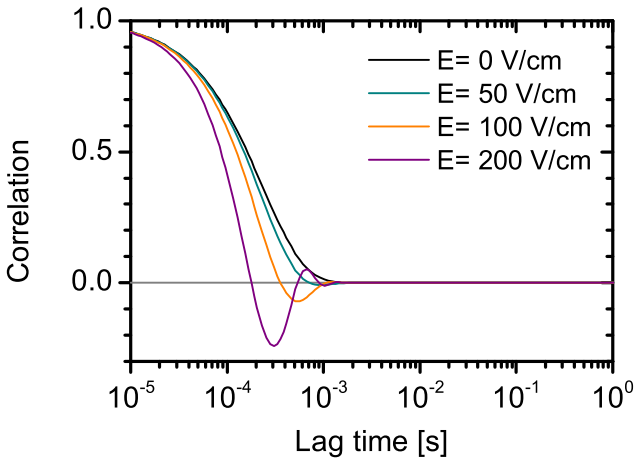

Figure 5.30.: Calculated heterodyne ACF for the sample and conditions used in this thesis ($d = 40\,\mathrm{nm}$; $\theta = 90°$; $D = 1.23 \times 10^{-11}\,\mathrm{s/m^2}$; $\mu = -3.3\,\mathrm{cm^2\ V^{-1}\ s^{-1}}$; $\zeta = -43\,\mathrm{mV}$.

to resolve the electrophoretic motion of the particles. Only at $E \gg 100\,\mathrm{V/cm}$, the cosine part is resolved in the ACF. This is in accordance with the fact that equation 5.8 would be greater than One only for field strengths higher than about $60\,\mathrm{V\,cm^{-1}}$.

The second reason why the electrophoresis of particles further away from the electrode cannot be resolved is that the electrophoretic mobility of nanoparticles has been demonstrated to decrease near the electrode. This can already be observed for distances in the 1 mm range. [143] In our experiment, the scattering and therefore detection volume reaches only 200 nm from the electrode into the sample, therefore we do not expect the particles to have their full electrophoretic mobility which has been measured by the ζ-potential analyzer.

The third reason for the differing appearance of the ACF from typical ACFs measured in electrophoretic light scattering experiments is that the according theory is based on the assumption that the overall particle concentration in the scattering volume is constant. This is only possible if the particles leaving the scattering volume due to electrophoresis are replaced by new ones entering from the opposite direction. In a REDLS experiment, the measurements are taking place directly at the electrode which also doubles as the wall of the measurement cell. New particles cannot enter the detection volume if particles are forced away from it or leave it if they are forced towards it. Consequently, the particle concentration in the scattering volume is not constant over the measurement

period.

In summary, our field strengths are to weak and the detection volume is located too close to the electrode to expect an ACF as it is measured in regular electrophoretic light scattering experiments. Additionally, care should be taken on the application of electrophoretic light scattering theory as it assumes a constant particle concentration in the detection volume.

6. Conclusions

In the first part of this thesis, a new method to prepare functionalized poly(lactic acid)-based (PLA-based) nanoparticles has been presented. One type of those nanoparticles has an increased stability in salt solutions compared to regular PLA nanoparticles, making them particularly suitable for biomedical applications since high salt concentrations are used in cell cultures. The increased stability of the nanoparticles was achieved by introducing additional carboxyl groups that are negatively charged in aqueous environments. For this purpose, copolymers of oligo(lactic acid) with vinyl terminus (HEMA-OLA) and acrylic as well as methacrylic acid in various molar ratios were prepared. The poly((methacrylic acid)-co-(HEMA-OLA)) with the higher number of acid units was then used in combination with preformed PLA in a miniemulsion solvent evaporation process to obtain the functionalized nanoparticles. Furthermore, it was shown that the copolymerization as well as the miniemulsion solvent evaporation step can be carried out within one step, yielding sufficiently equal results. In both cases, the surface charge and therefore stability in salt solutions is high compared to a control sample that was prepared from PLA and HEMA-OLA without the addition of methacrylic acid. Consequently, for some applications it might be sufficient to follow the more convenient one-step procedure even if the stability under salty conditions is slightly better for the particles prepared in the two-step procedure.

A mandatory requirement for the use of nanoparticles in fluorescent imaging experiments, which are common in life sciences, is the stable binding of the fluorescent dyes since their release during the experiment might falsify the results. Such a system was prepared for this work, following the same procedure as for the carboxyl-functionalization of nanoparticles. A fluorescent copolymer of HEMA-OLA and a polymerizable BODIPY dye were used to prepare the nanoparticles. They were shown to hold the dye for more than two weeks, making them eligible for use in fluorescence imaging experiments to monitor the uptake and metabolism

of nanoparticles by cells.

While the use of nanoparticles for medical applications is still on its way to everyday application, nanoparticles are already widely used in industrial coating processes, e.g. for electrophoretic deposition. The mechanism of this process has not been fully understood yet. However, it is known that the dynamics of nanoparticles near the electrode interface play a crucial role for the successful deposition. In order to investigate the dynamic behavior of nanoparticles in dispersion near an electrode at which an AC voltage has been applied, a REDLS experiment was developed in which the gold layer, which is necessary for the excitation of the surface plasmon, doubles as an electrode. High field strengths could be applied at low voltages due to the close distance of only about 150 µm between the electrodes. Nanoparticle layers which have possibly deposited at the electrode can be instantly characterized in terms of thickness and surface covering by reflectivity measurements without the need to remove the electrode from the experimental setup. The main advantage of this method is that the nanoparticle motion can be monitored in situ and at four different scattering angles simultaneously. From the results on the frequency, voltage, and particle diameter dependence of the nanoparticle dynamics near the electrode, it could be concluded that the particle deceleration and the increase of their concentration near the electrode due to electrophoresis are the most important factors for a successful electrophoretic deposition. In the investigated case of polystyrene nanoparticles, electrochemical mechanisms could be excluded as possible reasons for electrophoretic deposition.

Both primary results of this work, the synthesis of functionalized PLA-based nanoparticles and the findings on the nanoparticle dynamics near electrodes, enable future applications. One possible area of research might be the development of PLA-based biocompatible surface coatings for use in implants. Even higher charged nanoparticles would lead to better coating results. In order to reach this, vinyl phosphate could be used instead of methacrylic acid. Due to its higher acidity, its relative amount in the copolymer can be kept low in order to maintain the other nanoparticle characteristics like biocompatibility.

Bibliography

[1] M. Urban, A. Musyanovych, and K. Landfester. "Fluorescent Superparamagnetic Polylactide Nanoparticles by Combination of Miniemulsion and Emulsion/Solvent Evaporation Techniques". In: *Macromol. Chem. Phys.* 210.11 (2009), pp. 961–970.

[2] Y. Dong and S.-S. Feng. "In vitro and in vivo evaluation of methoxy polyethylene glycol-polylactide (MPEG-PLA) nanoparticles for small-molecule drug chemotherapy". In: *Biomaterials* 28.28 (2007), pp. 4154–4160.

[3] S. H. Lee, Z. Zhang, and S.-S. Feng. "Nanoparticles of poly(lactide)tocopheryl polyethylene glycol succinate (PLA-TPGS) copolymers for protein drug delivery". In: *Biomaterials* 28.11 (2007), pp. 2041–2050.

[4] E. Leo et al. "In vitro evaluation of PLA nanoparticles containing a lipophilic drug in water-soluble or insoluble form". In: *International Journal of Pharmaceutics* 278.1 (2004), pp. 133–141.

[5] T. Niwa et al. "Preparations of biodegradable nanospheres of water-soluble and insoluble drugs with D,L-lactide/glycolide copolymer by a novel spontaneous emulsification solvent diffusion method, and the drug release behavior". In: *Journal of Controlled Release* 25.1-2 (1993), pp. 89–98.

[6] M. K. Lai and R. C. C. Tsiang. "Encapsulating acetaminophen into poly(L-lactide) microcapsules by solvent-evaporation technique in an O/W emulsion". In: *Journal of Microencapsulation* 21.3 (2004), pp. 307–316.

[7] R. T. Liggins and H. M. Burt. "Paclitaxel loaded poly(lactic acid) (PLLA) microspheres II. The effect of processing parameters on microsphere morphology and drug release kinetics". In: *International Journal of Pharmaceutics* 281.1-2 (2004), pp. 103–106.

[8] Y. Zhang et al. "Cytotoxicity of organic surface coating agents used for nanoparticles synthesis and stability". In: *Toxicology in Vitro* 29.4 (2015), pp. 762–768.

[9] F. Li et al. "Novel surfactant for preparation of poly(l-lactic acid) nanoparticles with controllable release profile and cytocompatibility for drug delivery". In: *Colloids and Surfaces B: Biointerfaces* 115 (2014), pp. 377–383.

[10] J. Dausend et al. "Uptake Mechanism of Oppositely Charged Fluorescent Nanoparticles in HeLa Cells". In: *Macromolecular Bioscience* 8.12 (2008), pp. 1135–1143.

[11] O. Harush-Frenkel et al. "Surface Charge of Nanoparticles Determines Their Endocytic and Transcytotic Pathway in Polarized MDCK Cells". In: *Biomacromolecules* 9.2 (2008), pp. 435–443.

[12] M. R. Lorenz et al. "Uptake of functionalized, fluorescent-labeled polymeric particles in different cell lines and stem cells". In: *Biomaterials* 27.14 (2006), pp. 2820–2828.

[13] X. Jiang et al. "Specific effects of surface carboxyl groups on anionic polystyrene particles in their interactions with mesenchymal stem cells". In: *Nanoscale* 3.5 (2011), pp. 2028–2035.

[14] A. Pfister et al. "Boron polylactide nanoparticles exhibiting fluorescence and phosphorescence in aqueous medium". In: *ACS Nano* 2.6 (2008), pp. 1252–1258.

[15] A. Rogach et al. "Electrophoretic deposition of latex-based 3D colloidal photonic crystals: a technique for rapid production of high-quality opals". In: *Chemistry of Materials* 12.9 (2000), pp. 2721–2726.

[16] M. Marin-Suarez et al. "Electrophoretic deposition as a new approach to produce optical sensing films adaptable to microdevices". In: *Nanoscale* 6 (1 2014), pp. 263–271.

[17] D. Zhitomirsky et al. "Electrophoretic deposition of bioactive glass/polymer composite coatings with and without HA nanoparticle inclusions for biomedical applications". In: *Journal of Materials Processing Technology* 209.4 (2009), pp. 1853–1860.

[18] P. J. Sides. "Electrohydrodynamic particle aggregation on an electrode driven by an alternating electric field normal to it". In: *Langmuir* 17.19 (2001), pp. 5791–5800.

[19] T. J. Woehl et al. "Electrolyte-dependent aggregation of colloidal particles near electrodes in oscillatory electric fields". In: *Langmuir* 30.17 (2014), pp. 4887–4894.

[20] J. A. Fagan, P. J. Sides, and D. C. Prieve. "Vertical oscillatory motion of a single colloidal particle adjacent to an electrode in an AC electric field". In: *Langmuir* 18.21 (2002), pp. 7810–7820.

[21] J. D. Hoggard, P. J. Sides, and D. C. Prieve. "Electrolyte-dependent pairwise particle motion near electrodes at frequencies below 1 kHz". In: *Langmuir* 23.13 (2007), pp. 6983–6990.

[22] D. C. Prieve, P. J. Sides, and C. L. Wirth. "2-D assembly of colloidal particles on a planar electrode". In: *Current Opinion in Colloid & Interface Science* 15 (2010), pp. 160–174.

[23] F. Nadal et al. "Electrically induced interactions between colloidal particles in the vicinity of a conducting plane". In: *Physical Review E* 65.6 (2002), p. 061409.

[24] K. H. Bhatt, S. Grego, and O. D. Velev. "An AC electrokinetic technique for collection and concentration of particles and cells on patterned electrodes". In: *Langmuir* 21.14 (2005), pp. 6603–6612.

[25] W. Ristenpart, I. Aksay, and D. Saville. "Electrically driven flow near a colloidal particle close to an electrode with a faradaic current". In: *Langmuir* 23.7 (2007), pp. 4071–4080.

[26] R. M. Rock, P. J. Sides, and D. C. Prieve. "The effect of electrode kinetics on electrophoretic forces". In: *Journal of colloid and interface science* 393 (2013), pp. 306–313.

[27] C. L. Wirth et al. "Single and pairwise motion of particles near an ideally polarizable electrode". In: *Langmuir* 27.16 (2011), pp. 9781–9791.

[28] M. A. Plum et al. "Probing dynamics at interfaces: resonance enhanced dynamic light scattering". In: *Optics Express* 17.12 (2009), p. 10364.

[29] H. Helmholtz. "Studien über electrische Grenzschichten". In: *Annalen der Physik* 243.7 (1879), pp. 337–382.

[30] L. G. Gouy. "Sur la constitution de la charge électrique à la surface d' un électrolyte". In: *Journal de Physique Théorique et Appliquée* 9.1 (1910), pp. 457–468.

[31] D. L. Chapman. "A contribution to the theory of electrocapillarity". In: *Philosophical Magazine* 24.148 (1913), pp. 475–481.

[32] O. Stern. "The theory of the electrolytic double-layer". In: *Zeit. Elektrochem.* 30 (1924), pp. 508–516.

[33] B. Derjaguin and L. Landau. "Theory of stability of highly charged lyophobic sols and adhesion of highly charged particles in solutionsof electrolytes". In: *Zhurnal Eksperimentalnoi i Teoreticheskoi Fiziki* 15.11 (1945), pp. 663–682.

[34] B. Derjaguin and L. Landau. "Theory of the stability of strongly charged lyophobic sols and of the adhesion of strongly charged particles in solutions of electrolytes". In: *Progress in Surface Science* 43.1-4 (1993), pp. 30–59.

[35] E. J. W. Verwey and J. T. G. Overbeek. "Long distance forces acting between colloidal particles". In: *Trans. Faraday Soc.* 42 (1946), pp. 117–123.

[36] H. Hamaker. "The London & van der Waals attraction between spherical particles". In: *Physica* 4.10 (1937), pp. 1058–1072.

[37] E. M. Lifshitz. "The theory of molecular and attractive forces between solids". In: *Soviet Physics JETP-USSR* 2.1 (1956), pp. 73–83.

[38] J. Laven and J. P. Vissers. "The Hamaker and the Lifshitz approaches for the Van der Waals interaction between particles of composite materials dispersed in a medium". In: *Colloids and Surfaces A: Physicochemical and Engineering Aspects* 152.3 (1999), pp. 345–355.

[39] A. Einstein. "Über die on der molekularkinetischen Theorie der Wärme geforderte Bewegung von in ruhenden Flüssigkeiten suspendierten Teilchen". In: *Annalen der Physik* 322.8 (1905), pp. 549–506.

[40] M. Smoluchowski. "Zur kinetischen Theorie der Brownschen Molekularbewegung und der Suspensionen". In: *Annalen der Physik* 326.14 (1906), pp. 756–780.

[41] H.-J. Butt and M. Kappl. *Surface and Interfacial Forces*. Wiley-VCH, 2010.

[42] H. Brenner and J. Happel. *Low Reynolds number hydrodynamics: with special applications to particulate media*. Springer-Verlag, 1983.

[43] P. Holmqvist, J. K. Dhont, and P. R. Lang. "Colloidal dynamics near a wall studied by evanescent wave light scattering: Experimental and theoretical improvements and methodological limitations". In: *The Journal of Chemical Physics* 126.4 (2007), p. 044707.

[44] M. E. O'Neill. "A slow motion of viscous liquid caused by a slowly moving solid sphere". In: *Mathematika* 11 (02 1964), pp. 67–74.

[45] H. Faxen. "The resistance against the movement of a rigour sphere in viscous fluids, which is embedded between two parallel layered barriers". In: *Annalen der Physik* 68.10 (1922), pp. 89–119.

[46] M. A. Plum et al. "Anisotropic hindered motion close to an interface studied by resonance-enhanced dynamic light scattering". In: *New Journal of Physics* 12.10 (2010), p. 103022.

[47] D. C. Grahame. "The electrical double layer and the theory of electrocapillarity". In: *Chemical Reviews* 41.3 (1947), pp. 441–501.

[48] M. Smoluchowski. "Contribution à la théorie de l'endosmose électrique et de quelques phénomènes corrélatifs". In: *Bulletin International de l'Académie des Sciences de Cracovice* 3 (1903), pp. 182–199.

[49] E. Hückel. "The cataphoresis of the sphere". In: *Physikalische Zeitschrift* (1924).

[50] S. Semenekhin N.M .and Dukhin. "Calculation of electrophoretic mobility of a spherical particle, with account taken of polarization of a moderately thin double-layer". English. In: *Colloid Journal of the USSR* 37.6 (1975), 1017–1022.

[51] A. Dukhin and T. van de Ven. "Electrokinetic characterization of polydisperse colloidal particles". In: *Journal of Colloid and Interface Science* 165.1 (1994), pp. 9–18.

[52] F. F. Reuß. "Notice sur un nouvel effet de lélectricité galvanique". In: *Mem. de la societé Imp. des Naturalise de Moscou* (1809).

[53] H. C. Hamaker. "Formation of a deposit by electrophoresis". In: *Trans. Faraday Soc.* 35 (1940), pp. 279–287.

[54] H. C. Hamaker and E. J. W. Verwey. "Part II.-(C) Colloid stability. The role of the forces between the particles in electrodeposition and other phenomena". In: *Trans. Faraday Soc.* 35 (1940), pp. 180–185.

[55] L. Besra and M. Liu. "A review on fundamentals and applications of electrophoretic deposition (EPD)". In: *Progress in Materials Science* 52.1 (2007), pp. 1–61.

[56] P. Sides et al. *Electrophoretic Deposition of Nanomaterials*. Ed. by J. H. Dickerson and A. R. Boccaccini. Springer New York, 2012.

[57] B. Neirinck, O. Van der Biest, and J. Vleugels. "A current opinion on electrophoretic deposition in pulsed and alternating fields". In: *The Journal of Physical Chemistry B* 117.6 (2013), pp. 1516–1526.

[58] F. Grillon, D. Fayeulle, and M. Jeandin. "Quantitative image analysis of electrophoretic coatings". English. In: *Journal of Materials Science Letters* 11.5 (1992), pp. 272–275.

[59] H. Koelmans. "Suspensions in Non-Aqueous Media". In: *Philips Research Reports* 10 (1995), pp. 161–193.

[60] P. Sarkar and P. S. Nicholson. "Electrophoretic Deposition (EPD): Mechanisms, Kinetics, and Application to Ceramics". In: *Journal of the American Ceramic Society* 79.8 (1996), pp. 1987–2002.

[61] B. Tieke. *Makromolekulare Chemie*. Wiley-VCH, 2005.

[62] S. Koltzenburg, M. Maskos, and O. Nuyken. *Polymere: Synthese, Eigenschaften und Anwendungen*. Springer, 2014.

[63] K. Ziegler et al. "Das Mülheimer Normaldruck-Polyäthylen-Verfahren". In: *Angewandte Chemie* 67.19-20 (1955), pp. 541–547.

[64] G. Natta. "Stereospezifische katalysen und isotaktische polymere". In: *Angewandte Chemie* 68.12 (1956), pp. 393–403.

[65] O. Dechy-Cabaret, B. Martin-Vaca, and D. Bourissou. "Controlled ring-opening polymerization of lactide and glycolide". In: *Chemical Reviews* 104.12 (2004), pp. 6147–6176.

[66] H. R. Kricheldorf, I. Kreiser-Saunders, and A. Stricker. "Polylactones 48. SnOct2-initiated polymerizations of lactide: A mechanistic study". In: *Macromolecules* 33.3 (2000), pp. 702–709.

[67] A. Kowalski, A. Duda, and S. Penczek. "Mechanism of cyclic ester polymerization initiated with tin (II) octoate. 2. Macromolecules fitted with tin (II) alkoxide species observed directly in MALDI-TOF spectra". In: *Macromolecules* 33.3 (2000), pp. 689–695.

[68] F. R. Mayo and F. M. Lewis. "Copolymerization. I. A basis for comparing the behavior of monomers in copolymerization; the copolymerization of styrene and methyl methacrylate". In: *Journal of the American Chemical Society* 66.9 (1944), pp. 1594–1601.

[69] T. Alfrey and C. C. Price. "Relative reactivities in vinyl copolymerization". In: *Journal of Polymer Science* 2.1 (1947), pp. 101–106.

[70] G. W. B. Burton and C. P. O'Farell. "Preparation of Artificial Latexes". In: *Journal of Elastomers and Plastics* 9.1 (1977), pp. 94–101.

[71] Y. Ogawa et al. "A new technique to efficiently entrap leuprolide acetate into microcapsules of polylactic acid or copoly(lactic/glycolic) acid". In: *Chemical and Pharmaceutical Bulletin* 36.3 (1988). cited By 386, pp. 1095–1103.

[72] J. Molpeceres et al. "Application of central composite designs to the preparation of polycaprolactone nanoparticles by solvent displacement". In: *Journal of pharmaceutical sciences* 85.2 (1996), pp. 206–213.

[73] E. Allémann et al. "In vitro extended-release properties of drug-loaded poly (DL-lactic acid) nanoparticles produced by a salting-out procedure". In: *Pharmaceutical research* 10.12 (1993), pp. 1732–1737.

[74] P. B. O'Donnell and J. W. McGinity. "Preparation of microspheres by the solvent evaporation technique". In: *Advanced drug delivery reviews* 28.1 (1997), pp. 25–42.

[75] D. Quintanar-Guerrero et al. "Preparation techniques and mechanisms of formation of biodegradable nanoparticles from preformed polymers". In: *Drug development and industrial pharmacy* 24.12 (1998), pp. 1113–1128.

[76] S. Freiberg and X. Zhu. "Polymer microspheres for controlled drug release". In: *International journal of pharmaceutics* 282.1 (2004), pp. 1–18.

[77] C. P. Reis et al. "Nanoencapsulation I. Methods for preparation of drug-loaded polymeric nanoparticles". In: *Nanomedicine: Nanotechnology, Biology and Medicine* 2.1 (2006), pp. 8–21.

[78] J. U. John W. Vanderhoff Mohamed S. El-Aasser. "Polymer emulsification process". English. US4177177 A. 1979.

[79] N. Anton, J.-P. Benoit, and P. Saulnier. "Design and production of nanoparticles formulated from nano-emulsion templatesa review". In: *Journal of Controlled Release* 128.3 (2008), pp. 185–199.

[80] A. Graf, A. McDowell, and T. Rades. "Poly(alkycyanoacrylate) nanoparticles for enhanced delivery of therapeutics is there real potential?" In: *Expert Opin. Drug Deliv.* 6.4 (Apr. 2009), 371387.

[81] S. Vrignaud, J.-P. Benoit, and P. Saulnier. "Strategies for the nanoencapsulation of hydrophilic molecules in polymer-based nanoparticles". In: *Biomaterials* 32.33 (2011), pp. 8593–8604.

[82] P. Sansdrap and A.-J. Mos. "Influence of manufacturing parameters on the size characteristics and the release profiles of nifedipine from poly (DL-lactide-co-glycolide) microspheres". In: *International Journal of Pharmaceutics* 98.1 (1993), pp. 157–164.

[83] R. H. Staff et al. "Phase behavior of binary mixtures of block copolymers and a non-solvent in miniemulsion droplets as single and double nanoconfinement". In: *Soft Matter* 7.21 (2011), pp. 10219–10226.

[84] R. M. Mainardes and R. C. Evangelista. "PLGA nanoparticles containing praziquantel: effect of formulation variables on size distribution". In: *International journal of pharmaceutics* 290.1 (2005), pp. 137–144.

[85] Z. Xu et al. "Encapsulation of nanosized magnetic iron oxide by polyacrylamide via inverse miniemulsion polymerization". In: *Journal of Magnetism and Magnetic Materials* 277.1 (2004), pp. 136–143.

[86] D. Schaeffel et al. "Fluorescence correlation spectroscopy directly monitors coalescence during nanoparticle preparation". In: *Nano letters* 12.11 (2012), pp. 6012–6017.

[87] R. H. Staff et al. "Particle Formation in the Emulsion-Solvent Evaporation Process". In: *Small* 9.20 (2013), pp. 3514–3522.

[88] S. Desgouilles et al. "The design of nanoparticles obtained by solvent evaporation: a comprehensive study". In: *Langmuir* 19.22 (2003), pp. 9504–9510.

[89] K. Landfester. "Synthesis of colloidal particles in miniemulsions". In: *Annu. Rev. Mater. Res.* 36 (2006), pp. 231–279.

[90] K. Landfester. "Miniemulsion polymerization and the structure of polymer and hybrid nanoparticles". In: *Angewandte Chemie International Edition* 48.25 (2009), pp. 4488–4507.

[91] M. Knoll and E. Ruska. "Das Elektronenmikroskop". In: *Zeitschrift für Physik* 78.5-6 (1932), pp. 318–339.

[92] R. Erni et al. "Atomic-resolution imaging with a sub-50-pm electron probe". In: *Physical Review Letters* 102.9 (2009), pp. 96–101.

[93] M. Adrian et al. "Cryo-electron microscopy of viruses". In: *Nature* 308.5954 (1984), pp. 32–36.

[94] R. Egerton, P. Li, and M. Malac. "Radiation damage in the TEM and SEM". In: *Micron* 35.6 (2004), pp. 399–409.

[95] *ZEISS GeminiSEM Family*. Product Information. Version 1.0. Carl Zeiss Microscopy GmbH, 07745 Jena, Germany.

[96] J. Lyklema. *Fundamentals of interface and colloid science*. Academic Press, 1991.

[97] B. W. W. Flygare. "The simultaneous measurement of the electrophoretic mobility and diffusion coefficient in bovine serum albumin solutions by light scattering". In: *Chemical Physics Letters* 12.1 (1971), pp. 81–85.

[98] R. Xu. *Particle Characterization: Light Scattering Methods*. Ed. by B. Scarlett. Springer, 2002.

[99] E. L. Elson and D. Magde. "Fluorescence correlation spectroscopy. I. Conceptual basis and theory". In: *Biopolymers* 13.1 (1974), pp. 1–27.

[100] N. L. Thompson. *Topics in fluorescence spectroscopy*. Springer, 1999.

[101] I. Nikiforow et al. "Self-stratification during film formation from latex blends driven by differences in collective diffusivity". In: *Langmuir* 26.16 (2010), pp. 13162–13167.

[102] K. Ishimoto et al. "Biobased polymers: synthesis of graft copolymers and comb polymers using lactic acid macromonomer and properties of the product polymers". In: *Biomacromolecules* 13.11 (2012), pp. 3757–3768.

[103] G. Mie. "Articles on the optical characteristics of turbid tubes, especially colloidal metal solutions." In: *Annalen der Physik* 25.3 (1908), pp. 377–445.

[104] J. B. Berne and R. Pecora. *Dynamic Light Scattering: With Applications to Chemistry, Biology, and Physics*. Dover Publications, 1990.

[105] M. Höbel and J. Ricka. "Dead-time and afterpulsing correction in multiphoton timing with nonideal detectors". In: *Review of Scientific Instruments* 65.7 (1994), pp. 2326–2336.

[106] D. E. Koppel. "Analysis of Macromolecular Polydispersity in Intensity Correlation Spectroscopy: The Method of Cumulants". In: *The Journal of Chemical Physics* 57.11 (1972), pp. 4814–4820.

[107] R. Kohlrausch. "Theorie des elektrischen Rückstandes in der Leidener Flasche". In: *Annalen der Physik* 167.2 (1854), pp. 179–214.

[108] G. Williams and D. C. Watts. "Non-symmetrical dielectric relaxation behaviour arising from a simple empirical decay function". In: *Trans. Faraday Soc.* 66 (1970), pp. 80–85.

[109] S. W. Provencher. "CONTIN: a general purpose constrained regularization program for inverting noisy linear algebraic and integral equations". In: *Computer Physics Communications* 27.3 (1982), pp. 229–242.

[110] S. W. Provencher. "A constrained regularization method for inverting data represented by linear algebraic or integral equations". In: *Computer Physics Communications* 27.3 (1982), pp. 213–227.

[111] J. Vanhoudt and J. Clauwaert. "Experimental Comparison of Fiber Receivers and a Pinhole Receiver for Dynamic and Static Light Scattering". In: *Langmuir* 15.1 (1999), pp. 44–57.

[112] C. P. Lindsey and G. D. Patterson. "Detailed comparison of the Williams-Watts and Colde-Davidson functions". In: *J Chem. Phys.* 73.7 (1980), pp. 3348–3357.

[113] C. Lai, P. B. Macedo, and C. J. Montrose. "Light-scattering measurements of strucutral relaxation in glasses by digital correlation spectroscopy". In: *Journal of the American Ceramic Society* 58.3–4 (1975), pp. 120–123.

[114] J. Zenneck. "Über die Fortpflanzung ebener elektromagnetischer Wellen längs einer ebenen Leiterfläche und ihre Beziehung zur drahtlosen Telegraphie". In: *Annalen der Physik* 23.10 (1907), pp. 846–866.

[115] A. Sommerfeld. "Über die Ausbreitung der Wellen in der drahtlosen Telegraphie". In: *Annalen der Physik* 28.4 (1909), pp. 665–736.

[116] H. Raether. *Surface Plasmons on Smooth and Rough Surfaces and on Gratings*. Springer New York, 1988.

[117] A. Otto. "Excitation of nonradiative surface plasma waves in silver by the method of frustrated total reflection". English. In: *Zeitschrift für Physik* 216.4 (1968), pp. 398–410.

[118] E. Kretschmann. "Die Bestimmung optischer Konstanten von Metallen durch Anregung von Oberflächenplasmaschwingungen". In: *Zeitschrift für Physik* 241.4 (1971), pp. 313–324.

[119] D. Altschuh et al. "Determination of kinetic constants for the interaction between a monoclonal antibody and peptides using surface plasmon resonance". In: *Biochemistry* 31.27 (1992), pp. 6298–6304.

[120] E. F. Aust et al. "Surface plasmon and guided optical wave microscopies". In: *Scanning* 16.3 (1994), pp. 353–362.

[121] A. J. Tudos and R. B. M. Schasfoort. *Handbook of Surface Plasmon Resonance*. Ed. by R. B. M. Schasfoort and A. J. Tudos. The Royal Society of Chemistry, Cambridge, 2008.

[122] J. Homola. "Electromagnetic Theory of Surface Plasmons". In: *Springer Series on Chemical Sensors and Biosensors*. Ed. by O. S. Wolfbeis. Vol. 4. Springer Berlin Heidelberg, 2006.

[123] G. Anzivino et al. "Review of the hybrid photo diode tube (HPD) an advanced light detector for physics". In: *Nuclear Instruments and Methods in Physics Research Section A: Accelerators, Spectrometers, Detectors and Associated Equipment* 365.1 (1995), pp. 76–82.

[124] A. Fukasawa et al. "High Speed HPD for Photon Counting". In: *2006 IEEE Nuclear Science Symposium Conference Record* (2006).

[125] X. Michalet et al. "Hybrid photodetector for single-molecule spectroscopy and microscopy". In: *Single Molecule Spectroscopy and Imaging* (Feb. 2008). Ed. by J. Enderlein, Z. K. Gryczynski, and R. Erdmann.

[126] A. Zeller. "Phosphonat- und phosphatfunktionalisierte Polymerpartikel und Kapseln für biomedizinische Anwendungen wie Implantatbeschichtungen". PhD thesis. Universität Ulm, 2010.

[127] V. Beer et al. "Polylactide-Based Nanoparticles with Tailor-Made Functionalization". In: *Macromolecular Chemistry and Physics* 216.17 (2015), pp. 1774–1781.

[128] E. Klesper, A. Johnsen, and W. Gronski. "NMR study of configurational sequences in polymethacrylic acid". In: *Journal of Polymer Science Part B: Polymer Letters* 8.5 (1970), pp. 369–375.

[129] R. Ferrari et al. "A Methyl Methacrylate–HEMA-CLn Copolymerization Investigation: From Kinetics to Bioapplications". In: *Macromolecular bioscience* 13.10 (2013), pp. 1347–1357.

[130] J. K. Borchardt and E. D. Dalrymple. "Calculation of Alfrey–Price Q-e values from ^{13}C-NMR Data". In: *Journal of Polymer Science: Polymer Chemistry Edition* 20.7 (1982), pp. 1745–1764.

[131] R. Z. Greenley. *Polymer Handbook*. Ed. by J. Brandrup, E. H. Immergut, and E. A. Grulke. Wiley-Interscience, 1999.

[132] I. J. Arroyo et al. "The smallest and one of the brightest. Efficient preparation and optical description of the parent borondipyrromethene system". In: *The Journal of organic chemistry* 74.15 (2009), pp. 5719–5722.

[133] X. Yang et al. "Red fluorescent monobenzo-BODIPY dyes: Solvent effects on spectra and efficient fluorescence quenching by quinones and phenols". In: *Journal of Photochemistry and Photobiology A: Chemistry* 297 (2015), pp. 39–44.

[134] W. Qin et al. "Solvent-dependent photophysical properties of borondipyrromethene dyes in solution". In: *Chemical physics letters* 420.4 (2006), pp. 562–568.

[135] Plum. "Messung dynamischer Prozesse in der Nähe von Grenzflächen mit Hilfe neu entwickelter Lichtstreumethoden". PhD thesis. Johannes Gutenberg-Universität Mainz, 2010.

[136] G. K. Batchelor. "Brownian diffusion of particles with hydrodynamic interaction". In: *Journal of Fluid Mechanics* 74.01 (1976), pp. 1–29.

[137] N. Garnier and N. Ostrowsky. "Brownian dynamics in a confined geometry. Experiments and numerical simulations". In: *Journal de Physique II* 1.10 (1991), pp. 1221–1232.

[138] V. N. Michailidou et al. "Dynamics of Concentrated Hard-Sphere Colloids Near a Wall". In: *Physical Review Letters* 102.6 (Feb. 2009).

[139] P. Mirtaheri, S. Grimnes, and O. G. Martinsen. "Electrode Polarization Impedance in Weak NaCl Aqueous Solutions". In: *IEEE T. Bio-Med. Eng.* 12.12 (2005), pp. 2093–3000.

[140] M. Ammam. "Electrophoretic deposition under modulated electric fields: a review". In: *RSC Adv.* 2.20 (2012), p. 7633.

[141] A. R. Gardeshzadeh, B. Raissi, and E. Marzbanrad. "Electrophoretic deposition of SnO_2 nanoparticles using low frequency AC electric fields". In: *Materials Letters* 62.10-11 (2008), pp. 1697–1699.

[142] J. Esmaeilzadeh et al. "Role of the Electric Field Affected Zone (EFAZ) on the electrophoretic deposition of TiO_2 nanoparticles under symmetric low-frequency AC electric fields". In: *The Journal of Physical Chemistry B* 117.6 (2012), pp. 1660–1663.

[143] J. F. Miller et al. "A combined Instrument for Phase Analysis Light Scattering and Dielectric Spectroscopy". In: *Journal of Colloid and Interface Science* 174.2 (1995), pp. 490–499.

[144] N. L. Thompson and B. L. Steele. "Total internal reflection with fluorescence correlation spectroscopy". In: *Nature Protocols* 2.4 (2007), pp. 878–890.

A. Calculations

A.1. Time until particles in field reach their electrophoretic velocity

In order to calculate the time until particles in an electric field reach their final electrophoretic velocity, the boundary conditions

$$v(t = 0) = 0\,\mathrm{m/s} \tag{A.1}$$

and

$$v(t = t_x) = \frac{2}{3} \cdot \frac{\epsilon_r \epsilon_0 \zeta E}{\eta}, \tag{A.2}$$

which describe the electrophoretic velocity at $t = 0$ right before the electric field E is applied and at t_x when the final and maximum electrophoretic velocity is reached, must be considered. In equation A.2, ϵ_0 and ϵ_r are the vacuum and relative permittivities, ζ the ζ-potential of the particles, and η the dynamic viscosity of the solvent.

When an electric field is applied on particles in a solution, it is subject to an accelerating force

$$F_{electric} = F_e = QE \tag{A.3}$$

which depends on the charge of the particle Q, and a decelerating drag force

$$F_{drag} = F_d = 6\pi\eta R_H v \tag{A.4}$$

which es proportional to the hydrodynamic radius R_H and the velocity of the particle v.

For the final electrophoretic velocity,

$$v(t) = (a_E + a_d) \cdot t \tag{A.5}$$

$$= \left(\frac{QE}{m} + \frac{6\pi\eta R_H}{m} \cdot \frac{QE}{m} \cdot t \right) t \tag{A.6}$$

is valid with the accelerations a_C and a_d referrring to the previously mentioned forces. Under consideration of boundary condition A.2, it equation A.6 can be written as

$$\left(\frac{QE}{m} + \frac{6\pi\eta R_H}{m} \cdot \frac{QE}{m} \cdot t_x \right) t_x = \frac{2}{3} \cdot \frac{\epsilon\epsilon_0\zeta E}{\eta} \tag{A.7}$$

and rearranged to

$$\frac{6\pi\eta R_H}{m} \cdot \frac{QE}{m} \cdot t_x^2 + \frac{QE}{m} \cdot t_x - \frac{2}{3} \cdot \frac{\epsilon\epsilon_0\zeta E}{\eta} = 0 \tag{A.8}$$

$$t_x^2 + \frac{m}{6\pi\eta R_H} \cdot t_x - \frac{2}{3} \cdot \frac{m}{6\pi\eta R_H} \cdot \frac{m}{QE} \cdot \frac{\epsilon\epsilon_0\zeta E}{\eta} = 0. \tag{A.9}$$

The quadratic formula is applied to solve equation A.9:

$$t_x = -\frac{m}{12\pi\eta R_H} \pm \sqrt{\left(\frac{m}{12\pi\eta R_H} \right)^2 + \frac{1}{9} \frac{m}{\pi\eta R_H} \cdot \frac{m}{Q} \cdot \frac{\epsilon\epsilon_0\zeta}{\eta}}. \tag{A.10}$$

For physical reasons only the solution with a positive sign is considered:

$$t_x = -1.47 \times 10^{-10}\,\mathrm{s} + \sqrt{2.16 \times 10^{-20}\,\mathrm{s}^2 - 3.09 \times 10^{-23}\,\mathrm{s}^2} \tag{A.11}$$

$$< 1 \times 10^{-10}\,\mathrm{s} \tag{A.12}$$

The particles reach their final velocity much faster than the time resolution of REDLS which is in the 1×10^{-6} s range. Only at AC frequencies in the GHz range and above, constant particle velocity cannot be assumed. To be exact, particles in an alternating electric field have a starting velocity of $v(t = 0 = -v_z)$, therefore the time elapsed for acceleration is strictly $2 \cdot t_x$ which does not change the conclusion.

Table A.1.: Values used for the distinct parameters in the calculations above.

m	$= \rho \cdot V = \rho \frac{4}{3} \pi R_H^3$	$= 3.52 \times 10^{-20}\,\mathrm{g}$
$\eta_{293\,\mathrm{K}}$	$= 1 \times 10^{-3}\,\mathrm{Pa\,s}$	
R_H	$= 20\,\mathrm{nm}$	
$\epsilon_{\mathrm{H_2O},298\,\mathrm{K}}$	$= 80$	
λ_D	$= 3\,\mathrm{nm}$	
ζ	$= -42.5 \times 10^{-3}\,\mathrm{V}$	
Q	$= \sigma A = \frac{\epsilon\epsilon_0\zeta}{\lambda_D} 4\pi R_H^2$	$= 5.03 \times 10^{-17}\,\mathrm{C}$

A.2. Volume fraction near the electrode

Volume fraction of the undisturbed sample:

$$c = 0.1\ \mathrm{wt\%} \tag{A.13}$$

$$\rho_{particles} = 1.05\,\mathrm{g\,cm^{-3}} \tag{A.14}$$

$$\Rightarrow\ \phi_1 \approx 1 \cdot 10^{-3} \tag{A.15}$$

Volume fraction if all particles in the sample cell (height $h = 163\,\mu\mathrm{m}$) are located in the volume near the electrode up to $z = 500\,\mathrm{nm}$ away from it:

$$\phi = \frac{V_{particles}}{V_{total}} \tag{A.16}$$

$$\frac{\phi_2}{\phi_1} = \frac{V_{total,1}}{V_{total,2}} \tag{A.17}$$

$$\Rightarrow\ \phi_2 = \phi_1 \cdot \frac{V_{total,1}}{V_{total,2}} \tag{A.18}$$

Using the above mentioned values for the distinct parameters, we end up with

$$\phi_2 = \phi_1 \cdot \frac{h}{z} \tag{A.19}$$

$$= 1 \cdot 10^{-3} \cdot \frac{163 \times 10^{-6}\,\mathrm{m}}{500 \times 10^{-9}\,\mathrm{m}} \tag{A.20}$$

$$= 0.326 \tag{A.21}$$

A.3. Shift of θ_{SPR} due to deposition of a particle monolayer

The shift of the angle of surface plasmon resonance due to the deposition of a particle monolayer on the gold surface has been estimated by calculating the reflectivity curves for the case of the naked gold layer and the gold layer with a particle monolayer with Winspall (Version 3.0, Jürgen Worm, MPI for Polymer Research). Therefore, the refractive index of a monolayer of polystyrene nanoparticles has been estimated by

$$n_{ML} = \phi \cdot n_{Part} + (1 - \phi_{ML}) \cdot n_{H_2O}. \tag{A.22}$$

ϕ is the volume fraction of particles in a closed monolayer,

$$\phi_{ML} = \frac{\frac{4}{3}\pi R^3}{(2R)^3} = 0.524 \tag{A.23}$$

with the particle radius R. From the calculation with Winspall, a shift of the angle of the surface plasmon resonance by 6.2° due to the deposit of a monolayer of the particles with $R = 100\,\text{nm}$ has been obtained. The parameters entered into Winspall are listed in table A.2.

The fraction of the gold surface covered with particles can be calculated by finding the refractive index of the monolayer n at which the calculated reflectivity curve matches the measured curve. By rearranging equation A.22, the volume fraction of particles in the deposit

$$\phi_{dep} = \frac{n_{meas} - n_{\mathrm{H_2O}}}{n_{Part} - n_{\mathrm{H_2O}}} \tag{A.24}$$

can be calculated. By comparing ϕ_{dep} to ϕ_{ML}, we can draw conclusions on the coverage of the gold surface by particles.

Table A.2.: Parameters used for the calculation of the shift of the angle of surface plasmon resonance. For the naked gold surface, the monolayer has just been omitted in the calculation of the reflectivity curve.

Layer	**Thickness / nm**	$\boldsymbol{n}$	$\boldsymbol{k}$
NLak8	0		0
Cr	1	2.687	3.350
Au	48	0.189	3.518
Monolayer	100	1.466	0
H_2O	0	1.33	0

B. Details on fit procedures

B.1. Fitting of the damping constant

The fit of the damping constant Γ_{cos} turned out to be difficult if all seven parameters in the fit function B.1

$$g_1(t) = \underbrace{A \cdot \exp(-(\Gamma_{exp} t)^{\beta})}_{\text{fast process}} + \underbrace{B \cdot \cos(\omega_{cos} t) \cdot \exp(-\Gamma_{cos} t)}_{\text{slow, periodic process}}. \tag{B.1}$$

were varied. Therefore, the damping constant has been fitted first in a separate step in which the maxima of the cosine have been fitted with a single exponential

$$f(t) = \exp(-\Gamma_{cos} t), \tag{B.2}$$

one example is shown in figure B.1. The respective functions have been each fitted three times with a varying number of points, and the average and standard deviation of the results have been declared the value and its error.

B.2. Fitting of the FCS decay

ACFs obtained in fluorescence correlation spectroscopy experiments in which the evanescent part of a totally internally reflected beam is used for excitation are fitted with a function [144]

$$g_{FCS}(t) = \frac{1}{2N}\left\{(1-2Rt)\exp(Rt)\,\mathrm{erfc}\left(\left[(Rt)^{\frac{1}{2}}\right]\right) + 2\left(\frac{Rt}{\pi}\right)^{\frac{1}{2}}\right\} \text{ with } R = \frac{D}{L_{\perp}^2}. \tag{B.3}$$

N is the average number of molecules in the evanescent volume, R the relaxation rate, D the diffusion coefficient, and $L_{\perp}$ the penetration depth of the evanescent light.

Figure B.2 shows some calculated FCS ACFs and their fits with a single exponential decaying function. Despite those fits being rather rough estimations, their relaxation rate Γ_{fit} matches the relaxation rate of the FCS ACF quite good as the linear fit of $\Gamma_{fit}(R)$ proves. The decay rates of the REDLS and FCS experiment can be directly compared because

$$\Gamma_{REDLS} = Dq^2 \quad \text{and} \quad \Gamma_{FCS} \approx R = DL_{\perp}^{-2} \tag{B.4}$$

and

$$q^2 = 3.5 \times 10^{14}\,\mathrm{m}^2 \approx L_{\perp}^2 = 4.0 \times 10^{14}\,\mathrm{m}^2. \tag{B.5}$$

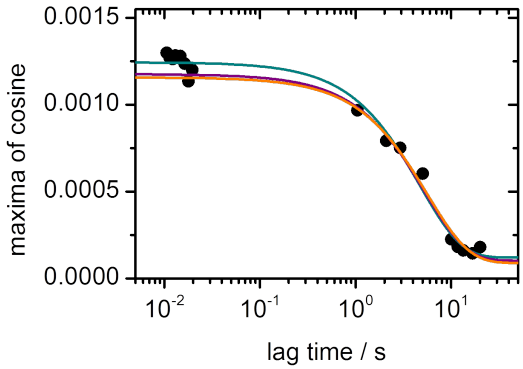

Figure B.1.: Example for the fit of the damping constant. The black circles are some points of the plataeu at $t < {}^{1}/_{\Gamma_{cos}}$, the maxima of the damped cosine, and some points of the plateau at $t > {}^{1}/_{\Gamma_{cos}}$. The colored lines represent three fits, in each one a different number of particles of the plateaus has to be taken into account.

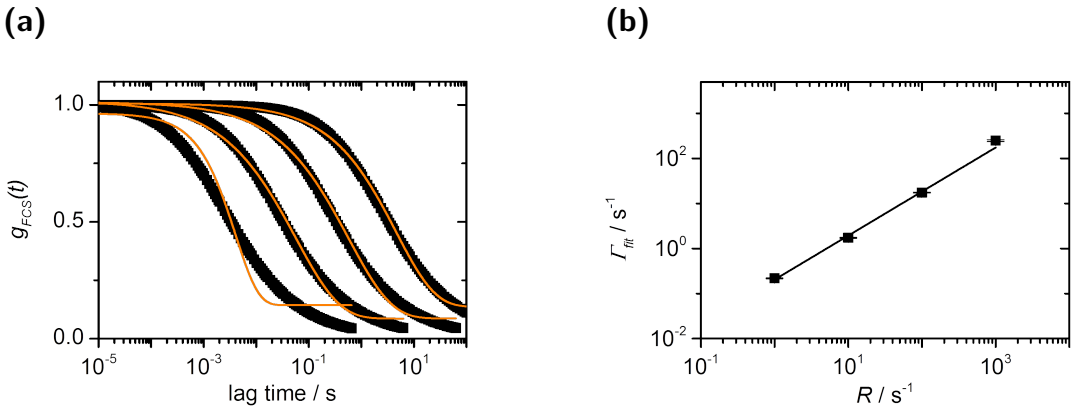

Figure B.2.: **(a)** Fits of FCS ACFs with a single exponential. **(b)** Relaxation rate of the single exponential versus the relaxation rate of the FCS ACF. The line represents a linear fit (slope = 0.977).

C. Abbreviations and symbols

C.1. Abbreviations

AA	acrylic acid
AC	alternating current
ACF	autocorrelation function
APD	avalanche photo diode
BODIPY	boron-dipyrromethene, 4,4-difluoro-4-bora-3a,4a-diaza-s-indacene
DL	double layer
DLS	dynamic light scattering
DLVO theory	Derjaguin-Landau-Verwey-Overbeek theory
EPD	electrophoretic deposition
FCS	fluorescence correlation spectroscopy
GPC	gel permeation chromatography
IHP	inner Helmholtz plane
ISL	inner Stern layer
ITO	indium tin oxide
KWW function	Kohlrausch-Williams-Watt function
MAA	methacrylic acid
MMA	methyl methacrylate
Nd:YAG	neodymium-doped yttrium aluminum garnet; Nd:$Y_3Al_5O_{12}$
NMR	nuclear magnetic resonance
OHP	outer Helmholtz plane
OLA	oligo(lactic acid)
OSL	outer Stern layer
PBS	phosphate buffered saline
PC	personal computer
PDADMAC	poly(diallyldimethylammonium chloride)

PLA, PLLA	poly(lactic acid), poly(L-lactic acid)
REDLS	resonance enhanced dynamic light scattering
SDS	sodium dodecyl sulfate
SEM	scanning electron microscopy
SPR	surface plasmon resonance, surface plasmon resonance spectroscopy
TEM	transmission electron microscopy
THF	tetrahydrofuran
UV	ultraviolet
VdW	Van der Waals
V70	2,2'-Azobis(4-methoxy-2.4-dimethyl valeronitrile)

C.2. Physical constants

c_0	$= 299\,792\,458\,\mathrm{m/s}$	speed of light in vacuum
h	$= 6.626\,069\,57 \times 10^{-34}\,\mathrm{J\,s}$	Planck constant
$\hbar$	$= 1.054\,571\,726 \times 10^{-34}\,\mathrm{J\,s}$	reduced Planck constant
k_B	$= 1.380\,649 \times 10^{-23}\,\mathrm{J\ K/mol}$	Boltzmann's constant

C.3. Variables

A	amplitude of the autocorrelation function or absorption
A_H	Hamaker constant
B	amplitude of cosine part of the autocorrelation function
C, C_i	symbol used for constants
c	speed of light
c^0	original concentration
D	diffusion coefficient
d	(center-to-center) distance
E	electric field strength
e	elementary charge or "e-value" for polarity quantification
F_{drag}	drag force
I	intesnity
k	reaction rate or wave number
$\vec{k_0}$	wave vector of incident wave

$\vec{k_{sc}}$	wave vector of scattered wave
$L_\perp, L_{\|\|}$	decay length of surface plasmon
M, M_t, M_r	torque, components of torque
N	absolute number of particles
$n_{(i)}$	number of particles or refractive index, indices indicate material
p	momentum
Q	"Q-value" for the quantification of reactivity
$q, \vec{q}$	(length of) scattering vector
q_{app}	apparent charge
R	resolution or radius
R_i	radius
R_H	hydrodynamic radius
r	reactivity ratio
$\vec{r}$	position
t	time or lag time
t'	lag time
T	Temperature
U	potential
U_{Born}	Born potential
U_{DLVO}	DLVO potential
U_{rep}	repulsive potential
V	voltage
v	velocity
W_i	work
z	number of charges or surface-to-surface distance
α	opening angle of an objective
β	stretching factor of stretched exponential function
$\Gamma_{(i)}$	decay rate, indices refer to fitting method
ϵ_0	vacuum permittivity
ϵ_r	relative permittivity, indices indicate material
ζ	ζ-potential
η	0 dynamic viscosity
κ	cumulant
λ	wavelength

λ_D	Debye length
μ	magnetic permeability
ρ_c	charge density
ρ_i	atom density
σ_c	surface charge
$\tau_{(i)}$	relaxation time, indices refer to fitting method
θ	scattering angle
θ_i	angle of incidence
θ_{gonio}	goniometer position angle
$\Upsilon_\perp, \Upsilon_{\|\|}$	correction factors for anisotropic diffusion coefficients
Φ	dimensionless potential
Ψ	potential
ω	angular frequency
ω_0	half-width length of Gaussian beam profile

C.4. Functions and operators

$G(t')$	FCS autocorrelation function
$g_1(t')$	field autocorrelation function (heterodyne detection mode)
$g_2(t')$	intensity autocorrelation function (homodyne detection mode)
$gamma(x)$	Gamma function
∇	Nabla operator, $\nabla = \frac{\partial^2}{\partial x^2} + \frac{\partial^2}{\partial y^2} + \frac{\partial^2}{\partial z^2}$

Acknowledgments

aus Datenschutzgründen online nicht verfügbar

Curriculum Vitae

aus Datenschutzgründen online nicht verfügbar